
# Towards identifying platinum anchor sites on carbon via a model electrochemical system



by

Adrian Charles Fortuin

A thesis submitted to the Department of Chemical Engineering
in conformity with the requirements for
the degree of Doctor of Philosophy

University of Cape Town
Cape Town, South Africa
March 2018

## Abstract

The interaction between Pt and its carbon support was investigated by a model electrochemical system. This entailed aggressively oxidising a two-dimensional carbon substrate, *i.e.* highly orientated pyrolytic graphite (HOPG) and mirror finish graphite (MFG) quartz crystal, to incorporate oxygen terminated groups into the graphitic matrix. This study focusses on potential cycling to determine the mobility of Pt across these carbon surfaces and the effect of the Pt anchoring to carbon on the electrocatalyst durability.

This work incorporates both a conventional three electrode electrochemical setup and the use of the electrochemical quartz crystal nano-balance (EQCN). The objectives of this study were to better understand the Pt mobility across the carbon substrate surface and to gain insight into the solid-liquid interface of Pt dissolution due to potential cycling.

Initial results on HOPG as discussed in chapter 2, indicated minimal Pt dissolution of between 13% and 15% of total electrochemical active surface area loss. These results, however, did not provide adequate evidence to conclusively determine the extent of Pt mobility on the carbon surface and the effect of oxygen terminated groups in hindering Pt dissolution.

In order to gain a more thorough understanding of the Pt dissolution processes, the use of the EQCN technique was utilised. Firstly, it was shown that the mirror finished graphite quartz crystals used in the EQCN technique, are qualitatively comparable to the electrochemical measurements recorded with the HOPG samples. Secondly, potential cycling under the same conditions as HOPG produced similar electrochemical results.

The frequency response curves from the EQCN yielded the most promising results. This study showed, qualitatively, that the surface of Pt is non-monotonic, and that the surface charge changes with increased potential cycling. Pt/MFG-A had consistent frequency responses over the entire potential range during Pt dissolution, thus, with the above understanding of surface charge, it is concluded that acid treated carbon substrates show a stronger affinity for Pt anchoring.

## Co-Authorship

All work carried out in this manuscript was carried out by Adrian Fortuin under the supervision of A/Prof Pieter Levecque and Dr Günther Scherer within HySA/Catalysis Centre of Competence, Catalysis Institute, Department of Chemical Engineering, University of Cape Town. Portions of this work includes contributions in sample preparation by Prof Cobus Kriek (North West University Potchefstroom Campus) in the form of Pt deposition by DC magnetron sputtering; data acquisition and analysis by Prof David Billing (University of the Witwatersrand), Dr Daniel Wamwangi (University of the Witwatersrand), Dr Rudolph Erasmus (University of the Witwatersrand), and Mr Adam Shnier (University of the Witwatersrand) in the form of X-ray reflectometry measurements, with Prof Sekhar Ray (University of South Africa Florida Campus), Dr Emanuela Carleschi (University of Johannesburg), and Dr Bryan Doyle (University of Johannesburg) in the form of X-ray photoelectron spectroscopy measurements; and Dr Colleen Jackson (University of Cape Town) as a peer-reviewed publication and conference proceedings.

Peer-reviewed publications:

Fortuin, A. C., Jackson, C., Carleschi, E., Doyle, B. P., Shnier, A., Kriek, R. J., Ray, S. C., Billing, D. G., Wamwangi, D., Scherer, G. G., and Levecque, P. B. J., *Towards practical applications of EQCN experiments to study Pt anchor sites on carbon surfaces*. Electrocatalysis, 2017.

Conference Proceedings:

Fortuin, A.C., Carleschi, E., Doyle, B.P., Billing, D.G., Erasmus, R., Shnier, A., Wamwangi, D., Kriek, R.J., Scherer, G.G., and Levecque, P.B.J. (2017). *Model Electrocatalyst to Study the Anchoring of Pt on Carbon for PEFCs*. Presented at the 68th Annual Meeting of the International Society of Electrochemistry in Providence, RI, USA.

Fortuin, A.C., Ray, S.C., Scherer, G.G., and Levecque, P.B.J. (2016). *Validation of a Method for Studying Pt Anchor Sites by EQCN*. Presented at the ECAT2016 Symposium in Kanagawa, Japan

## Acknowledgements

Finding the words to express my gratitude to the many people who have supported me and put up with me during the journey, is an incredibly difficult task.

This has not been an easy journey and this project has been ambitious from its inception. However, a Ph.D. is not just about the scientific work and scientific contributions (it does make up a large part), it is about the relationships one makes, the growth as a scientist, and learning how to deal with failure. Embarking on an incredibly complex problem with limited resources is never an easy task, but it allows one to push boundaries and understand the recorded data to its full extent. One develops an appreciation for the science, and one is humbled by the science. For me, this was the greatest lesson.

Although this journey was tough, there were many people in my life to support me. Far too many to thank individually in a short acknowledgement section (I will have to write a separate manuscript of appreciation and thanks if I want to get through everyone). Instead, I will limit my thanks to those people who have been active in the day to day journey, who have actively mentored me, and whom I've admired and have been inspired by. This does not mean I have forgotten everyone else, but if you haven't made this list, know that I cherish everything you have done for me and appreciate you.

A/Prof Pieter Levecque (supervisor): Ik wil graag mijn oprechte waardering uitspreken voor uw begeleiding in de loop van de jaren. Ik waardeer het extreme geduld dat je met me hebt gehad en ik zal altijd onze gesprekken over politiek en mensenrechten koesteren. Ik zal onze vriendschap voor altijd in de buurt houden. Bedankt voor alles. (Ik hoop dat google translate deze vertaling recht heeft gedaan.)

Dr Günther Scherer (supervisor): Deine Mentorschaft und Anleitung hat entscheidend zu meinem Wachstum als Wissenschaftler beigetragen. Ich bin unter Deiner Führung in mehr als einer Hinsicht beträchtlich gewachsen, und unsere Gespräche waren immer interessant und produktiv. Ich werde Ihre Eingaben und wissenschaftliche Kritik immer schätzen. Vielen Dank.

Prof Gregory Jerkiewicz (mentor and host): I would like to express my sincere thank you for hosting me in your lab and being an inspiration for this work. I hold your lab and quality of work in high regards and I appreciate the short time I spent with your group. My time spent in Kingston was memorable and I will always cherish my friendships with Nakki, Derek, Sadaf, Ram, and Jutae. I wish I was somewhat proficient in Polish such that I could thank you more thoroughly in your mother-tongue, for now I will just say, Dziękuję!

Prof Eric van Steen (mentor and HoD): Eric, je bent een voorbeeld en inspiratie sinds CHE2031F in 2008. Hoewel we niet veel samen hebben gewerkt, ben ik dankbaar voor de beperkte input die je me hebt gegeven voor mijn werk. Als ik groot ben, wil ik zoals jij zijn. Hopelijk kunnen we in de toekomst samen aan een paar projecten werken.

Dr Shiro Tanaka (mentor and friend): すべてありがとうございます。すばらしい会話に感謝し、あなたが私のためにしたすべてのことに感謝します。京都でお会いしましょう、お約束します。

Prof Cobus Kriek (mentor and friend): Dankie vir al die waardewolle en vrugbare gesprekke, end dat jy altyd so welwillend end akkommoderend was. Ek waardeer alles wat jy vir my gedoen het.

I would like to thank everyone in Pieter's group with whom I've worked with over the years: Dr Colleen Jackson, Dr Rhiyaad Mohamed, Dr Graham Smith, Dr Susan Taylor, Ilyaas Abdullah, Ntando Hlabangana, Nabeel Hussain, Clayton Jacobs, Thuli Khoza, Nobuhle Mpofu, and Caelin September. Thank you all for the great memories in the lab and trying to figuring out what we are doing, it has been awesome. I must extend a special thank you to Colleen for proof-reading this thesis for me, your input to make this document easier on the eye has inspired pride in this work. Thank you.

My friends and family have been the pillar of my emotional support and have endured many hours of debate and ranting on a subject they know nothing about. I appreciate the your time, ear to listen to me, and shoulders to cry on in some cases. Again, this is an endless list, I will

limit this to those who have had a direct impact on my life and whom have been around to listen to me about my work and all those times that I've just needed to moan about this Ph.D.

Lee-Anne Kallam: What can I say, I've learned a lot from you and have always appreciated our many conversations. Thank you for listening and offering advise during the course of my project. I don't know what I'm going to do without a Lee-Anne in my life, especially when I need to sort out research budgets.

Sharon Rademeyer: Friend, I hope we graduate at the same ceremony. You have been such a wonderful person in my life and someone who has always been willing to listen about lab issues and how it impacts on life. The Sunday hikes and Wednesday bouldering is something that I wouldn't have survived without. Thank you for being there when I've needed it.

Kimaya Reddy: Kim, let's be honest, I annoyed you, constantly. I was always on your case about something or other, and you were always on my case about giving you the inside scoop during your undergraduate studies. Fortunately, my strong moral compass couldn't be worn down and I was a useless source (I know this angered you greatly). Thank you for your friendship and listening to me about my work. Thank you for taking such a keen interest in my work and making the lab somewhat fun. I wish you every success and thanks for the free lunch, that one time.

Marc Wüst: For fear of getting too emotional and what not, let me lead with no homo. Marc, you are a special guy and someone I've looked up to over these years. In some instances I would look towards you as a father figure. I'm forever grateful for our friendship and miss you around the department. I promise I'll visit you and Zinzi in the depths of Middle Earth. God bless.

Lize: Well, you've had to deal with me at my worst, somehow you've stuck by my side. I cherish your support, your words, and your heart. Thank you for being the inspiration that renewed excitement in my work. I appreciate everything you've done for me and I hope that I can be a better a partner to you. Thank you for always believing in me, I love you.

Mother: I am where I am today because of you. From the day I was born you've put my needs and academic dreams ahead of yours. There is no way I can ever repay you or thank you enough. I've always tried to be the best I can and I've always strived to do great thinks. Thank you for always believing in me and paving the way to my successes. Your support has been invaluable and I could not have done this without you. Thank you, I love you.

Lastly, to the HySA team, the Catalysis Institute, and the University of Cape Town, I would like to express my gratitude for the world-class facilities and for the financial support. My sincerest gratitude and thanks to my collaborators for access to your facilities and good scientific discussions. The financial assistance of the National Research Foundation (NRF) towards this research is hereby acknowledged as well. Opinions expressed and conclusions arrived at, are those of the author and are not necessarily to be attributed to the NRF.

In conclusion, I would like to leave you all with a few quotes that I have summed up who I am as a scientist and the journey of this Ph.D.

*The task is not so much to see what no one has yet seen; but to think what nobody has yet thought, about that which everybody sees.*

Arthur Schopenhauer

*I would rather have questions that can't be answered than answers that can't be questioned.*

Richard Feynman

*Most people say that it is the intellect which makes a great scientist. They are wrong: it is character.*

Albert Einstein

## Plagiarism Declaration

I hereby certify that all of the work described within this thesis is the original work of the author. Any published (or unpublished) ideas and/or techniques from the work of others are fully acknowledged in accordance with the standard referencing practices.

I confirm that I have been granted permission by the University of Cape Town's Doctoral Degrees Board to include the following publication in my PhD thesis, and where co-authorships are involved, my co-authors have agreed that I may include the publication:

Fortuin, A. C., Jackson, C., Carleschi, E., Doyle, B. P., Shnier, A., Kriek, R. J., Ray, S. C., Billing, D. G., Wamwangi, D., Scherer, G. G., and Levecque, P. B. J., *Towards practical applications of EQCN experiments to study Pt anchor sites on carbon surfaces.* Electrocatalysis, 2017.

Adrian Charles Fortuin

FRTADR005

Signed by candidate

12 March 2018

# Table of Contents

## List of Figures

## List of Tables

## List of Abbreviations

| | |
|---|---|
| $A$ | geometric area ($cm^2$) |
| ADT | accelerated durability test |
| AFM | atomic force microscopy |
| $C$ | capacitance ($F.cm^{-2}$) |
| $C_f$ | calibration factor ($ng.Hz^{-1}.cm^{-2}$) |
| CV | cyclic voltammogram |
| $d$ | crystallite size (nm) |
| DLR | double layer region |
| $D_O$ | diffusivity of oxidised species ($cm.s^{-1}$) |
| $D_R$ | diffusivity of reduced species ($cm.s^{-1}$) |
| $E$ | potential (V) |
| ECSA | electrochemical active surface area ($m^2.g_{Pt}^{-1}$) |
| EQCM | electrochemical quartz crystal micro-balance |
| EQCN | electrochemical quartz crystal nano-balance |
| $F$ | Faraday's constant (96,485 $C.mol^{-1}$) |
| $f$ | F/RT (38.92 $V^{-1}$ at 25 °C) |
| $f_0$ | base resonant frequency (Hz) |
| FT-IR | Fourier transform infrared spectroscopy |
| GC | glass carbon |
| HOPG | highly orientated pyrolytic graphite |
| HOPG-A | acid oxidised HOPG |
| HOPG-H | peroxide (Fenton's reagent) oxidised HOPG |

| | |
|---|---|
| HOPG-P | pristine HOPG |
| $H_{upd}$-R | hydrogen underpotential deposition region |
| $j$ | current density ($mA.cm^{-2}$) |
| K | dimensionless shape factor |
| $k^0$ | rate constant ($cm.s^{-1}$) |
| $M$ | atomic mass ($g.mol^{-1}$) |
| MFG | mirror finish graphite |
| MFG-A | acid oxidised MFG |
| MFG-H | peroxide (Fenton's reagent) oxidised MFG |
| MFG-P | pristine MFG |
| ML | monolayer |
| $N$ | frequency parameter (1,661 kHz.mm for AT-cut quartz) |
| $n$ | harmonic mode |
| OFRR | oxide formation and reduction region |
| PEFC | polymer electrolyte fuel cell |
| $Pt_{poly}$ | polycrystalline platinum |
| PZTC | potential of zero total charge |
| QCM | quartz crystal micro-balance |
| $R$ | ideal gas constant ($8.314\ J.mol^{-1}.K^{-1}$) |
| RHE | reversible hydrogen electrode |
| SEM | scanning electron microscopy |
| STM | scanning tunnelling microscopy |
| $T$ | temperature (°C) |

| | |
|---|---|
| $t$ | time (s) |
| TEM | transmission electron microscopy |
| UHV | ultra-high vacuum |
| UPD | underpotential deposition |
| XPS | X-ray photoelectron spectroscopy |
| XRD | X-ray diffractometry |
| XRR | X-ray reflectometry |
| $z$ | valence electrons/charge of metal species |
| $\alpha$ | transfer coefficient |
| $\beta$ | full width at half maximum (rad) |
| $\Delta E_P$ | difference between peak anodic and peak cathodic potentials (mV) |
| $\Delta f$ | frequency change (Hz) |
| $\Delta i$ | current difference at fixed potential (A) |
| $\Delta m$ | mass change (g) |
| $\Delta m_g$ | mass change per unit area ($g.cm^{-2}$) |
| $\Delta q$ | change in charge density ($C.cm^{-2}$) |
| $\theta$ | incident angle (deg) |
| $\lambda$ | wavelength (Å) |
| $\mu_q$ | shear modulus of quartz ($2.947 \times 10^{11}$ $g.cm^{-1}.s^{-2}$) |
| $\nu$ | scan rate ($mV.s^{-1}$) |
| $\rho_q$ | density of quartz ($2.648$ $g.cm^{-3}$) |
| $\Phi$ | angle normal to sample surface (deg) |
| $\Psi$ | dimensionless rate parameter |

# Chapter 1
# Introduction and Background

## 1.1 Background to Study

The increased inner-city air pollution, global climate change, and increased awareness of environmental sustainability; there has caused a strong drive towards using alternative means to power our cities and vehicles in a more environmentally friendly and sustainable manner.

To this end, many technologies exist and are being successfully implemented worldwide. Energy grids are being sustained by renewable energy sources (such as wind and solar energy), while batteries, pumped storage hydroelectric dams, compressed air, and hydrogen can be used as grid storage/fuels. However, there still remains much research to improve current technologies, particularly grid storage technologies, such that sustainable energy solutions can be implemented at large macroeconomic scales [1].

Currently, much attention has been given to lithium-sulphur, sodium-ion, lithium-air, Pb-acid, and redox flow batteries. The predecessor to the aforementioned technologies, and current technology of choice, is the lithium-ion battery, which finds use in technologies ranging from mobile devices to small grid storage devices for smart homes. While this technology works well, there are multiple shortfalls of the technology, *viz*. Boeing 787 Dreamliner overheating issues of 2013 and Samsung Galaxy Note 7 self-combusting issues of 2016, to name a few.

An alternative technology, which is lighter and more energy dense, is the hydrogen polymer electrolyte fuel cell. This technology has been around for decades, and a related fuel cell (alkaline fuel cell) was used to power the beginning of the space age with the Gemini programme for the National Aeronautics and Space Administration (NASA). While there has

been much push back in terms of required infrastructure, hydrogen generation, safety, *etc.*, hydrogen fuel cells are still an attractive technology to bridge the gap between fossil fuels and renewables. Secondly, the technology has many uses in large scale stationary applications, such as back-up power for telecommunication towers in remote locations.

Considering that South Africa has the world's largest platinum reserves (> 80 %), the South African Government started the Hydrogen South Africa initiative to (i) stimulate the economy from resource based to value-add based, and (ii) to stimulate job creation. The choice to invest in hydrogen and hydrogen fuel cells, in particular, was a strategic use of South Africa's naturally abundant mineral resources. As a result, three centres of competence (CoC) were formed, namely, HySA/Catalysis, HySA/Systems, and HySA/Infrastructure. As the names suggest, HySA/Catalysis broadly focusses on catalyst related research for hydrogen production and hydrogen to energy conversion, while HySA/Systems focusses on system integration of fuel stacks into technologies such as forklifts, *etc.*, and HySA/Infrastructure focusses on hydrogen storage and infrastructure development for a hydrogen network, and policies and regulations for the technology.

In recent years, one of the focusses of HySA/Catalysis has been to study and understand the typical hydrogen fuel cell electrocatalyst (henceforth referred to as polymer electrolyte fuel cells). While focus has been to study alternative supports for the Pt supported on carbon (Pt/C) electrocatalysts, an understanding of the metal-support interactions between Pt and carbon needed to be better understood. This work will thus investigate these Pt-C interactions by employing a model electrochemical system, *i.e.* making use of a two-dimensional carbon substrate, and an underappreciated electrochemical analytical technique, *i.e.* the electrochemical quartz crystal nano-balance (EQCN).

## 1.2 Literature Review – Carbon as a Support for Pt

### 1.2.1 Active Metal Electrocatalyst for Polymer Electrolyte Fuel Cells

Much of the on-going research into low temperature polymer electrolyte fuel cells (LT-PEFCs) shows Pt (pure and alloyed) to be the active metal catalyst of choice in commercial applications. Oxygen species bind to Pt in a way such that it doesn't bind too strongly or weakly, thereby showing the most favourable activity to the oxygen reduction reaction (ORR) as illustrated in fig. 1.1 below [2].

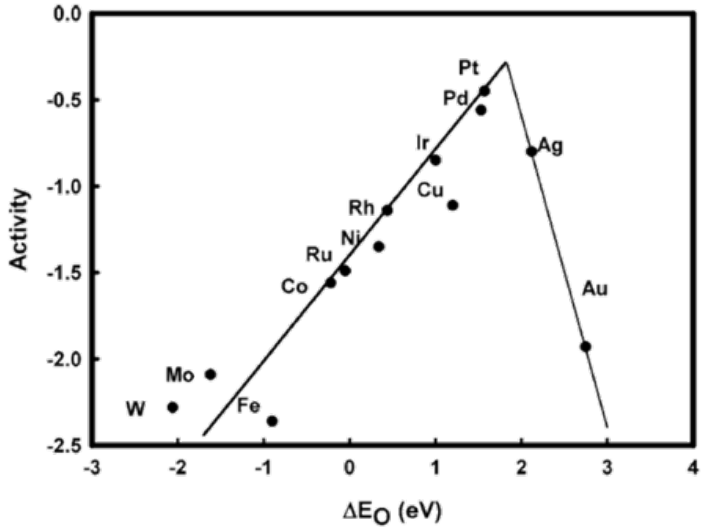


**Figure 1.1 Trends in the ORR activity as a function of the binding energy of oxygen to various metals. From Nørskov *et al.* [2]**

Regardless of Pt being the best single metal catalyst for this reaction, the high cost has spurred focused research efforts towards increasing the utilisation of the Pt, and hence lowering Pt loading. Historically, bulk Pt black has been employed as the electrocatalyst in an early PEFC on the Gemini missions at loadings of 28 $mg_{Pt}/cm^2$ [3]. With the boom of space exploration and military funding, advancements in PEFC saw Pt black loadings of 4 $mg_{Pt}/cm^2$ [4], a seven-fold reduction in Pt content. However, to see widespread adoption of the technology, particularly for automotive applications, Pt loading needed to be reduced even further. This reduction was achieved by supporting Pt on carbon blacks resulting in loadings of < 0.4 $mg_{Pt}/cm^2$ [5], with the

ultimate aim of reaching 0.125 $mg_{PGM}/cm^2$ by 2020 [6]. The selection of carbon as a support material is to ensure mechanical stability, resistance to the corrosive environment, increase surface area for better Pt utilisation, and most importantly to serve as an electron conductor to the Pt nanoparticles [5,7].

However, there has been great interest to not only reduce platinum content in PEFCs, but to increase activity towards the ORR by alloying Pt with various transition base metals [8-11]. The base metal inclusions and the highly acidic environment result in the un-leached bimetallic alloy catalysts undergoing rapid degradation with prolonged operation [8]. Yet, despite improvements obtained by alloying, the challenge of lowering Pt loading and minimising Pt loss still remains.

Pt/C also undergoes degradation by one of four main mechanisms, *viz.*: platinum dissolution, agglomeration, carbon corrosion and particle detachment [11-18] as illustrated in fig 1.2. Despite the main pathways of Pt loss being identified, as mentioned above, there still remain unanswered questions around the exact mechanisms of platinum dissolution, agglomeration and particle detachment [12,16,18,19]. However, current research is focussed primarily on using *in-situ* inductively coupled plasma mass spectroscopy to study the kinetic rate of Pt dissolution on potential cycling and the preferential facets for Pt dissolution leading to a stable thermodynamic structure [17,20-24]. In order to understand these mechanisms, one needs to first take a step back and appreciate and understand the mechanism by which platinum nanoparticles anchors itself to the carbon support.

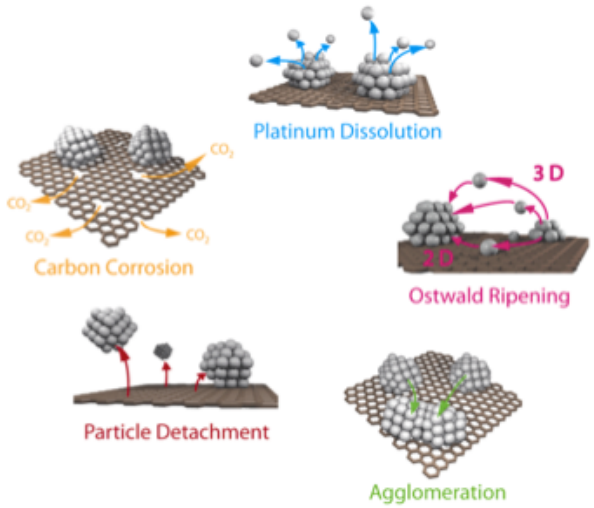


**Figure 1.2 Schematic of proposed degradation mechanisms of Pt/C in PEFCs. From Meier *et al.* [19]**

### 1.2.2 Carbon substrate for Pt anchoring

Vulcan XC-72R is a type of electrically conductive furnace black produced as a by-product of crude oil refinery [25,26]. Vulcan XC-72R is relatively free of surface oxides as the decomposition into carbon black particles are processed at temperatures of approximately 1400 °C and under oxygen deficiency. Furnace blacks have amorphous carbon growth centres, around which ordered graphitic carbon structures form.

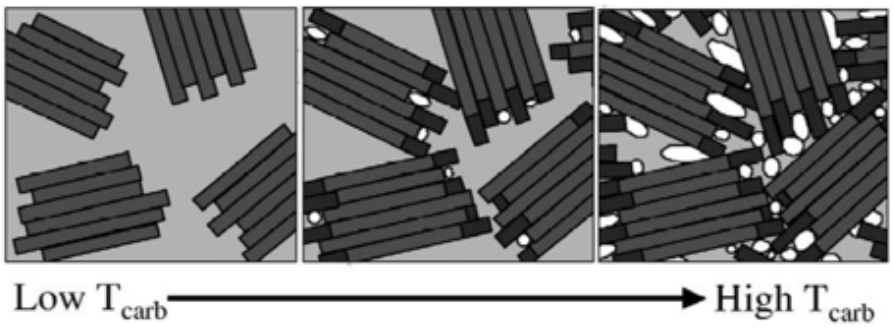


**Figure 1.3 Growth of graphene sheets (dark grey for growth, medium grey for graphene crystallites) from disordered (amorphous) carbons (light grey) as a function of temperature. From Kercher and Nagle [27]**

Fig. 1.3 from Kercher and Nagle [27], illustrates the ordering of amorphous carbons with increasing temperature, *i.e.* the carbonisation of crude oil residue for the production of furnace blacks. The high temperature of furnace black processing allows for the production of analogous spherical structures as presented in the right-most pane of fig. 1.3. The outer surfaces of Vulcan XC-72R are graphitic (high $sp^2/sp^3$ ratio) and thus form a conducting network across the surface of the particle.

However, there is significant interest to use evermore ordered carbon structures, *e.g.* carbon nanotubes (CNTs), carbon nanofibres (CNFs), *etc.* for applications not just related to PEFCs [28-32]. These ordered structures are mechanically stronger with anisotropic electrical conductivity and are more flexible than Vulcan XC-72R. Such ordered carbon structures are easily doped, predominately with nitrogen, to serve as a support for Pt or as a metal-free catalyst [33-36]. The move towards these structures as alternative supports and complex networks gives an indication as to the requirement of the carbon support substrate, albeit at a higher cost.

Highly orientated pyrolytic graphite (HOPG) is used in many fundamental studies [19,26,37-41] and it serves as a highly suitable model substrate to mimic theoretical representations of graphite [42]. It eliminates the complexities associated with CNTs and CNFs, allowing for fundamental surface studies to be conducted between the substrate and anchored metal particles [19]. HOPG is unique in that it can be synthesised such that it has a near smooth atomic surface (often used as a calibration material for scanning tunnelling microscopes) giving a seemingly infinite atomic surface for the study of atomic interfaces.

PEFCs electrocatalysts rely on the conductive nature of the carbon support, therefore, HOPG serves as a good model substrate to study atomic interfaces and interactions between metal and support, reproducibly as a model for the real-world catalyst [42].

### 1.2.3 Pt Interaction with Carbons

There remains much speculation as to how platinum deposits and interacts with its support substrate. However, it has been known for some time that defects on graphitic surfaces, particularly for pyrolytic graphites, can be decorated with gold, or platinum, silver, indium, *etc.*, and analysed under a transmission electron microscope [43]. This does not inform us how the particles are deposited, only that there are steps or kinks in the surface morphology. Furthermore, for a carbon system, it is firmly believed that platinum deposits with the aid of carboxylic groups, phenolic groups and/or $\pi$ sites at surface defects altering the densities of state of platinum [28,44-47].

To better understand the process of Pt deposition, Aktary *et al.* [44] conducted a study to propose a potential mechanism by which a particular platinum precursor (1,5-cyclooctadiene-dimethylplatinum(II), *i.e.* $Pt(COD)(CH_3)_2$) is deposited onto HOPG as illustrated in fig. 1.4 below.

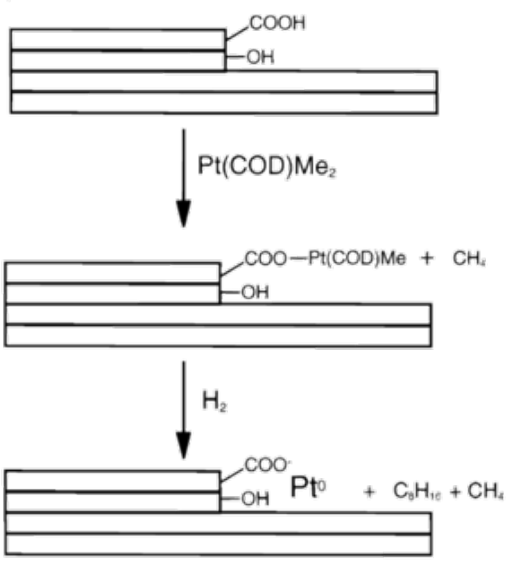


**Figure 1.4 Potential chemical vapour deposition mechanism of Pt(II) on edge plane site of HOPG. From Aktary *et al.* [39]**

The work of Aktary *et al.* [44] is conducted on the edge plane of HOPG, rather than the basal plane, making use of the idea that carboxylic acid groups are likely to populate the edge sites

of carbon. This suggestion is further supported by the fact that edge plane surfaces of HOPG show higher activity to the ORR than the basal plane [43]. Again, it is unknown whether this is due to the presence of carboxylic acid groups or not. The proposal of the spacing between graphitic sheets acting as an anchoring site was not suggested.

### 1.2.4 Graphitic structure

The challenge in understanding the interaction of Pt and the support, does not arise from the honey-comb lattice structure that is graphene and graphite, but rather from the inclusion of surface functional groups that sparsely populate the surface of graphite.

To understand the inclusion of surface functional groups on graphite, one needs to understand the insulation properties of graphite oxide [48,49], which illustrate the highest degree of functionalisation. Six acclaimed models for graphite oxide have been proposed of which the Lerf-Klinowski model (illustrated in fig. 1.5 below) acts as a summation of all proposed models. The only truly accepted condition is the presence of alcohol groups and 1,3 ethers/epoxide groups on the basal plane, with much debate as to the presence of carboxylic acid groups on the edge planes [43,50,51].

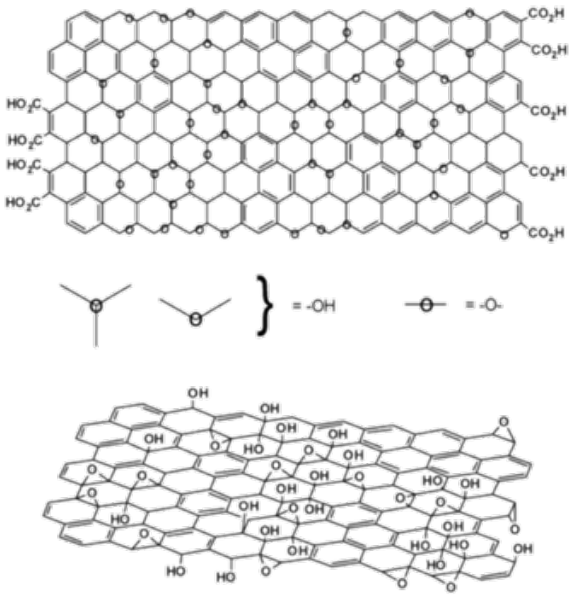


**Figure 1.5 An illustration of the Lerf-Klinowski structural model of graphene oxide with carboxylic groups present (top) and not present (bottom). From Dreyer *et al.* [46]**

However, conductivity of carbon is dictated by the presence of $sp^2$ hybridised structures and can be formed by carbonisation processes where the acidity of carbon is driven off as $H_2O$, CO and $CO_2$ by a temperature increase, thus restoring aromaticity [43,49,51-53]. Carbons with high aromaticity, such as highly graphitic structures, are chemically inert and hence require functionalisation to a certain degree [54]. Typically, structures such as carbon nanotubes, carbon nanofibres, *etc.*, are pre-treated in a highly acidic medium to create the required functionalisation. This does not allow for a very controlled regime and sees a plethora of various oxygen species populating the graphitic surface with no clear means to determine the trend by which a specific oxygen species is increasing with functionalisation [28,31,45,46,54-59].

The critical question is how a metal, *e.g.* platinum, can deposit on a surface that requires a high degree of aromaticity as well as sites for nucleation. While the answer to this question remains unknown to most, irrespective of support (alumina, titania, silica, *etc.*), the answer is linked to the periodicity of the support [60] and the presence of oxygen groups [28,44-47] as discussed above.

## 1.3 Literature Review – The Electrochemical Quartz Crystal Nano-balance

### 1.3.1 Quartz Crystal – Properties and Structure

The electrochemical quartz crystal nano-balance (EQCN) is an instrument used to monitor *in-situ* mass change with applied potential and time. The technique makes use of quartz crystal that is resonated at a specific frequency, *viz.* 3 MHz for resolution of 50 ng, 9 MHz for a resolution of 3 ng, and 27 MHz for a resolution of 200 pg. The aforementioned technique, thus, relies on the piezoelectric properties of the quartz crystal [61].

Depending on the plane in which the quartz crystal is cut gives rise to different modes of operation, *viz.* thickness shear, face shear, *etc.* (fig. 1.6). These properties influence the sensitivity of the quartz crystal to variances in temperature and/or base resonance frequency, over the intrinsic properties of the particular cut [62,63].

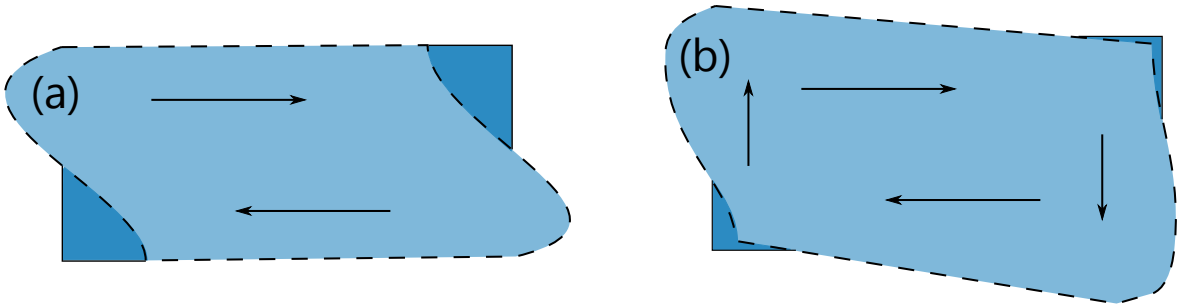


**Figure 1.6 Modes of oscillation of the quartz crystal with (a) representing thickness shear and (b) representing face shear**

The basis of operation of the quartz crystal, is to apply an external electric field to the quartz crystal, which induces a mechanical stress as depicted in fig. 1.6, resulting in the crystal oscillating at a particular frequency [61,64]. For the purpose of studying interfacial electrochemical systems, quartz crystals cut in particular plane are employed (as illustrated in fig. 1.7), known as the AT-cut. This cut shows thickness shear characteristics [61,64].

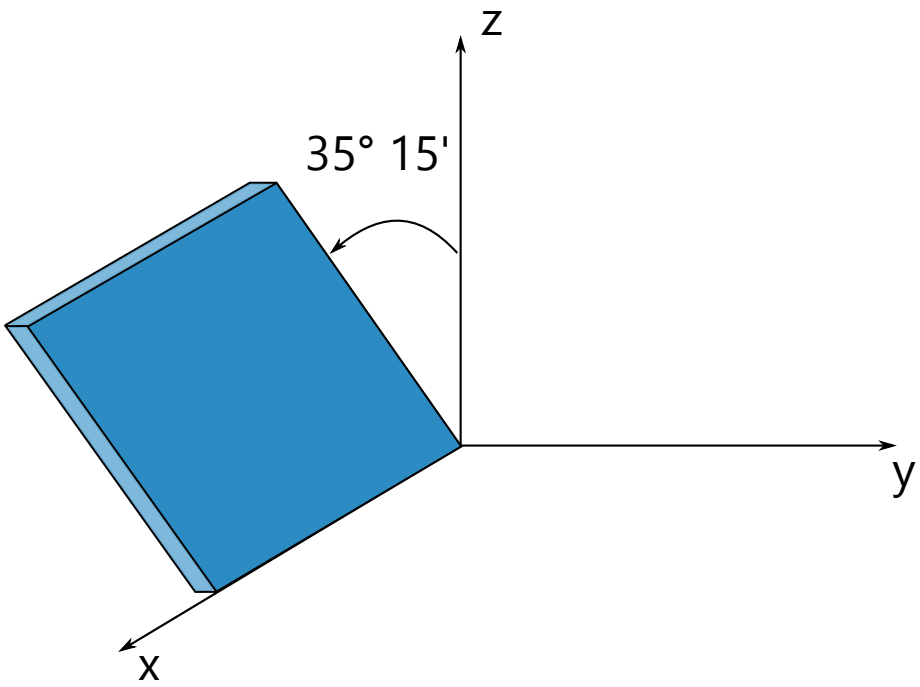


**Figure 1.7 Quartz crystal AT-plane. Reproduced from O'Sullivan and Guilbault [59]**

While there are many alternative cuts for quartz crystals, the AT-cut is the most common and easiest to manufacture [63], however, the AT-cut is more sensitive to temperature gradients. On

the other hand, cuts such as the BT- and SC-planes, are less prone to thermal drift, but show poorer performance and less predictability in coupled applications (*i.e.* electrochemical applications) [62,63].

### 1.3.2 The Sauerbrey Equation

The underlying physics of relating frequency change to mass change makes use of the Sauerbrey equation [65] as indicated below:

$$\Delta f = -\frac{2f_0^2}{n\sqrt{\rho_q \mu_q}}\Delta m \qquad (1.1)$$

whereby:

$\Delta f$ is the measured frequency change (Hz)

$f_0$ is the baseline frequency of the quartz crystal in air (9.03 MHz)

$n$ is the harmonic mode ($n$ = 1)

$\rho_q$ is the density of quartz (2.648 g.cm$^{-3}$)

$\mu_q$ is the shear modulus of quartz (2.947 x 10$^{11}$ g.cm$^{-1}$.s$^{-2}$)

$\Delta m$ is the associated mass change (g)

However, the Sauerbrey equation only relates to oscillations in air and as a continuous elastic extension of the quartz [66]. For liquid contact, the physics of the system changes and other factors need to be taken into consideration as shown below [61,67]:

$$\Delta f = \Delta f_m + \Delta f_v + \Delta f_p + \Delta f_T + \Delta f_s + \Delta f_r \qquad (1.2)$$

whereby:

$\Delta f_m$ is the associated mass change from equation 1.1

$\Delta f_v$ is due to viscosity effects of the solution

$\Delta f_p$ is due to pressure effects from fluid pressure head

$\Delta f_T$ is due to temperature effects

$\Delta f_s$ is due to stress effects

$\Delta f_r$ is due to surface roughness effects

However, in order to compensate for the above effects described in equation 1.2, the Sauerbrey equation can be rearranged with a calibration factor ($C_f$) to take into account the various physical phenomena that are introduced by submerging the quartz crystal in a liquid media. This modified equation, thus requires the calibration of the frequency change with a known addition of mass by electrodeposition [67]. The modified equation is shown below:

$$\Delta m = -\frac{n\sqrt{\rho_q \mu_q}}{2f_0^2}\Delta f = -\frac{N\rho_q}{f_0^2}\Delta f = -C_f \Delta f \qquad (1.3)$$

whereby:

$N$ is a frequency parameter which is dependent on the of cut of quartz (1661 kHz.mm) [63]

$C_f$ is the calibration factor determined experimentally (ng.Hz$^{-1}$.cm$^{-2}$)

Hence, electrochemical measurements making use of equation 1.3 rely quite substantially on the calibration factor, $C_f$, and the method of calibrating the EQCN in a liquid/aqueous media. Typically, $Ag^+$ or $Cu^{2+}$ is used as the deposition material for calibration and absolute mass data and interpretations originate from this method [66-71]. Thus, in order to correlate EQCN data published throughout the scientific community, $C_f$ should be a constant regardless of the metal salt used for calibration.

### 1.3.3 EQCN Calibration

In order to quantify mass addition and subtraction at the atomic level, the EQCN needs to be calibrated experimentally to ensure that the various forces within the system are taken into account, as described in equation 1.2. Various metal salts are used in literature in order to

deposit a known quantity of metal, however the use of $Ag^{+}$ and $Cu^{2+}$ salts are the most common [66-71], across multiple disciplines as illustrated in table 1.1.

**Table 1.1 Theoretical and experimental calibration factors ($C_f$) as reported in literature for different metal salts and base frequencies ($f_0$)**

| $M^{z+}$ conc. ($mmol.L^{-1}$) | Supporting Electrolyte | $f_0$ (MHz) | $C_f$ ($ng.Hz^{-1}.cm^{-2}$) | Ref. |
|---|---|---|---|---|
| Theoretical | - | 5 | 17.7 | - |
| 1.0 mM $Cu^{2+}$ | 0.5 M LiCl in HCl (pH = 4) | 5 | 24.7 | [68] |
| 0.82 mM $Ag^{+}$ | 0.14 M $HClO_4$ | 5 | 19.8 | [68] |
| Theoretical | - | 6 | 12.3 | - |
| $Cu^{2+}$ | - | 6 | 13.3 | [69] |
| Theoretical | - | 9 | 5.45 | - |
| $Cu^{2+}$ | 0.5 M $H_2SO_4$ | 9 | 5.61 | [66] |
| $Cu^{2+}$ | - | 9 | 6.13 | [69] |
| 1.5 mM $Ag^{+}$ | 0.5 M $H_2SO_4$ | 9 | 4.19 | [67] |
| 1.5 mM $Ag^{+}$ | 0.5 M $H_2SO_4$ | 9 | 5.18 | [72] |
| 1.0 mM $Ag^{+}$ | 0.5 M $HClO_4$ | 9 | 5.32 | [70] |
| 1.0 mM $Ag^{+}$ | 0.2 M $H_2SO_4$ | 9 | 5.50 | [71] |
| Theoretical | - | 27(3) | 1.82 | - |
| $Cu^{2+}$ | - | 27(3) | 1.75 | [69] |

In the case of quartz crystals with a base frequency of 9 MHz, the calibration factor is within ± 1 $ng.Hz^{-1}.cm^{-2}$. This illustrates the accuracy of the technique, such that error is within a nanogram of what is recorded. However, this is still not sensitive enough to measure monolayers of $H_{ads}$.

In order to determine the calibration factor, $C_f$, one requires a (i) keen understanding of metal underpotential deposition (UPD) and the relative work functions between deposition metal and metal substrate, and (ii) UPD coverage of the deposition metal on the metal substrate.

For the case of Pt and Au metal substrates, UPD has been studied extensively by Kolb [73-76], Bruckenstein [77,78], Ross [79-81], Wilde [82], Feliu [83-88], and many more groups [89-98]. With applications ranging from fundamental atomistic understanding and kinetics of the UPD

process to using UPD as a tool to determine heavy metal contaminants in water sources.

The above processes have been studied extensively, that the application of (i) Faraday's 1st law of electrolysis [99], (ii) the Sauerbrey equation [65], and (iii) known metal salt solution for a particular system can be easily related mathematically. Thus, it is understandable why the likes of Ag and Cu have been chosen for Pt and Au systems. Both Ag and Cu, readily form uniform layers across the surface of Pt and/or Au, thus giving a close approximation of mass change as defined by Faraday's 1st law of electrolysis in equation 1.4.

$$\Delta m_g = \left(\frac{\Delta q}{F}\right)\left(\frac{M}{z}\right) \tag{1.4}$$

whereby:

$\Delta m_g$ is the change in mass per unit area ($g.cm^{-2}$)

$\Delta q$ is the change in charge as a result of current flow ($C.cm^{-2}$)

$F$ is Faraday's constant (96,485 $C.mol^{-1}$)

$M$ is the molar mass of the metal being electrodeposited ($g.mol^{-1}$)

$z$ is the charge of the metal solution being reduced

If we are to consider the system of the EQCN, we can then combine equations 1.3 and 1.4 to accurately determine the calibration factor, $C_f$ as indicated in equation 1.5.

$$C_f = \left(\frac{M}{zF}\right)\left(\frac{\Delta q}{\Delta f}\right) = \left(\frac{M}{zF}\right)\left(\frac{j\Delta t}{\Delta f}\right) \tag{1.5}$$

whereby:

$j$ is the current density ($A.cm^{-2}$)

$\Delta t$ is the time over which the current density, $j$, is applied (s)

However, even with experimental data, $C_f$ cannot be determined accurately below a certain threshold. Although the theoretical algebra predicts a linear relationship, this is only experimentally true in a narrow window. Work by Jerkiewicz *et al.* [67,72] has shown that deposition of less than 4 ML's results in localised deposition, and only once that threshold has been reached, a homogenous distribution of the deposition metal is achieved (fig. 1.8) [100].

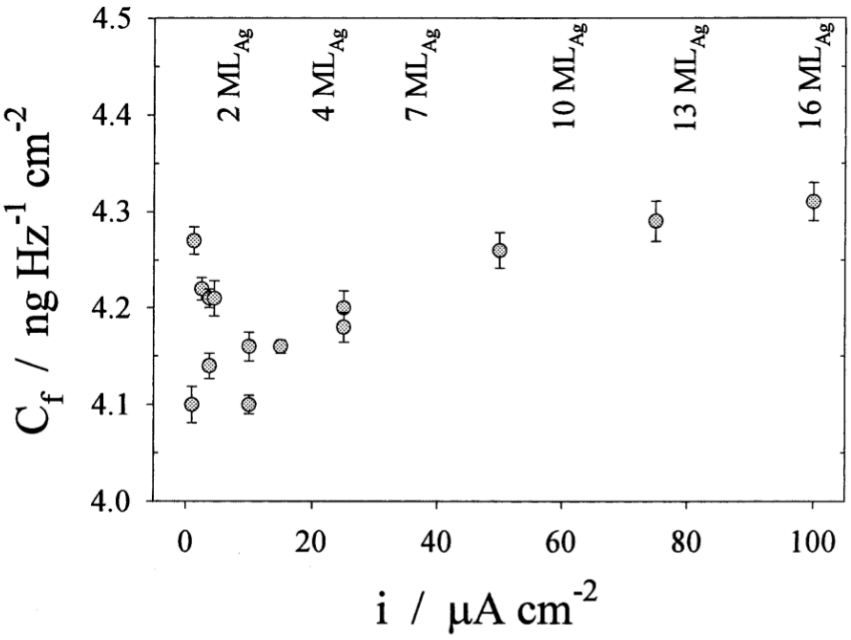


**Figure 1.8 Comparison of calibration factor at various Ag deposition current densities. From Vatankhah *et al.* [62]**

From fig. 1.8 we see scattering of the $C_f$ value below 4 ML's, but a steady logarithmic increase thereafter. This deviates from the linearity of equation 1.5 due to the exclusion of various forces in the derivation. Anion effects of supporting electrolyte [101], double layer capacitance [102], deposition additives, *etc.*, all play a role in the uniform deposition of a dissolved metal onto the substrate metal. While experimental determination of $C_f$ gives a good representation of the associated mass changes, one cannot assume it is absolute. As multiple physical effects are at play, these need to be taken into consideration when determining $C_f$, in particular, maintaining a narrow range of ML's deposited seems to be a good estimate for now.

## 1.4 Objectives and Scope

The main objectives of this study are two-fold:

(i) To identify Pt anchor sites on carbon substrates and determine their effect on catalyst durability.

(ii) Show that we can use the EQCN technique to study Pt dissolution rates on carbon substrates and hence qualitatively determine catalyst durability.

While the above is rather broad and encompasses many years of research, the scope of this study has been limited to only studying 2-D substrates, *viz*. highly orientated pyrolytic graphite (HOPG), and graphite quartz crystals. Pristine surfaces were studied to obtain a baseline for comparison for two different surface modifications.

This work aims to qualitatively determine Pt mobility across a carbon substrate, as well as to ascertain whether or not the EQCN technique can be used as a tool in electrocatalyst degradation studies.

The outline of this thesis is in the form of standalone results chapters, where chapter 2 investigates the surface modification of HOPG by oxidation and how these surface modifications affect Pt mobility and Pt dissolution. Chapter 3 focusses on the whether or not we can directly compare results obtained from the EQCN to classical systems, due to the difference in the carbon structure between HOPG and the graphite deposited onto the quartz crystal. With this, in chapter 4 we can then investigate Pt/C degradation mechanisms using the EQCN technique. Lastly, overall conclusions are drawn in chapter 5 to link the results from chapters 2 through 4. It is important to note that each chapter has the structure of introduction, experimental methods, results and discussion, and conclusions.

## 1.5 References


[1] *Horizon 2020 - Work Programme 2018-2020: Secure, clean and efficient energy*. 2017, European Union.

[2] Nørskov, J. K., Rossmeisl, J., Logadottir, A., Lindqvist, L., Kitchin, J. R., Bligaard, T., and Jónsson, H., *Origin of the Overpotential for oxygen reduction at a fuel-cell cathode.* The Journal of Physical Chemistry B, 2004. **108**(46): p. 17886-17892.

[3] Warshay, M. and Prokopius, P. R., *The fuel cell in space: yesterday, today and tomorrow.* Journal of Power Sources, 1990. **29**(1): p. 193-200.

[4] Gottesfeld, S. and Zawodzinski Jr, T. A., *Polymer electrolyte fuel cells*, in *Advances in Electrochemical Science and Engineering*, R.C. Alkire and C.W. Tobias, Editors. 1997, John Wiley & Sons.

[5] Barbir, F., *PEM fuel cells: Theory and Practice*. 2005: Elsevier Academic Press.

[6] *Multi-Year research, development and demonstration plan.* 2012, U.S. Department of Energy: Office of Energy Efficiency and Renewable Energy.

[7] Spiegel, C., *PEM fuel cell modeling and simulaion using MATLAB*. 2008: Academic Press.

[8] Gasteiger, H. A., Kocha, S. S., Sompalli, B., and Wagner, F. T., *Activity benchmarks and requirements for Pt, Pt-alloy, and non-Pt oxygen reduction catalysts for PEMFCs.* Applied Catalysis B: Environmental, 2005. **56**(1–2): p. 9-35.

[9] Stamenkovic, V. R., Mun, B. S., Arenz, M., Mayrhofer, K. J. J., Lucas, C. A., Wang, G., Ross, P. N., and Markovic, N. M., *Trends in electrocatalysis on extended and nanoscale Pt-bimetallic alloy surfaces*. Nature materials, 2007. **6**(3): p. 241-247.

[10] Stamenkovic, V. R. and Markovic, N. M., *Electrochemistry at well-characterized bimetallic surfaces*, in *Fuel cell catalysis: A surface science approach*, M.T.M. Koper, Editor. 2009, John Wiley & Sons. p. 245-271.

[11] Xu, Y., Shao, M., Mavrikakis, M., and Adzic, R. R., *Recent developments in the electrocatalysis of the $O_2$ reduction reaction*, in *Fuel cell catalysis: a surface science approach*, M.T.M. Koper, Editor. 2009, John Wiley & Sons. p. 271-317.

[12] Ferreira, P. J., la O', G. J., Shao-Horn, Y., Morgan, D., Makharia, R., Kocha, S., and Gasteiger, H. A., I*nstability of Pt/C electrocatalysts in proton exchange membrane fuel cells: A mechanistic investigation*. Journal of The Electrochemical Society, 2005. **152**(11): p. A2256-A2271.

[13] Mayrhofer, K. J. J., Blizanac, B. B., Arenz, M., Stamenkovic, V. R., Ross, P. N., and Markovic, N. M., T*he impact of geometric and surface electronic properties of Pt-catalysts on the particle size effect in electrocatalysis*. The Journal of Physical Chemistry B, 2005. **109**(30): p. 14433-14440.

[14] Shao-Horn, Y., Sheng, W. C., Chen, S., Ferreira, P. J., Holby, E. F., and Morgan, D., *Instability of supported platinum nanoparticles in low-temperature fuel cells*. Topics in Catalysis, 2007. **46**(3): p. 285-305.

[15] Mayrhofer, K. J. J., Meier, J. C., Ashton, S. J., Wiberg, G. K. H., Kraus, F., Hanzlik, M., and Arenz, M., *Fuel cell catalyst degradation on the nanoscale*. Electrochem. Commun., 2008. **10**(8): p. 1144-1147.

[16] Meier, J. C., Galeano, C., Katsounaros, I., Topalov, A. A., Kostka, A., Schüth, F., and Mayrhofer, K. J. J., *Degradation mechanisms of Pt/C fuel cell catalysts under simulated start–stop conditions*. ACS Catal., 2012. **2**(5): p. 832-843.

[17] Cherevko, S., Topalov, A. A., Zeradjanin, A. R., Keeley, G. P., and Mayrhofer, K. J. J., *Temperature-dependent dissolution of polycrystalline platinum in sulfuric acid electrolyte*. Electrocatalysis, 2014. **5**(3): p. 235-240.

[18] Meier, J. C., Galeano, C., Katsounaros, I., Witte, J., Bongard, H. J., Topalov, A. A., Baldizzone, C., Mezzavilla, S., Schüth, F., and Mayrhofer, K. J. J., *Design criteria for stable Pt/C fuel cell catalysts*. Beilstein Journal of Nanotechnology, 2014. **5**: p. 44-67.

[19] Foelske-Schmitz, A., Peitz, A., Guzenko, V. A., Weingarth, D., Scherer, G. G., Wokaun, A., and Kötz, R., *In situ electrochemical STM study of platinum nanodot arrays on highly oriented pyrolythic graphite prepared by electron beam lithography*. Surface Science, 2012. **606**(23–24): p. 1922-1933.

[20] Xing, L., Hossain, M. A., Tian, M., Beauchemin, D., Adjemian, K. T., and Jerkiewicz, G., *Platinum electro-dissolution in acidic media upon potential cycling*. Electrocatalysis, 2014. **5**(1): p. 96-112.

[21] Arulmozhi, N., Esau, D., Lamsal, R. P., Beauchemin, D., and Jerkiewicz, G., *Structural transformation of monocrystalline platinum electrodes upon electro-oxidation and electro-dissolution*. ACS Catalysis, 2018. DOI: 10.1021/acscatal.8b00319

[22] Tahmasebi, S., Hossain, M. A., and Jerkiewicz, G., *Corrosion behavior of platinum in aqueous $H_2SO_4$ solution: Part 1—Influence of the potential scan rate and the dissolved gas*. Electrocatalysis, 2018. **9**(2): p. 172-181.

[23] Tahmasebi, S., Jerkiewicz, G., Baranton, S., Coutanceau, C., Furuya, Y., and Ohma, A., *How stable are spherical platinum nanoparticles applied to fuel cells?* The Journal of Physical Chemistry C, 2018. **122**(22): p. 11765-11776.

[24] Alsabet, M., Grden, M., and Jerkiewicz, G., *Comprehensive study of the growth of thin oxide layers on Pt electrodes under well-defined temperature, potential, and time conditions*. Journal of Electroanalytical Chemistry, 2006. **589**(1): p. 120-127.

[25] Boehm, H. P., *Some aspects of the surface chemistry of carbon blacks and other carbons*. Carbon, 1994. **32**(5): p. 759-769.

[26] Ban, S., Malek, K., Huang, C., and Liu, Z., *A molecular model for carbon black primary particles with internal nanoporosity*. Carbon, 2011. **49**(10): p. 3362-3370.

[27] Kercher, A. K. and Nagle, D. C., *Microstructural evolution during charcoal carbonization by X-ray diffraction analysis*. Carbon, 2003. **41**(1): p. 15-27.

[28] Lordi, V., Yao, N., and Wei, J., *Method for supporting platinum on single-walled carbon nanotubes for a selective hydrogenation catalyst*. Chemistry of Materials, 2001. **13**(3): p. 733-737.

[29] Breuer, O. and Sundararaj, U., *Big returns from small fibers: A review of polymer/carbon nanotube composites*. Polymer Composites, 2004. **25**(6): p. 630-645.

[30] Coleman, J. N., Khan, U., Blau, W. J., and Gun'ko, Y. K., *Small but strong: A review of the mechanical properties of carbon nanotube–polymer composites*. Carbon, 2006. **44**(9): p. 1624-1652.

[31] Tian, Z. Q., Jiang, S. P., Liang, Y. M., and Shen, P. K., *Synthesis and characterization of platinum catalysts on multiwalled carbon nanotubes by intermittent microwave irradiation for fuel cell applications*. The Journal of Physical Chemistry B, 2006. **110**(11): p. 5343-5350.

[32] Zhu, G., Zhang, X., Gai, P., Zhang, X., and Chen, J., *β-Cyclodextrin non-covalently functionalized single-walled carbon nanotubes bridged by 3, 4, 9, 10-perylene tetracarboxylic acid for ultrasensitive electrochemical sensing of 9-anthracenecarboxylic acid*. Nanoscale, 2012. **4**(18): p. 5703-5709.

[33] Golberg, D., Bando, Y., Han, W., Kurashima, K., and Sato, T., *Single-walled B-doped carbon, B/N-doped carbon and BN nanotubes synthesized from single-walled carbon nanotubes through a substitution reaction*. Chemical Physics Letters, 1999. **308**(3–4): p. 337-342.

[34] Chen, Z., Higgins, D., Tao, H., Hsu, R. S., and Chen, Z., *Highly active nitrogen-doped carbon nanotubes for oxygen reduction reaction in fuel cell applications*. The Journal of Physical Chemistry C, 2009. **113**(49): p. 21008-21013.

[35] Qu, L., Liu, Y., Baek, J.-B., and Dai, L., *Nitrogen-doped graphene as efficient metal-free electrocatalyst for oxygen reduction in fuel cells*. ACS Nano, 2010. **4**(3): p. 1321-1326.

[36] Chen, S., Bi, J., Zhao, Y., Yang, L., Zhang, C., Ma, Y., Wu, Q., Wang, X., and Hu, Z., *Nitrogen-doped carbon nanocages as efficient metal-free electrocatalysts for oxygen reduction reaction*. Advanced Materials, 2012. **24**(41): p. 5593-5597.

[37] Heidenreich, R. D., Hess, W. M., and Ban, L. L., *A test object and criteria for high resolution electron microscopy*. Journal of Applied Crystallography, 1968. **1**(1): p. 1-19.

[38] Donnet, J.-B., *Fifty years of research and progress on carbon black*. Carbon, 1994. **32**(7): p. 1305-1310.

[39] Donnet, J. B., *Structure and reactivity of carbons: From carbon black to carbon composites*. Carbon, 1982. **20**(4): p. 267-282.

[40] Ávila-Brande, D., Katcho, N. A., Urones-Garrote, E., Gómez-Herrero, A., Landa-Cánovas, A. R., and Otero-Díaz, L. C., *Nano-structured carbon obtained by chlorination of NbC*. Carbon, 2006. **44**(4): p. 753-761.

[41] Peitz, A., *Degradation mechanisms of electrocatalysts used in polymer electrolyte fuel cells*, in *Department of Chemistry and Applied Biosciences*. 2011, ETH Zurich: ETH Zurich.

[42] Zhou, Y., Holme, T., Berry, J., Ohno, T. R., Ginley, D., and O'Hayre, R., *Dopant-induced electronic structure modification of HOPG surfaces: Implications for high activity fuel cell catalysts*. The Journal of Physical Chemistry C, 2009. **114**(1): p. 506-515.

[43] Kinoshita, K., *Carbon: Electrochemical and physicochemical properties*. A Wiley-Interscience publication. 1988: Wiley.

[44] Aktary, M., Lee, C. E., Xing, Y., Bergens, S. H., and McDermott, M. T., *Surface-directed deposition of platinum nanostructures on graphite by chemical vapor deposition*. Langmuir, 2000. **16**(14): p. 5837-5840.

[45] Mu, P., Haolin, T., Shichun, M., and Runzhang, Y., *Synthesis of platinum/multi-wall carbon nanotube catalysts*. Journal of materials research, 2004. **19**(8): p. 2279-2284.

[46] Rajalakshmi, N., Ryu, H., Shaijumon, M. M., and Ramaprabhu, S., *Performance of polymer electrolyte membrane fuel cells with carbon nanotubes as oxygen reduction catalyst support material*. Journal of Power Sources, 2005. **140**(2): p. 250-257.

[47] Wu, B., Hu, D., Kuang, Y., Yu, Y., Zhang, X., and Chen, J., *High dispersion of platinum–ruthenium nanoparticles on the 3, 4, 9, 10-perylene tetracarboxylic acid-functionalized carbon nanotubes for methanol electro-oxidation*. Chem. Commun., 2011. **47**(18): p. 5253-5255.

[48] Snoeyink, V. L. and Weber, W. J., *The surface chemistry of active carbon; A discussion of structure and surface functional groups*. Environmental Science & Technology, 1967. **1**(3): p. 228-234.

[49] Boehm, H. P., Diehl, E., Heck, W., and Sappok, R., *Surface oxides of carbon*. Angewandte Chemie International Edition in English, 1964. **3**(10): p. 669-677.

[50] Szabó, T., Berkesi, O., Forgó, P., Josepovits, K., Sanakis, Y., Petridis, D., and Dékány, I., *Evolution of surface functional groups in a series of progressively oxidized graphite oxides*. Chemistry of Materials, 2006. **18**(11): p. 2740-2749.

[51] Dreyer, D. R., Park, S., Bielawski, C. W., and Ruoff, R. S., *The chemistry of graphene oxide*. Chemical Society Reviews, 2010. **39**(1): p. 228-240.

[52] Boehm, H. P., *Surface oxides on carbon and their analysis: A critical assessment*. Carbon, 2002. **40**(2): p. 145-149.

[53] Pandolfo, A. G. and Hollenkamp, A. F., *Carbon properties and their role in supercapacitors*. Journal of Power Sources, 2006. **157**(1): p. 11-27.

[54] Stamatin, S. N., Borghei, M., Andersen, S. M., Veltze, S., Ruiz, V., Kauppinen, E., and Skou, E. M., *Influence of different carbon nanostructures on the electrocatalytic activity and stability of Pt supported electrocatalysts*. International Journal of Hydrogen Energy, 2014. **39**(16): p. 8215-8224.

[55] Aksoylu, A. E., Faria, J. L., Pereira, M. F. R., Figueiredo, J. L., Serp, P., Hierso, J. C., Feurer, R., Kihn, Y., and Kalck, P., *Highly dispersed activated carbon supported platinum catalysts prepared by OMCVD: A comparison with wet impregnated catalysts*. Applied Catalysis A: General, 2003. **243**(2): p. 357-365.

[56] Kim, U. J., Furtado, C. A., Liu, X., Chen, G., and Eklund, P. C., *Raman and IR spectroscopy of chemically processed single-walled carbon nanotubes*. Journal of the American Chemical Society, 2005. **127**(44): p. 15437-15445.

[57] Guha, A., Lu, W., Zawodzinski Jr, T. A., and Schiraldi, D. A., *Surface-modified carbons as platinum catalyst support for PEM fuel cells*. Carbon, 2007. **45**(7): p. 1506-1517.

[58] Yu, X. and Ye, S., *Recent advances in activity and durability enhancement of Pt/C catalytic cathode in PEMFC: Part I. Physico-chemical and electronic interaction between Pt and carbon support, and activity enhancement of Pt/C catalyst*. Journal of Power Sources, 2007. **172**(1): p. 133-144.

[59] Schönfelder, R., Avilés, F., Knupfer, M., Azamar-Barrios, J. A., González-Chi, P. I., and Rümmeli, M. H., *Influence of architecture on the Raman spectra of acid-treated carbon nanostructures*. Journal of Experimental Nanoscience, 2014. **9**(9): p. 931-941.

[60] Gritschneder, S., Becker, C., Wandelt, K., and Reichling, M., *Disorder or complexity? Understanding a nanoscale template structure on alumina*. Journal of the American Chemical Society, 2007. **129**(16): p. 4925-4928.

[61] Hepel, M., *Electrode-Solution interface studied with electrochemical quartz crystal nanobalance*, in *Interfacial Electrochemistry: Theory, Experiment, and Applications*, A. Wieckowski, Editor. 1999, Marcel Dekker, Inc.: New York.

[62] Bottom, V. E., *Introduction to quartz crystal unit design*. Electrical-Computer Science and Engineering Series. 1982: Van Nostrand Reinhold.

[63] Lichter, J. A. Crystals and Oscillators, JL9113 Rev. C. [cited 2018, 11 Jan]; Available from: http://www.nelfc.com/pdf/pdfapp/9113.pdf.

[64] O'Sullivan, C. K. and Guilbault, G. G., *Commercial quartz crystal microbalances – theory and applications*. Biosensors and Bioelectronics, 1999. 14(8): p. 663-670.

[65] Sauerbrey, G., *Verwendung von Schwingquarzen zur Wägung dünner Schichten und zur Mikrowägung*. Zeitschrift für Physik, 1959. 155(2): p. 206-222.

[66] Jerkiewicz, G., Vatankhah, G., Zolfaghari, A., and Lessard, J., *Analysis of the mass response of the electrochemical quartz-crystal nanobalance in horizontal and vertical geometry*. Electrochemistry Communications, 1999. **1**(9): p. 419-424.

[67] Vatankhah, G., Lessard, J., Jerkiewicz, G., Zolfaghari, A., and Conway, B. E., *Dependence of the reliability of electrochemical quartz-crystal nanobalance mass responses on the calibration constant, $C_f$: analysis of three procedures for its determination*. Electrochimica acta, 2003. **48**(11): p. 1613-1622.

[68] Koh, W., Kutner, W., Jones, M. T., and Kadish, K. M., *An improved holder for the electrochemical quartz crystal microbalance and its cyclic voltammetry characteristics*. Electroanalysis, 1993. **5**(3): p. 209-214.

[69] Bizet, K., Gabrielli, C., and Perrot, H., *Immunodetection by quartz crystal microbalance*. Applied Biochemistry and Biotechnology, 2000. **89**(2): p. 139.

[70] Jeffrey, C. A., Storr, W. M., and Harrington, D. A., *Electrochemical quartz-crystal microbalance study of silver and copper electrodeposition on bare and iodine-covered platinum electrodes*. Journal of Electroanalytical Chemistry, 2004. **569**(1): p. 61-70.

[71] Ratieuville, Y., Viers, P., Alexandre, J., and Durand, G., *A new electrochemical cell adapted to quartz crystal microbalance measurements*. Electrochemistry Communications, 2000. **2**(12): p. 839-844.

[72] Kim, J. and Jerkiewicz, G., *Influence of the surface roughness of platinum electrodes on the calibration of the electrochemical quartz-crystal nanobalance*. Analytical Chemistry, 2017. **89**(14): p. 7462-7469.

[73] Kolb, D. M., Przasnyski, M., and Gerischer, H., *Underpotential deposition of metals and work function differences*. Journal of Electroanalytical Chemistry and Interfacial Electrochemistry, 1974. **54**(1): p. 25-38.

[74] Batina, N., Will, T., and Kolb, D. M., *Study of the initial stages of copper deposition by in situ scanning tunnelling microscopy*. Faraday Discussions, 1992. **94**: p. 93-106.

[75] Hölzle, M. H., Retter, U., and Kolb, D. M., T*he kinetics of structural changes in Cu adlayers on Au (111)*. Journal of Electroanalytical Chemistry, 1994. **371**(1-2): p. 101-109.

[76] Magnussen, O. M., Hotlos, J., Beitel, G., Kolb, D. M., and Behm, R. J., *Atomic structure of ordered copper adlayers on single-crystalline gold electrodes*. Journal of Vacuum Science & Technology B: Microelectronics and Nanometer Structures Processing, Measurement, and Phenomena, 1991. **9**(2): p. 969-975.

[77] Hepel, M., Kanige, K., and Bruckenstein, S., *In situ underpotential deposition study of lead on silver using the electrochemical quartz crystal microbalance*. Journal of Electroanalytical Chemistry and Interfacial Electrochemistry, 1989. **266**(2): p. 409-421.

[78] Swathirajan, S. and Bruckenstein, S., *Interpretation of the potentiodynamic response during the underpotential deposition of silver on polycrystalline gold*. Journal of Electroanalytical Chemistry and Interfacial Electrochemistry, 1983. **146**(1): p. 137-155.

[79] Marković, N. M., Gasteiger, H. A., Lucas, C. A., Tidswell, I. M., and Ross, P. N., T*he effect of chloride on the underpotential deposition of copper on Pt(111): AES, LEED, RRDE, and X-ray scattering studies*. Surface Science, 1995. **335**: p. 91-100.

[80] Markovic, N. M., Gasteiger, H. A., and Ross, P. N., Jr., *Copper electrodeposition on Pt(111) in the presence of chloride and (bi)sulfate: Rotating ring-Pt(111) disk electrode studies*. Langmuir, 1995. **11**(10): p. 4098-4108.

[81] Marković, N. M., Lucas, C. A., Gasteiger, H. A., and Ross, P. N., *The structure of adsorbed bromide concurrent with the underpotential deposition (UPD) of Cu on Pt(111)*. Surface Science, 1997. **372**(1): p. 239-254.

[82] Wilde, C. P. and Zhang, M., *Adsorption and underpotential deposition of lead at electrodeposited platinum electrodes*. Journal of Electroanalytical Chemistry, 1992. **327**(1): p. 307-320.

[83] Clavilier, J., Feliu, J. M., and Aldaz, A., *An irreversible structure sensitive adsorption step in bismuth underpotential deposition at platinum electrodes*. Journal of electroanalytical chemistry and interfacial electrochemistry, 1988. **243**(2): p. 419-433.

[84] Clavilier, J., Orts, J. M., Gomez, R., Feliu, J. M., and Aldaz, A., *Comparison of electrosorption at activated polycrystalline and Pt (531) kinked platinum electrodes: surface voltammetry and charge displacement on potentiostatic CO adsorption*. Journal of Electroanalytical Chemistry, 1996. **404**(2): p. 281-289.

[85] Danilov, A. I., Molodkina, E. B., Polukarov, Y. M., Climent, V., and Feliu, J. M., *Active centers for Cu UPD–OPD in acid sulfate solution on Pt (111) electrodes*. Electrochimica acta, 2001. **46**(20): p. 3137-3145.

[86] Feliu, J. M., Fernandez-Vega, A., Orts, J. M., and Aldaz, A., *The behaviour of lead and bismuth adatoms on well-defined platinum surfaces*. Journal de chimie physique, 1991. **88**: p. 1493-1518.

[87] Gomez, R., Yee, H. S., Bommarito, G. M., Feliu, J. M., and Abrun, H. D., *Anion effects and the mechanism of Cu UPD on Pt (111): X-ray and electrochemical studies*. Surface science, 1995. **335**: p. 101-109.

[88] Kuzume, A., Herrero, E., Feliu, J. M., Nichols, R. J., and Schiffrin, D. J., *Copper underpotential deposition at high index single crystal surfaces of Au*. Journal of Electroanalytical Chemistry, 2004. **570**(2): p. 157-161.

[89] Boxley, C. J., White, H. S., Lister, T. E., and Pinhero, P. J., *Electrochemical deposition and reoxidation of Au at highly oriented pyrolytic graphite. Stabilization of Au nanoparticles on the upper plane of step edges*. The Journal of Physical Chemistry B, 2003. 107(2): p. 451-458.

[90] Green, C. L. and Kucernak, A., *Determination of the platinum and ruthenium surface areas in platinum− ruthenium alloy electrocatalysts by underpotential deposition of copper. I. Unsupported catalysts*. The Journal of Physical Chemistry B, 2002. **106**(5): p. 1036-1047.

[91] Herrero, E., Buller, L. J., and Abruña, H. D., *Underpotential deposition at single crystal surfaces of Au, Pt, Ag and other materials*. Chemical Reviews, 2001. **101**(7): p. 1897-1930.

[92] Herzog, G. and Arrigan, D. W. M., *Determination of trace metals by underpotential deposition–stripping voltammetry at solid electrodes*. Trends in Analytical Chemistry, 2005. **24**(3): p. 208-217.

[93] Jaya, S., Rao, T. P., and Rao, G. P., *Underpotential deposition studies of copper on glassy carbon*. Journal of Chemical Sciences, 1986. **97**(5): p. 581-586.

[94] Kibler, L. A., Soliman, K. A., Plumer, A., Wildi, C. S., Bringley, E., Mueller, J. E., and Jacob, T., *Electrodeposition of Ag overlayers onto Pt(111): Structural, electrochemical and electrocatalytic properties*. Electrocatalysis, 2017. **8**(6): p. 605-615.

[95] Mascaro, L. H., Santos, M. C., Machado, S. A. S., and Avaca, L. A., *Underpotential deposition of silver on polycrystalline platinum studied by cyclic voltammetry and rotating ring-disc techniques*. Journal of the Chemical Society, Faraday Transactions, 1997. **93**(22): p. 3999-4003.

[96] Obretenov, W., Schmidt, U., Lorenz, W. J., Staikov, G., Budevski, E., Carnal, D., Müller, U., Siegenthaler, H., and Schmidt, E., *Underpotential deposition and electrocrystallization of metals an atomic view by scanning tunneling microscopy*. Journal of The Electrochemical Society, 1993. **140**(3): p. 692-703.

[97] Sudha, V. and Sangaranarayanan, M. V., *Underpotential deposition of metals: Structural and thermodynamic considerations*. The Journal of Physical Chemistry B, 2002. **106**(10): p. 2699-2707.

[98] Sudha, V. and Sangaranarayanan, M. V., *Underpotential deposition of metals – Progress and prospects in modelling*. Journal of Chemical Sciences, 2005. **117**(3): p. 207-218.

[99] Faraday, M., VI. *Experimental researches in electricity.—Sixth series*. Philosophical Transactions of the Royal Society of London, 1834. **124**: p. 77-122.

[100] Pletcher, D., *A first course in electrode processes*. 2nd edition ed. 2009: The Royal Society of Chemistry.

[101] Huang, J., Malek, A., Zhang, J., and Eikerling, M. H., *Non-monotonic surface charging behavior of platinum: A paradigm change*. The Journal of Physical Chemistry C, 2016. **120**(25): p. 13587-13595.

[102] Bard, A. J. and Faulkner, L. R., *Electrochemical methods: Fundamentals and applications*. 2nd ed. 2001: John Wiley & Sons, Inc.

# Chapter 2
# Highly Orientated Pyrolytic Graphite - A Model Substrate to Study Anchoring of Pt on Carbon

## 2.1 Introduction

The polymer electrolyte fuel cell (PEFC) is a promising energy conversion device that is seeing slow breakthrough into the marketplace. While this technology is commercially viable, there are many drawbacks preventing the technology being catapulted from the niche market into the mainstream market [1,2].

One challenge associated with the PEFC, is the electrocatalyst. While, much focus is devoted to studying PGM-free electrocatalysts [3-5] and alternative supports [6,7], the issue of understanding the interactions between Pt and carbon has not been thoroughly investigated. In order to improve our understanding of the electrocatalyst, we need to understand the metal support interactions, with a particular emphasis on the mobility of the active metal across the support surface. This is a topic that is widely studied in the field of heterogeneous catalysis [8-10], but has only been touched on in the field of electrocatalysis.

In this chapter, focus will be on using a model substrate to study Pt mobility on carbon. Basal plane highly orientated pyrolytic graphite (HOPG) will be used and modified with various oxygen terminated groups. The question of whether or not oxygen impurities on the surface of carbon influence the anchoring of Pt will be explored. This will be investigated by studying the mobility of Pt on the modified and unmodified HOPG surfaces by load cycling accelerated durability tests.

## 2.2 Experimental Methods

All electrochemical measurements were conducted using a Bio-Logic SP-200 potentiostat, in a home-built Faraday cage and vibration free table. The packaged EC-Lab v11.1x software was used to control the instrument.

### 2.2.1 Electrodes

A custom-built, two-compartment cell (developed by Prof Jerkiewicz) was used and cleaned by submerging in NOCHROMIX® (Godax Laboratories, Inc.) overnight. The working electrode consisted of 1 $cm^2$, 200 µm thick HOPG disks (Optigraph GmbH, Berlin). This was attached to a conventional glassy carbon (GC) electrode using a carbon-Nafion® (Ion Power) paste. The HOPG surface was modified by refluxing in Fenton's reagent for 24 hours at 80 °C [11] or refluxing in a 1:1 ratio of 5 N $HNO_3$ and 5 N $H_2SO_4$ for 24 hours at 120 °C [12], the constant time and temperatures were chosen to ensure the concentration of potential anchor sites on the surface is maximised. The hydroxyl modified HOPG is referred to as HOPG-H, with the acid treated HOPG samples referred to as HOPG-A, and the pristine HOPG samples referred to as HOPG-P. Pt was then deposited onto the modified and unmodified surfaces at loadings of 20 $\mu g.cm^{-2}$ and 50 $\mu g.cm^{-2}$ by DC magnetron sputtering (PVD Products, USA). This was accomplished by using a Pt sputtering target (1.5" diameter x ⅛" thick) obtained from ACI Alloys (USA) having a purity of 99.95%. Prior to sputtering, the vacuum chamber of the sputtering apparatus was pumped down to a base pressure of approximately $5 \times 10^{-7}$ Torr. Sputtering of Pt, under an Ar plasma, was conducted at a chamber pressure of 8 mTorr and an Ar flow of 15 sccm. The sputtering rate ($nm.min^{-1}$) of Pt was calibrated as described by Falch *et al.* [13] with minimal deviation in the sputtered layer from sample to sample. The substrates were positioned onto a stainless-steel tray that slots into a housing fitted with a computer controlled XY motor below a fixed aperture, allowing for dedicated sputtering of individual samples.

A reversible hydrogen electrode (RHE) using Pt foil (Alfa Aesar, 99.999%) was used as the reference electrode and a Pt mesh (Alfa Aesar, 99.99%) as the counter electrode.

### 2.2.2 Electrochemical Testing

Prior to conducting electrochemical measurements on HOPG, cyclic voltammograms ($i$ vs $E$) of polycrystalline Pt were measured in aqueous 0.5 M $H_2SO_4$ prepared from 99.999 wt.% $H_2SO_4$ (Sigma Aldrich) and 18.2 MΩ.cm nano-pure water. All measurements were carried out at room temperature and under an inert Ar atmosphere (99.999%, Air Products). The electric potential was cycled between 0.05 and 1.50 V vs RHE to ensure cleanliness and reproducible functioning of the electrochemical setup.

Pt/HOPG samples were cycled between 0.00 and 1.50 V vs RHE for 30 cycles at 250 $mV.s^{-1}$, then between 0.00 and 1.20 V vs RHE for 100 cycles at 250 $mV.s^{-1}$. These initial cycles were run to ensure the electrode surface was cleaned and was sufficiently conditioned before running accelerated durability tests.

With the focus of this study on Pt mobility, only load cycling accelerated durability tests (ADT) were considered. Once the cleaning cyclic voltammograms were completed three cyclic voltammograms were recorded between 0.05 and 1.20 V vs RHE at 50 $mV.s^{-1}$. The load cycling protocol described in Ohma *et al.* [14] was employed, where potential is held at 0.60 V vs RHE for 3 s, then stepped to 1.00 V vs RHE for 3 s, and finally stepped back down to 0.60 V vs RHE for 3 s. This process was repeated 5000 times, with cyclic voltammograms, as described earlier in this paragraph, recorded at intervals.

The potential of zero total charge (PZTC) was recorded before and after the ADTs to ensure that the process did not alter the support. The method of differential capacitance was employed as described in Shao *et al.* [15] and Lockett *et al.* [16]. The potential was swept between -0.10 and 0.75 V vs RHE at intervals of 42.5 mV, impedance was measured between

5 kHz and 6 Hz at each potential interval, with nine points per decade.

Finally, to confirm the oxidation of HOPG by various treatment methods and changes in the electronic states of the carbon, cyclic voltammograms (CVs) using the ferri/ferrocyanide redox couple were run. A solution of 1 mM $K_4Fe(CN)_6$ (Sigma Aldrich) in 1 M KCl (Merck) was prepared. The electric potential was cycled between 0.00 and 1.20 V vs RHE at scan rates of 100, 75, 50, 25, and 20 $mV.s^{-1}$.

### 2.2.3 Physical Characterisation

Scanning electron microscopy (SEM) measurements were conducted with a FEI Nova NanoSEM 230 with a beam energy of 15 keV - 20 keV and spot size of 3.0 under vacuum.

X-ray diffraction (XRD) measurements were taken using a Bruker D2 Phaser in the Bragg-Brentano geometry with a Co anode ($\lambda$ = 1.79026 Å), primarily using a $2\theta$ range of 20 - 90° with 0.0274° steps. Samples were placed in a zero-background sample holder and the sample was placed such that they were in line with a straight edge across the holder. The measurement was repeated at various angles ($\Phi$) about the vector normal to the sample surface.

X-Ray Reflectometry (XRR) measurements were taken using a Bruker D8 Discover with a Cu anode ($\lambda$ = 1.54184 Å) and a symmetric $2\theta$ geometry between 0.0 and 4.5°. XRR measurements were taken at a step size of 0.02° at 5 s per step. The sample height displacements and offsets in $\omega$ (the angle between the detector and sample) were optimised for each measurement. Model fitting was performed manually based on a layer stack consisting of the Pt/HOPG sample to ensure a rapid and unambiguous convergence of the simulation towards a global minimum. This was followed by fit optimisation with the Levenberg-Marquardt [17,18] algorithm using Poisson or linear models.

X-ray photoelectron spectroscopy (XPS) measurements were carried out using a

monochromated Al source (1487.1 eV) and a SPECS PHOIBOS 150 hemispherical electron energy analyser. The overall experimental resolution was approximately 0.6 eV for all spectra. Some of the spectra were acquired on a KRATOS-SUPRA spectrometer at UNISA (Florida Science Campus, South Africa), using a monchromated Al source (1486.6 eV) having a base pressure of $1.2 \times 10^{-8}$ Torr. The surface of all samples was cleaned with a short cycle of Ar ion sputtering. This ranged from 30 to 120 s, with measurements taken at various intervals.

## 2.3 Results and Discussion

A systematic approach was taken to analyse the samples. First, HOPG samples were physically and electrochemically characterised without Pt deposition. Secondly, the characterisation of Pt/HOPG samples was done and then electrochemical measurements were completed. Lastly, the samples were re-characterised for their physical and electrochemical properties after accelerated durability tests.

### 2.3.1 HOPG Characterisation

Prior to the deposition of Pt on the chemically modified HOPG, the surface of HOPG-P, HOPG-H, and HOPG-A were probed to examine the environment for Pt deposition. First, scanning electron micrographs were obtained for the as received sample (HOPG-P in fig. 2.1a) and after the two treatment methods (HOPG-H in fig. 2.1b & c and HOPG-A in fig. 2.1d) as illustrated in fig. 2.1 below. It is clear, from fig. 2.1, that the chemical modifications had a significant effect on the morphology of HOPG. In fig. 2.1 (a), a fairly pristine representation of the as received HOPG (HOPG-P) sample surface is illustrated. While there are steps at intervals, much of the sample comprises of a smooth and homogenous surface.

The pristine HOPG underwent aggressive chemical modification as described in section 2.2.1, this is evident from the change in morphology seen between fig. 2.1 (a) and the treated samples in fig. 2.1 (b) - (d). The HOPG-H samples showed unusual morphologies, with

amorphous-like carbonaceous material on a fairly smooth surface as in fig. 2.1 (b). On the other hand, a certain degree of exfoliation and raised surfaces also appear on the HOPG-H samples, as indicated in fig. 2.1 (c). This is very peculiar behaviour and it is postulated that once the graphene layers exfoliate, they clump together forming the illustrated carbonaceous amorphous masses.

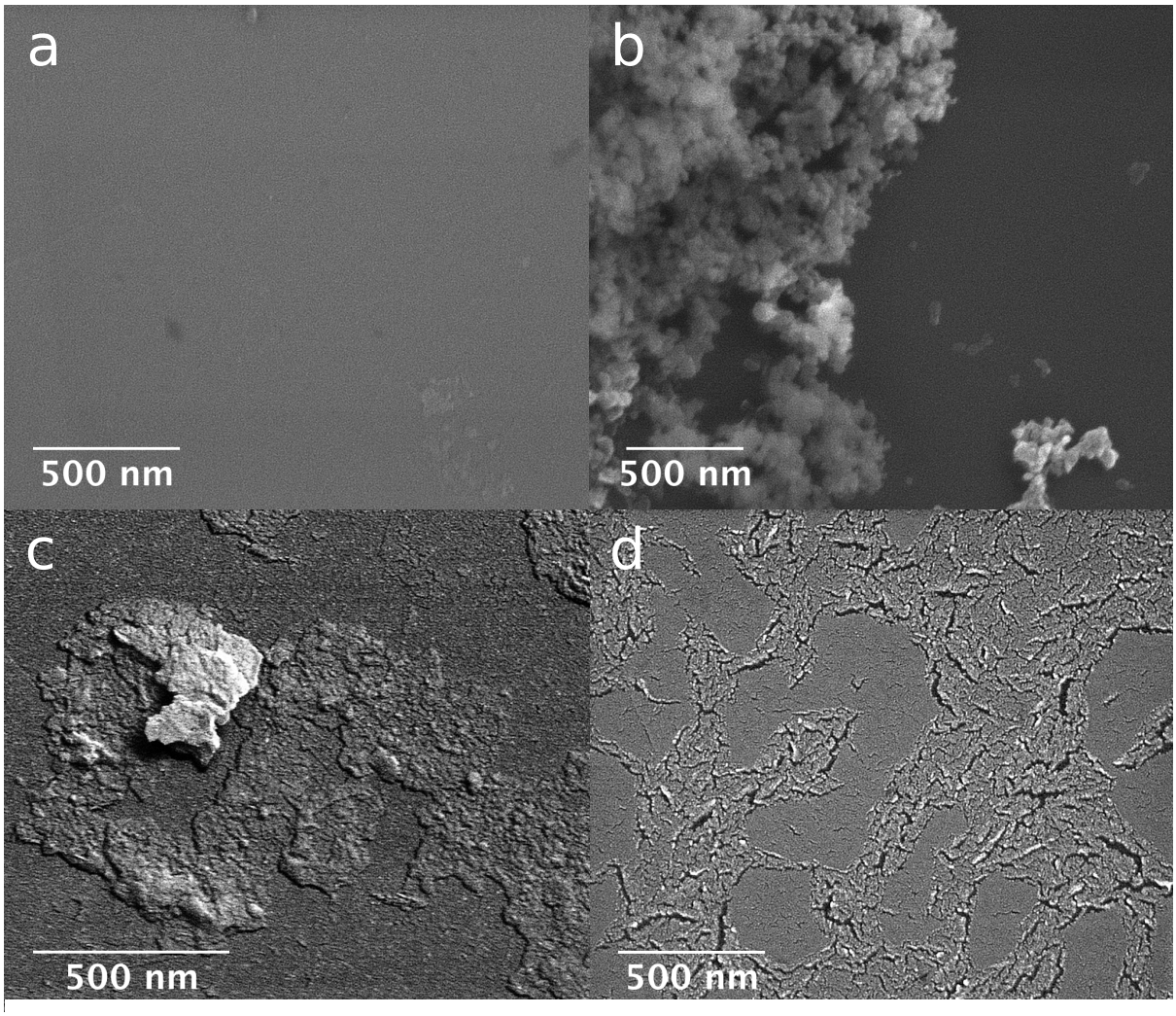


**Figure 2.1 SEM micrographs of (a) pristine HOPG at 20 keV and 150 000 magnification, (b), HOPG-H at 15 keV and 120 000 magnification, (c) HOPG-H at 18 keV and 200 000 magnification, and (d) HOPG-A at 20 keV at 150 000 magnification.**

Lastly, the acid-treated HOPG (HOPG-A) displayed different changes to its morphology, as compared to HOPG-H. The acid treatment appears to have attacked small defects in the graphene structures and created mild exfoliation by creating valleys and potentially forming edge sites, hence increasing surface roughness.

In order to obtain a better understanding of the surface chemistry, XPS was performed and the surface was etched with Ar plasma as described in section 2.2.3. This protocol was employed in order to gain insight into whether or not the oxygenation of the basal plane remained a surface phenomenon or penetrated into the bulk. In fig. 2.2 a survey spectrum of the three HOPG samples were compared before and after etching.

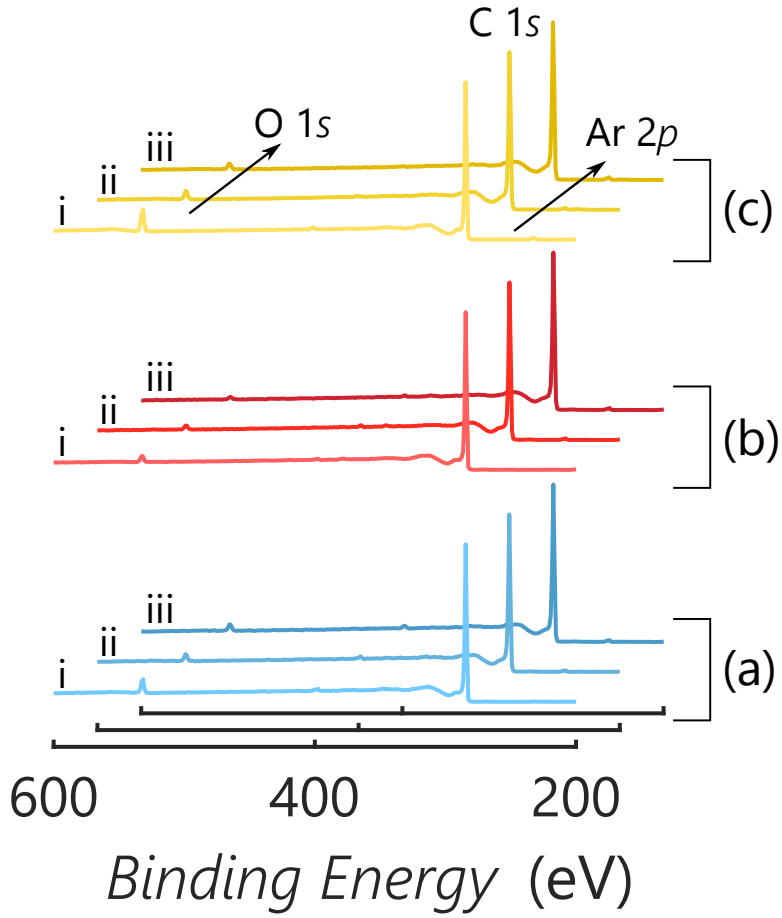


**Figure 2.2 XPS survey spectra of (a) HOPG-P, (b) HOPG-H, and HOPG-A. Spectra (i) represents samples as received, spectra (ii) represents samples after 60 s sputtering, spectra (iii) represents samples after 120 s sputtering. Bands at 532.4 eV, 284.4 eV, and 241.1 eV are assigned to O 1*s*, C 1*s*, and Ar 2*p*, respectively**

It is clear that with each repeat of sputtering, the O 1*s* band is reduced in HOPG-A (as seen in fig. 2.2c: i - iii). However, there is a low oxygen content for HOPG-H, lower than the surface oxygen present in HOPG-P, see fig. 2.2 (a) and (b). This further suggests that the chemical modification in Fenton's reagent appears to exfoliate the upper graphene layers of the HOPG.

However, this effect seems to be site specific, this is not observed throughout the entire sample, as illustrated in the SEM micrographs (fig. 2.1). Thus, the O 1*s* spectra is only significant for HOPG-A, before etching. Lastly, the prepared samples appear to be free of any appreciable contaminants, with only Ar implantation after sputtering [19]. However, this has no effect on observed electrochemical results.

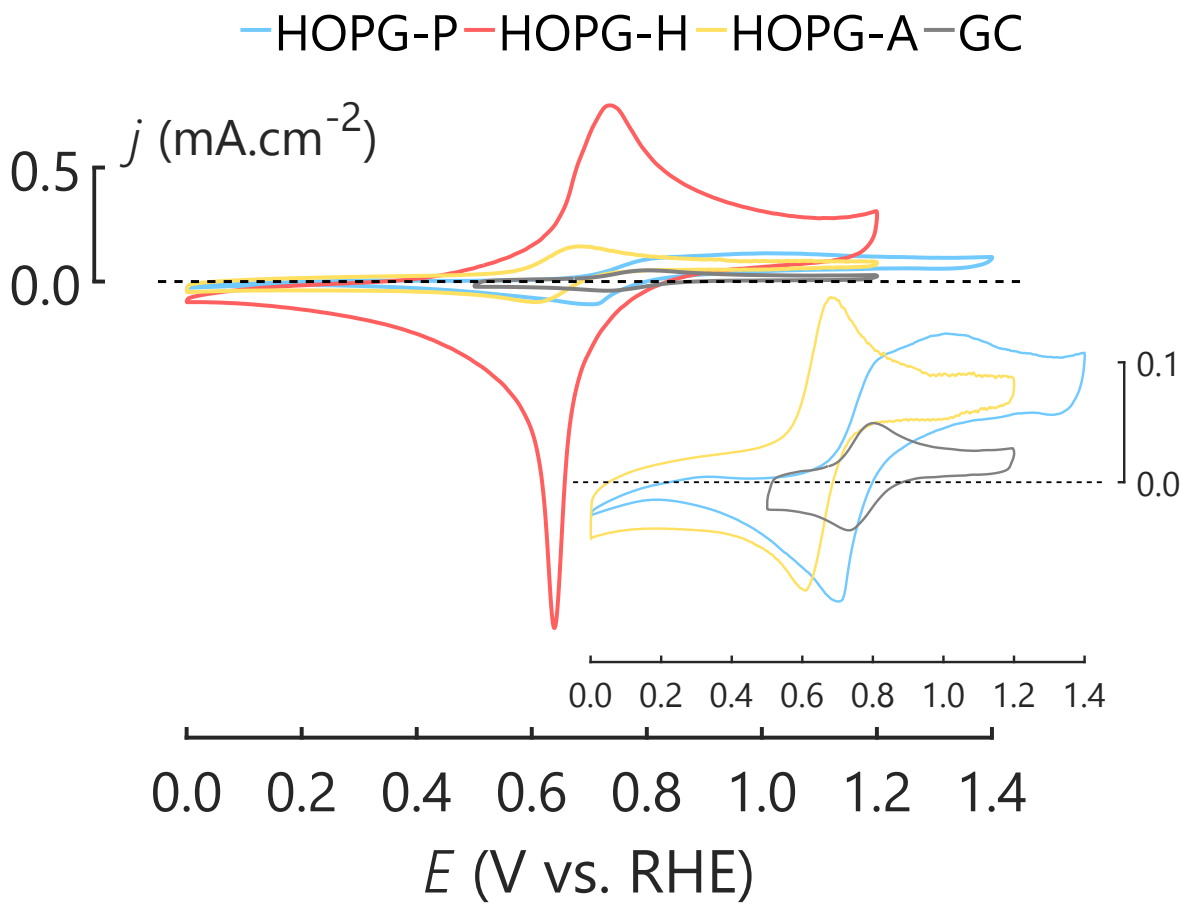


**Figure 2.3 Current responses of HOPG samples and glassy carbon (GC) electrodes in 1 mM $[Fe(CN)_6]^{4-}$ / 1 M $KCl_{(aq)}$ solution under Ar saturation and room temperature, with a sweep rate of 50 mV.s$^{-1}$**

The CVs of the ferri/ferrocyanide redox couple were studied for each of the HOPG substrates and a 50 nm alumina polished GC electrode, as shown in fig. 2.3. GC and HOPG-P are used as baselines to which surface modifications can be compared. From the corresponding CVs, an estimated electrode capacitance (*C*) [20] was determined using equation 2.1 below

$$|\Delta i| = AC\nu \quad (2.1)$$

where, $\Delta i$ is the current difference at a fixed potential in A, $A$ is the electrode geometric area in $cm^2$, $C$ is the capacitance in $F.cm^{-2}$, and $\nu$ is the scan rate in $V.s^{-1}$. The rate constant, $k^0$, was estimated using Nicholson's method [21] as outlined below

$$\psi = \frac{\left(\frac{D_O}{D_R}\right)^{\alpha/2} k^0}{\sqrt{(\pi D_O f \nu)}} \quad (2.2)$$

where, $D_O$ and $D_R$ are the diffusivities of the oxidised and reduced species respectively in $cm^2.s^{-1}$, $\alpha$ is the transfer coefficient, $k^0$ is the rate constant in $cm.s^{-1}$, and $f$ is equivalent to $F/RT$ or 38.92 $V^{-1}$ at 25 °C. $\Psi$ is a dimensionless rate parameter as described by Nicholson [21], whereby tabulated values (table 2.1) relating $\Delta E_p$ to $\Psi$ was developed in order to infer the rate constant, $k^0$.

**Table 2.1 Variation of $\Delta E_p$ with $\Psi$ at 25 °C. Reproduced from Bard & Faulkner [20]**

| $\Psi$ | $\Delta E_p$ (mV) |
|---|---|
| 20 | 61.0 |
| 7.0 | 63.0 |
| 6.0 | 64.0 |
| 5.0 | 65.0 |
| 4.0 | 66.0 |
| 3.0 | 68.0 |
| 2.0 | 72.0 |
| 1.0 | 84.0 |
| 0.75 | 92.0 |
| 0.50 | 105 |
| 0.35 | 121 |
| 0.25 | 141 |
| 0.10 | 212 |

As expected, HOPG-P surfaces show a large separation of the anodic and cathodic peak potentials, indicating a slow rate of electron transfer for the $[Fe(CN)6]^{4-/3-}$ couple. This has been postulated by Cline *et al.* [22] to be due to a lack of surface reactive sites at the basal plane of HOPG, which is not a suitable electron transfer structure. With the introduction of surface disorder, *i.e.* by chemical modification as discussed above, there is a significant increase in the rate constant as indicated in table 2.2 [22,23]. Furthermore, as seen in fig. 2.3, the broadening of the HOPG-P peaks ($E_{p,a}$ and $E_{p,c}$) and deviation from the classic "duck bill" shape, suggests that there are few sites for adsorption for the ferrocyanide ion and subsequent electron transfer.

**Table 2.2 Redox potential, kinetic data, and capacitance values for all samples in fig. 2.3**

| Substrate | $\Delta E_p$ (mV) | $k^0$ (cm.s$^{-1}$)[a] | C ($\mu$F.cm$^{-2}$) |
|---|---|---|---|
| HOPG-P | 306 | $5.0 \times 10^{-7}$ | 620 |
| HOPG-H | 95.2 | 0.0056 | 3,400 |
| HOPG-A | 78.4 | 0.012 | 1,000 |
| GC | 68.7 | 0.020 | 520 |

[a] $\alpha$ = 0.5, $D_O = D_R = 10^{-5}$ cm$^2$.s$^{-1}$

HOPG-H shows a five-fold increase in capacitance over HOPG-P, while HOPG-A shows about 1.5 times increase in capacitance over HOPG-P (table 2.2). These increases are most likely due to decreased conductivity of the chemically modified HOPG substrates. However, these chemical modifications have been successful in creating more adsorption sites for electron transfer to occur, as is evident by the decrease in $\Delta E_p$ and subsequent increase in $k^0$ [20-23].

From the above results, it is clear that the chemical modifications result in both morphological and chemical changes to the HOPG. The results further illustrate that there is possible exfoliation of the upper most graphene layers in HOPG-H, which is strongly supported by an insignificant O 1*s* band and the high capacitance resulting in a charge separation. There is an appreciable increase in capacitance in HOPG-A and this can be attributed to partial exfoliation, the creation of valleys, and regions of high $sp^3$ moieties to $sp^2$ moieties [22-25].

### 2.3.2 Pt/HOPG Characterisation

After the characterisation of the Pt-free HOPG samples, loadings of 20 $\mu$g.cm$^{-2}$ and 50 $\mu$g.cm$^{-2}$ were deposited by DC magnetron sputtering as described in section 2.3.1. In order to ensure that the correct loading of Pt was deposited, X-ray reflectometry (XRR) [26] was employed to determine the Pt layer thickness. Below (fig. 2.4), the XRR measurements for 20 $\mu$g.cm$^{-2}$ Pt/HOPG-H and 50 $\mu$g.cm$^{-2}$ Pt/HOPG-H are illustrated.

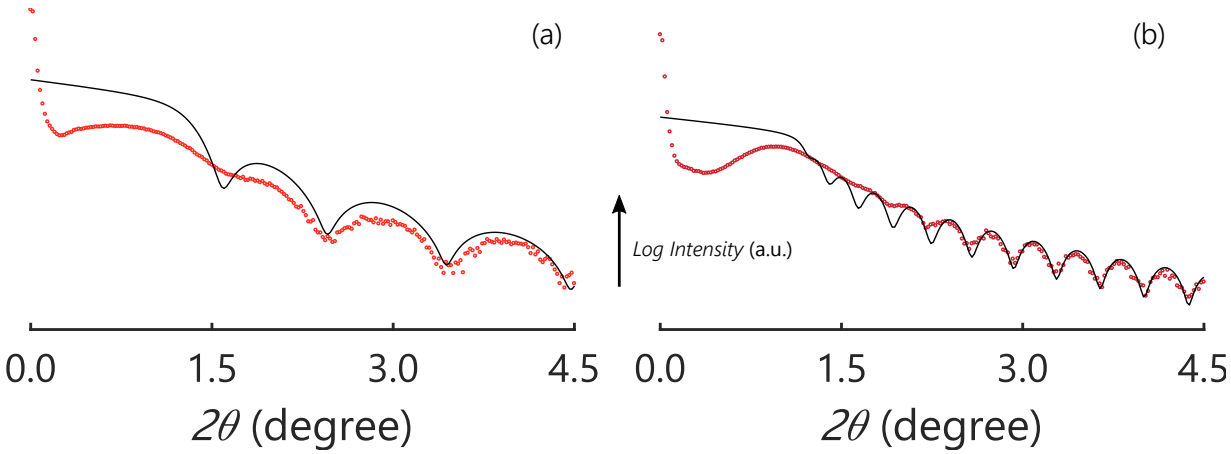


**Figure 2.4 X-ray reflectometry measurements (red dots) and model fit (black line) for (a) 20 $\mu$g.cm$^{-2}$ Pt/HOPG-H and (b) 50 $\mu$g.cm$^{-2}$ Pt/HOPG-H**

With increasing Pt thickness, we expect to see a decrease in the period of the Kiessig fringes [27]. From fig. 2.4, it is shown that the period of the Kiessig fringes have decreased on the 50 $\mu$g.cm$^{-2}$ Pt/HOPG-H, indicating that the increased loading has been deposited. A mathematical fit to the Kiessig fringes gives data on film thickness, density, and surface roughness. For this study, we fixed the density of Pt to 21.44 g.cm$^{-3}$ and did not include surface roughness optimisation in order to reduce unknown variables. There is good agreement between the film thickness calculated using the model and the experimental data for both the 20 $\mu$g.cm$^{-2}$ and 50 $\mu$g.cm$^{-2}$ Pt/HOPG-H samples, with little deviation from the desired loading (see table 2.3. below). Instances where the model is not superimposed over the experimental data is outside the scope of this work, however, slight shifts in Kiessig fringe periods gives an indication that the deposited film may not be uniform.

**Table 2.3 Desired vs Measured Pt film thickness as deposited by DC magnetron sputtering**

| Sample | Desired Thickness (nm) | Measured Thickness (nm) |
|---|---|---|
| 20 $\mu$g.cm$^{-2}$ Pt/HOPG-H | 9.32 | 8.19 |
| 50 $\mu$g.cm$^{-2}$ Pt/HOPG-H | 23.3 | 23.3 |

Following XRR, X-ray diffractometry (XRD) measurements were performed on all 20 $\mu$g.cm$^{-2}$ and 50 $\mu$g.cm$^{-2}$ Pt/HOPG samples, however, initial measurements did not show the expected Pt spectral positions for the 20 $\mu$g.cm$^{-2}$ samples. In order to eliminate any effects from the substrate, Pt at various loadings was deposited on an inert Si (100) wafer, as illustrated in fig. 2.5 below.

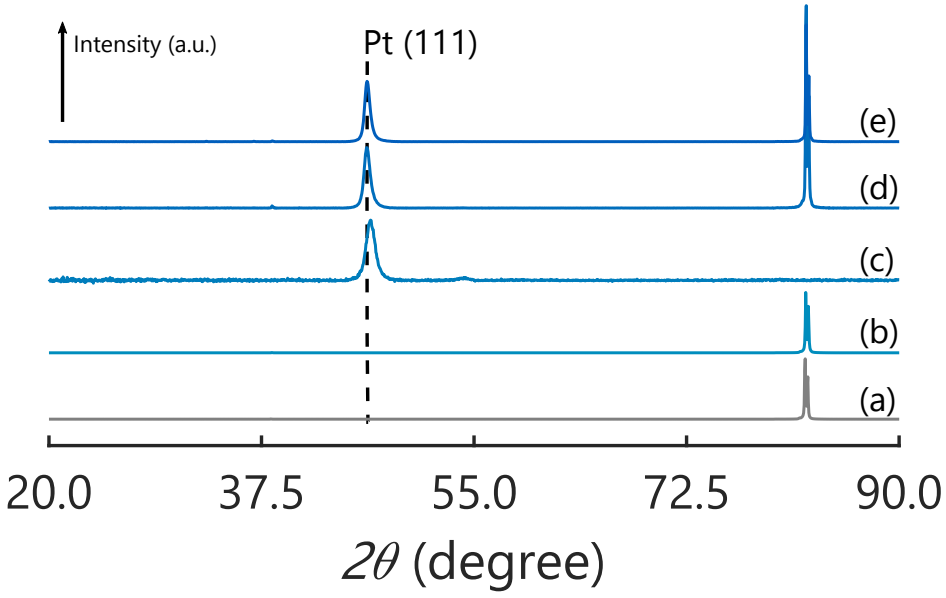


**Figure 2.5 Normalised diffractograms of Pt deposited on Si (100) by DC magnetron sputtering, where (a) is the blank substrate, (b) has a loading of 20 $\mu$g.cm$^{-2}$, (c) has a loading of 50 $\mu$g.cm$^{-2}$, (d) has a loading of 100 $\mu$g.cm$^{-2}$, and (e) has a loading of 150 $\mu$g.cm$^{-2}$**

The XRD diffraction patterns illustrated in fig. 2.5 (c)-(e) are as expected, however, the absence of the Pt (111) spectrum at approximately 46° two theta in fig. 2.5 (b) is evident. This led to the conclusion that (i) the loading on the 20 $\mu$g.cm$^{-2}$ Pt/HOPG samples is below or at the detection

limit of the instrument and there are insufficient unit cells to gain a clear diffraction pattern, or (ii) there is no Pt on these samples. In order to test this hypothesis, a range of $2\theta$ = 42 - 50° with 400 steps and a dwell time of 13.5 s per step was selected. This allowed for the Pt (111) spectra to be resolved as illustrated in fig. 2.6 below and thus proving the hypothesis that the loading was near the detection limit of the instrument. An interesting observation was the disappearance of the Si (100) spectrum at a Pt loading of 50 $\mu$g.cm$^{-2}$. This is explained by the thermodynamics of the system which are minimised such that Pt forms a continuous and homogenous film across the surface of the substrate, whereas loadings below and above 50 $\mu$g.cm$^{-2}$ form discrete particles. This hypothesis seems to be supported by the XRR measurements (fig. 2.4b), particularly at $2\theta$ > 2.5°.

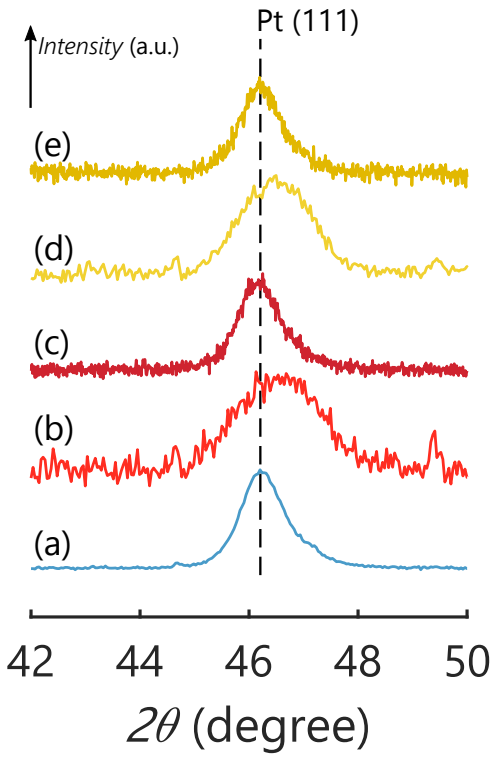


**Figure 2.6 Normalised diffractograms of (a) 50 $\mu$g.cm$^{-2}$ Pt/HOPG-P, (b) 20 $\mu$g.cm$^{-2}$ Pt/HOPG-H, (c) 50 $\mu$g.cm$^{-2}$ Pt/HOPG-H, (d) 20 $\mu$g.cm$^{-2}$ Pt/HOPG-A, and (e) 50 $\mu$g.cm$^{-2}$ Pt/HOPG-A**

From fig. 2.6, Pt crystallite sizes could be estimated using the Scherrer equation [28] below

$$d = \frac{K\lambda}{\beta cos\theta} \tag{2.3}$$

where, $d$ is the estimated crystallite size in nm, $K$ is a dimensionless shape factor set to 0.9, $\lambda$ is the X-ray source wavelength ($\lambda$ = 1.79026 Å), $\beta$ is the full width at half maximum in rad, and $\theta$ is the Bragg angle in degrees. The Pt crystallite sizes are summarised in table 2.4.

**Table 2.4 Pt crystallite sizes for Pt/HOPG as determined by the Scherrer equation**

| Sample | Pt (111) Crystallite Size (nm) |
|---|---|
| 20 $\mu$g.cm$^{-2}$ Pt/HOPG-H | 5.45 |
| 20 $\mu$g.cm$^{-2}$ Pt/HOPG-A | 6.50 |
| 50 $\mu$g.cm$^{-2}$ Pt/HOPG-P | 10.9 |
| 50 $\mu$g.cm$^{-2}$ Pt/HOPG-H | 11.1 |
| 50 $\mu$g.cm$^{-2}$ Pt/HOPG-A | 10.8 |

The above results show that with increasing loading, the Pt crystallite size reaches thermodynamic equilibrium, approaching the average crystallite diameter of Pt black. This is expected, as 50 $\mu$g.cm$^{-2}$ Pt seems to create a uniform film across HOPG and Si as discussed earlier. The estimated crystallite sizes at 20 $\mu$g.cm$^{-2}$ Pt loading deviates from this pattern, as the average crystallite size increases from HOPG-H to HOPG-A, this suggests a stronger affinity of HOPG-A to interact with Pt. While this is speculative at this point, X-ray photoelectric spectroscopy (XPS) can assist in understanding the chemical nature of the surface of the electrocatalyst.

The 20 $\mu$g.cm$^{-2}$ Pt/HOPG (fig. 2.7a - c) and 50 $\mu$g.cm$^{-2}$ Pt/HOPG (fig. 2.7d - f) C 1*s* spectra, we see very similar chemical traits as seen from XPS spectra. The C 1*s* spectra were obtained without any Ar sputtering, and hence gives a fair representation of the chemical surface as

determined electrochemically in fig. 2.3. Prior to any electrochemical activity and accelerated durability tests, we see a large response from $sp^2$ carbon moieties. It is postulated that Pt films agglomerate around the oxygen rich areas on the HOPG, thus leaving only an area of the characteristic HOPG basal plane at 284.4 eV. This is further emphasised by the low C 1*s* response in the survey scan (fig. 2.8).

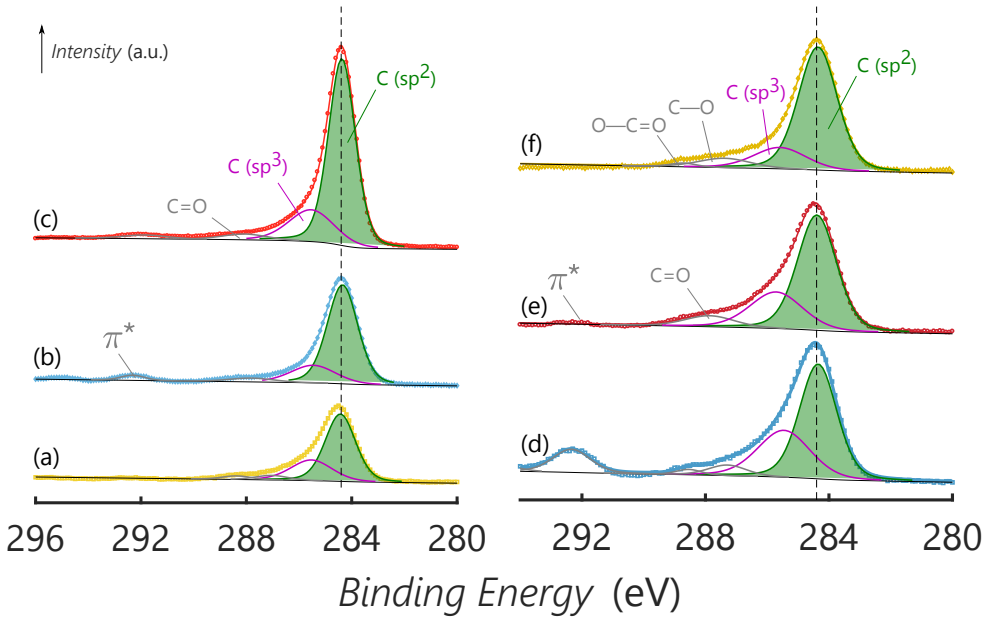


**Figure 2.7 C 1*s* spectra of (a) 20 $\mu$g.cm$^{-2}$ Pt/HOPG-A, (b) 20 $\mu$g.cm$^{-2}$ Pt/HOPG-P, (c) 20 $\mu$g.cm$^{-2}$ Pt/HOPG-H, (d) 50 $\mu$g.cm$^{-2}$ Pt/HOPG-P, (e) 50 $\mu$g.cm$^{-2}$ Pt/HOPG-H, and (f) 50 $\mu$g.cm$^{-2}$ Pt/HOPG-A**

The Pt response from the survey scan is shown in fig. 2.8, while a more focussed Pt 4*f* spectra were measured in fig. 2.9. The spectra for Pt/HOPG-P served as the baseline and Pt/HOPG-H and Pt/HOPG-A was compared to identify if any peak shifts occurred due to metal support interactions [29,30]. Although there are slight shifts to higher binding energies in the Pt 4*f* spectra for Pt/HOPG-H and Pt/HOPG-A at 0.15 - 0.20 eV, these are significant enough to account for electronic changes in the substrate [29,30]. This data is in contrast to the work reported by Matsutsu *et al.* [31] which states that electronic effects should be greater in Pt/HOPG-H, than Pt/HOPG-A. However, Pt/HOPG-A appears to have more mono-vacancy sites as seen by the large valleys in fig. 2.1.

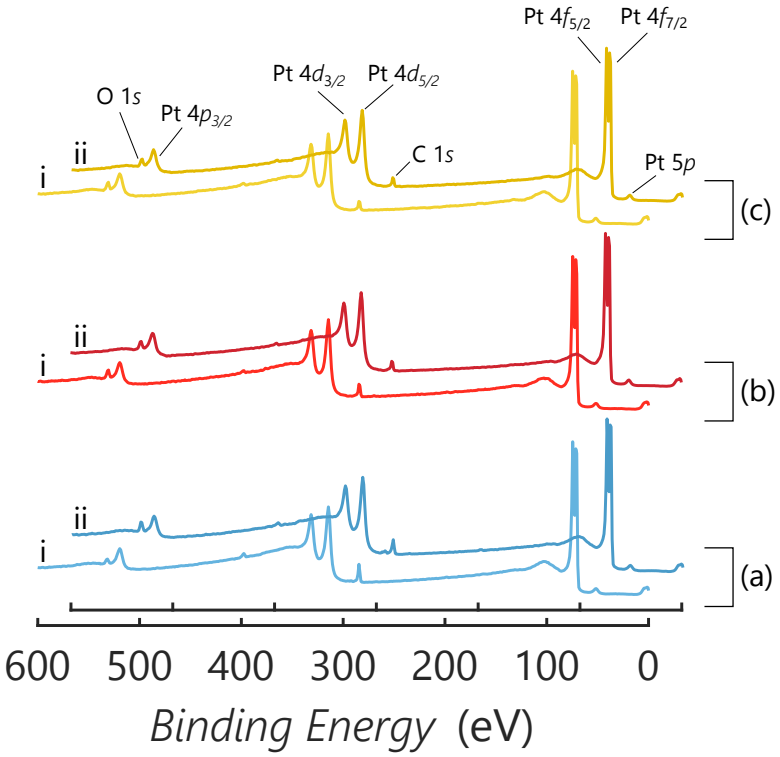


**Figure 2.8 XPS survey spectra of (a) Pt/HOPG-P, (b) Pt/HOPG-H, (c) Pt/HOPG-A, where (i) is a loading of 20 $\mu$g.cm$^{-2}$ Pt, and (ii) is a loading of 50 $\mu$g.cm$^{-2}$ Pt**

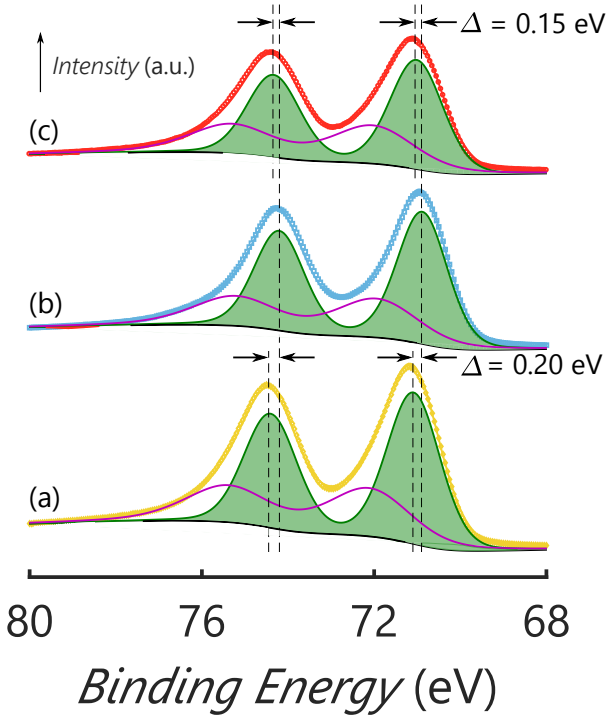


**Figure 2.9 Pt 4*f* spectra of (a) Pt/HOPG-A, (b) Pt/HOPG-P, and (c) Pt/HOPG-H, all with a loading of 20 $\mu$g.cm$^{-2}$**

Moreover, it is shown that the desired loading of Pt on the HOPG substrates was obtained. Further to this, there appears to be differences in the particle sizes and film morphology between the chemical treated samples. Due to the dominant Pt intensity in the XPS measurements, an accurate indication of the chemical nature of the surface cannot be inferred. However, the slight shifts towards higher binding energies in the Pt 4*f* spectra suggest changes in electronic structure of the substrate, which may indicate that the chemical modifications have created anchor sites for Pt.

### 2.3.3 Pt/HOPG Accelerated Durability Tests

Chemical modification of HOPG and the subsequent deposition of Pt at loadings of 20 $\mu$g.cm$^{-2}$ and 50 $\mu$g.cm$^{-2}$ on these substrates was successful. Following this, we looked at the electrochemical environment of Pt/HOPG and how mobile Pt is across the surface of the various substrates. Load cycling durability tests in a square wave form was performed in accordance with Ohma *et al.* [14] and the US DoE [2]. Together with the ADTs, the differential capacitance was measured before and after load cycling to ensure that the HOPG substrate remains unchanged over the course of the experiment. These experiments were used to investigate the electrochemical environment of the Pt/HOPG samples and the mobility of Pt on the surface of the various substrates.

**Table 2.5 Summary of Pt/HOPG ECSA at intervals during load cycling**

| Sample | Electrochemical Active Surface Area ($m^2.g_{Pt}^{-1}$) | | | | % $\Delta$ECSA |
|---|---|---|---|---|---|
| | Cycle 180 | Cycle 1190 | Cycle 3200 | Cycle 5250 | |
| 20 $\mu$g.cm$^{-2}$ Pt/HOPG-P | 5.21 | 7.06 | 7.14 | 6.12 | -13.3% |
| 20 $\mu$g.cm$^{-2}$ Pt/HOPG-H | 2.85 | 3.92 | 3.50 | 3.40 | -13.3% |
| 20 $\mu$g.cm$^{-2}$ Pt/HOPG-A | 3.22 | 4.76 | 4.90 | 4.03 | -15.3% |

The electrochemical active surface area (ECSA) is summarised in table 2.5, using the cyclic voltammograms in fig. 2.10 – 2.12. The changes in ECSA for Pt/HOPG shows that the initial ECSA after 180 cycles is lower than the final ECSA after approximately 5,000 cycles. This is due

to conditioning of the electrocatalyst, which requires further oxidation surface contaminants. For Pt/HOPG-P we see a typical current response in 0.5 M $H_2SO_4$ with well-defined $H_{upd}$ regions. For the first 3,200 cycles, there is minimal change in the current response, which suggests that the Pt NPs/film is partially embedded into the HOPG substrate after sputtering as described in Popok *et al.* [32] and Peitz [33]. This is explained by the limited mobility in Pt NPs which sit within a crater, however after 3,200 cycles, dissolution effects appear to dominate the electrochemical response and thus a decrease in ECSA is seen.

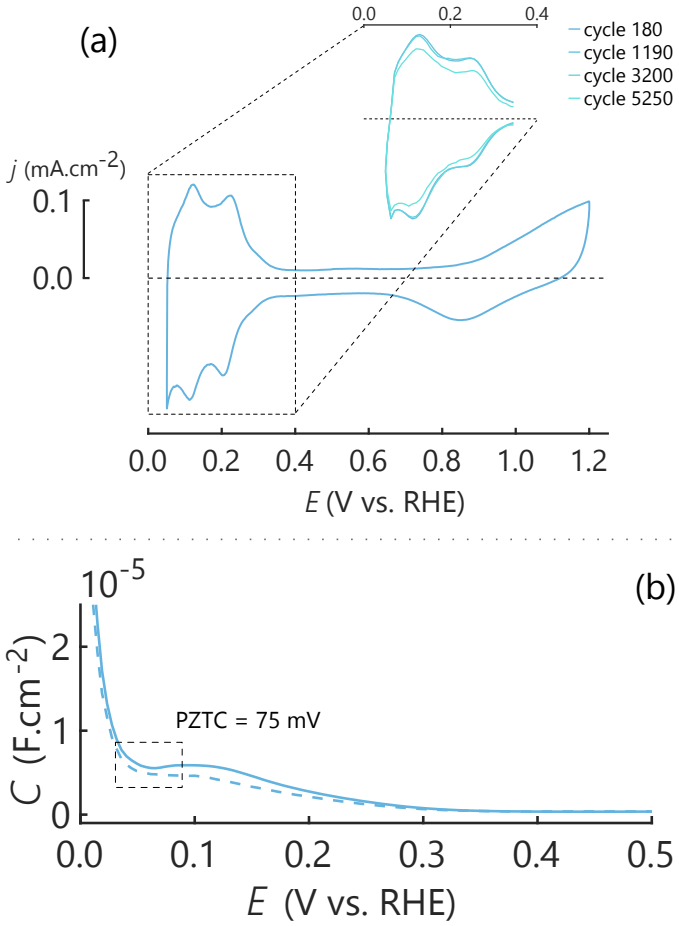


**Figure 2.10 (a) Current response of 20 $\mu$g.cm$^{-2}$ Pt/HOPG-P, inset is the hydrogen region used to determine ECSA, and (b) differential capacitance measurement in order to determine the PZTC**

The Pt/HOPG-H and Pt/HOPG-A (fig. 2.11 and fig. 2.12) both show a decrease in conductivity due to the slope of the double layer region. Typically, one would associate this slope with a

system that is not completely de-aerated, however this was excluded by measuring a $Pt_{poly}$ electrode in the same electrolyte and under the same conditions in the sequence (i) Pt/HOPG-H, (ii) $Pt_{poly}$, (iii) and Pt/HOPG-H. The slope was not present in the $Pt_{poly}$ case; hence it can be concluded that the slope is due to conductivity issues. The Pt/HOPG-H (fig. 2.11) shows a smaller ECSA than the reported ECSA values for HOPG-P and HOPG-A. While the crystallite size as determined by XRD is smaller than HOPG-A, the ECSA is influenced by the available active sites for electrochemical reactions. This suggests that portions of active metal are inaccessible and points to oxygen groups blocking these electrochemically active sites. However, there is no real evidence to suggest the validity of this hypothesis. Yet, the ECSA of Pt/HOPG-H remains statistically constant over 5,000 cycles, suggesting a stronger metal-support interaction, as Pt mobility by dissolution has been limited.

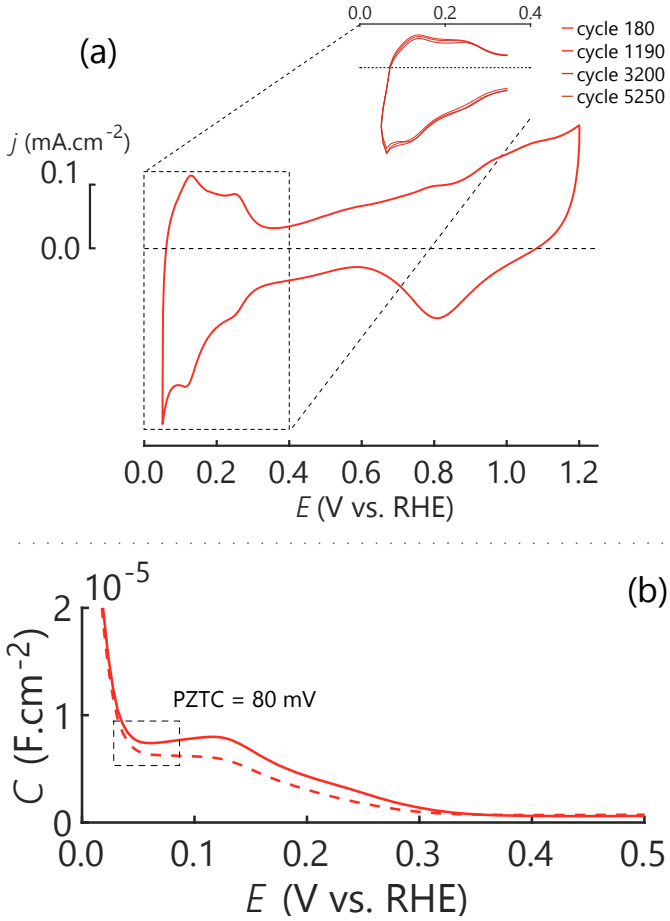


**Figure 2.11 (a) Current response of 20 $\mu$g.cm$^{-2}$ Pt/HOPG-H, inset is the hydrogen region used to determine ECSA, and (b) differential capacitance measurement in order to determine the PZTC**

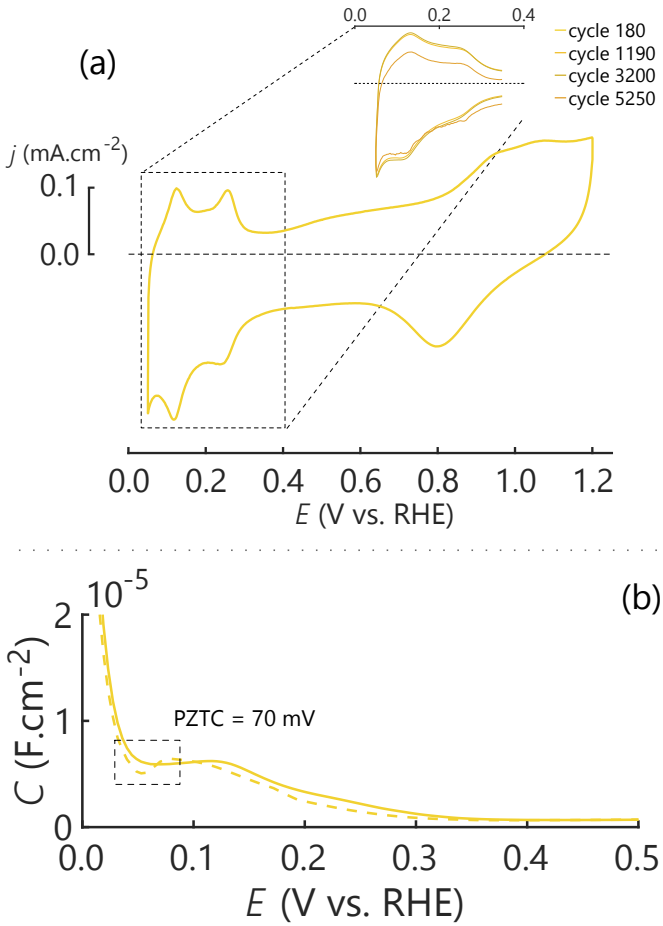


**Figure 2.12 (a) Current response of 20 $\mu$g.cm$^{-2}$ Pt/HOPG-A, inset is the hydrogen region used to determine ECSA, and (b) differential capacitance measurement in order to determine the PZTC**

A similar trend is observed for Pt/HOPG-A (fig. 2.12) as for Pt/HOPG-H. However, the change in ECSA over time is reduced significantly, which suggests that Pt has more mobility on the substrate surface (13.3% vs 15.3%). It is hypothesised from the ECSA, that Pt forms discrete islands around the oxygen terminated groups, thus leading to Ostwald ripening, and thus larger Pt particle size as illustrated in the XRD results summarised in table 2.6 below.

No significant change in the potential of zero total charge (PZTC) is observed between the substrates, as measured using differential capacitance. Using HOPG-P as the benchmark, the HOPG-H sample has a 5 mV higher PZTC and the HOPG-A sample has a 5 mV lower PZTC.

However, these slight variations in PZTC could be significant when coupled with the lower conductivity of HOPG-H and HOPG-A. Moreover, the PZTC does not change significantly after load cycling, which suggests that HOPG surface does not change, *i.e.* is not further oxidised.

Once the ADT measurements were completed, the samples were once again analysed by XRD and XPS. The diffractogram from XRD did not show any significant peak shifts, however, there is a slight narrowing of the peaks indicating particle growth. This is summarised in table 2.6 below.

**Table 2.6 Pt crystallite sizes for Pt/HOPG samples as determined by the Scherrer equation**

| Sample | $Pt_{initial}$ Crystallite Size (nm) | $Pt_{final}$ Crystallite Size (nm) |
|---|---|---|
| 20 $\mu$g.cm$^{-2}$ Pt/HOPG-P | - | 6.92 |
| 20 $\mu$g.cm$^{-2}$ Pt/HOPG-H | 5.45 | 6.97 |
| 20 $\mu$g.cm$^{-2}$ Pt/HOPG-A | 6.50 | 7.22 |
| 50 $\mu$g.cm$^{-2}$ Pt/HOPG-P | 10.9 | 11.0 |
| 50 $\mu$g.cm$^{-2}$ Pt/HOPG-H | 11.1 | - |
| 50 $\mu$g.cm$^{-2}$ Pt/HOPG-A | 10.8 | - |

As expected, growth in crystallite size after load cycling is seen, except for loadings of 50 $\mu$g.cm$^{-2}$. For 50 $\mu$g.cm$^{-2}$ loadings particle growth is not significant as the particles are at thermodynamic equilibrium. Again, it is curious that Pt/HOPG-H has a lower ECSA than Pt/HOPG-A considering that Pt/HOPG-H has the smaller average crystallite size. This seems to support the current hypothesis of some active sites being blocked by the surface oxygen groups.

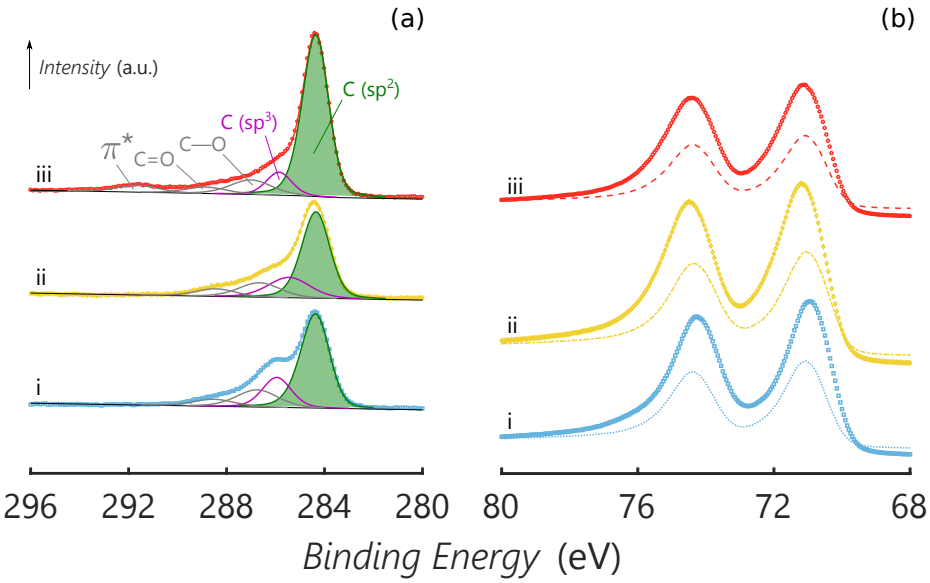


**Figure 2.13 (a) C 1*s* spectra and (b) Pt 4*f* spectra of 20 $\mu$g.cm$^{-2}$ (i) Pt/HOPG-P, (ii) Pt/HOPG-A, (iii) Pt/HOPG-H after load cycling. In (b) the dashed lines indicate the initial intensity, where the points represent the intensity after load cycling**

Lastly, XPS spectra of these samples were measured after load cycling, where significant differences in the spectra are observed. The $sp^3$ moieties are dominant, and carbonyl groups are in more abundance. This suggests that more of the carbon surface is exposed and hence, the Pt particles have agglomerated and migrated around the surface. This is further amplified by the increase in Pt 4*f* intensities after load cycling. This increase in Pt 4*f* intensity suggests that there are more well-defined Pt particles and a shift to higher binding energies for Pt/HOPG-H and Pt/HOPG-A illustrates a potential stronger support interaction [29,30], however an increase in $PtO_x$ species cannot be excluded and may be present in a greater extent in Pt/HOPG-H and Pt/HOPG-A [34-36].

## 2.4 Conclusions

From the results presented, there appears to be strong evidence of graphene-like exfoliation of HOPG under the harsh chemical treatment, by which the HOPG was modified. However, the

modifications do alter the surface carbon structure with more $sp^3$ moieties present as illustrated in the XPS results. This is further supported by the decreased conductivity observed for Pt/HOPG-H and Pt/HOPG-A.

While the results are not conclusive in illustrating which chemical modification enhances Pt interaction, there is sufficient evidence to infer that Pt will gravitate towards mono-valences or areas with defects thus supporting the theoretical work of our colleagues [31]. This is expected, as literature is inundated with reports of Pt and Au decorating HOPG steps and edges. Further to this, sputtering is too high energy for HOPG to avoid Pt implantation, even though low power and extended times were used.

However, these results indicate that Pt clusters and forms islands around oxygen terminated groups. While it is an unlikely occurrence, the determined average crystallite size indicates this phenomenon is present, especially if the changes in ECSA and absolute values of ECSA between Pt/HOPG-H and Pt/HOPG-A are considered.

An interesting aspect of these results are the changes in the PZTC of the various modified HOPG substrates. Hydroxyl groups should be weak electron donors, while acid groups are electron withdrawing. This phenomenon is evident in the shifts of the PZTC to negative for electron donating and positive for electron withdrawing relative to HOPG-P. Thus, with the absence of FT-IR, it was concluded that we have modified our surfaces with either an electron donating or electron withdrawing group.

## 2.5 References


[1] Lund, P. D., *Importance of integrated strategies and innovations for commercial breakthrough of fuel cells.* International Journal of Hydrogen Energy, 2010. **35**(7): p. 2602-2605.

[2] *Multi-year research, development and demonstration plan*. 2012, U.S. Department of Energy: Office of Energy Efficiency and Renewable Energy.

[3] Boulatov, R., *Metalloporphyrin catalysts of oxygen reduction*, in *Fuel cell catalysis: a surface science approach*, M.T.M. Koper, Editor. 2009, John Wiley & Sons. p. 637-695.

[4] Madkikar, P., Mittermeier, T., Gasteiger, H. A., and Piana, M., *Communication—Synergistic effect on the activity of $ZrO_2$-Fe as PGM-free ORR catalysts for PEMFCs*. Journal of The Electrochemical Society, 2017. **164**(7): p. F831-F833.

[5] Wu, G., *Current challenge and perspective of PGM-free cathode catalysts for PEM fuel cells*. Frontiers in Energy, 2017. **11**(3): p. 286-298.

[6] Sharma, S. and Pollet, B. G., *Support materials for PEMFC and DMFC electrocatalysts—A review*. Journal of Power Sources, 2012. **208**(Supplement C): p. 96-119.

[7] Du, L., Shao, Y., Sun, J., Yin, G., Liu, J., and Wang, Y., A*dvanced catalyst supports for PEM fuel cell cathodes*. Nano Energy, 2016. **29**(Supplement C): p. 314-322.

[8] Tauster, S. J., *Strong metal-support interactions*. Accounts of Chemical Research, 1987. **20**(11): p. 389-394.

[9] Dulub, O., Hebenstreit, W., and Diebold, U., I*maging cluster surfaces with atomic resolution: the strong metal-support interaction state of Pt supported on $TiO_2$ (110)*. Physical Review Letters, 2000. **84**(16): p. 3646.

[10] van Steen, E., Claeys, M., Dry, M. E., van de Loosdrecht, J., Viljoen, E. L., and Visagie, J. L., *Stability of nanocrystals: Thermodynamic analysis of oxidation and re-reduction of cobalt in water/hydrogen mixtures*. The Journal of Physical Chemistry B, 2005. **109**(8): p. 3575-3577.

[11] Kim, U. J., Furtado, C. A., Liu, X., Chen, G., and Eklund, P. C., *Raman and IR spectroscopy of chemically processed single-walled carbon nanotubes*. Journal of the American Chemical Society, 2005. **127**(44): p. 15437-15445.

[12] Schönfelder, R., Avilés, F., Knupfer, M., Azamar-Barrios, J. A., González-Chi, P. I., and Rümmeli, M. H., *Influence of architecture on the Raman spectra of acid-treated carbon nanostructures*. Journal of Experimental Nanoscience, 2014. **9**(9): p. 931-941.

[13] Falch, A., Lates, V., and Kriek, R. J., *Combinatorial plasma sputtering of $Pt_xPd_y$ thin film electrocatalysts for aqueous $SO_2$ electro-oxidation*. Electrocatalysis, 2015. **6**(3): p. 322-330.

[14] Ohma, A., Shinohara, K., Iiyama, A., Yoshida, T., and Daimaru, A., *Membrane and catalyst performance targets for automotive fuel cells by FCCJ membrane, catalyst, MEA WG*. ECS Trans., 2011. **41**(1): p. 775-784.

[15] Shao, L.-H., Biener, J., Kramer, D., Viswanath, R. N., Baumann, T. F., Hamza, A. V., and Weissmuller, J., *Electrocapillary maximum and potential of zero charge of carbon aerogel*. Physical Chemistry Chemical Physics, 2010. **12**(27): p. 7580-7587.

[16] Lockett, V., Sedev, R., Ralston, J., Horne, M., and Rodopoulos, T., *Differential capacitance of the electrical double layer in imidazolium-based ionic liquids: Influence of potential, cation size, and temperature*. The Journal of Physical Chemistry C, 2008. **112**(19): p. 7486-7495.

[17] Levenberg, K., *A method for the solution of certain non-linear problems in least squares*. Quarterly of Applied Mathematics, 1944. **2**(2): p. 164-168.

[18] Marquardt, D. W., *An algorithm for least-squares estimation of nonlinear parameters*. Journal of the Society for Industrial and Applied Mathematics, 1963. **11**(2): p. 431-441.

[19] Evans, S. and Thomas, J. M., *The chemical nature of ion-bombarded carbon: A photoelectron spectroscopic study of "cleaned" surfaces of diamond and graphite*. Proceedings of the Royal Society of London. A. Mathematical and Physical Sciences, 1977. **353**(1672): p. 103-120.

[20] Bard, A. J. and Faulkner, L. R., *Electrochemical methods: Fundamentals and applications*. 2nd ed. 2001: John Wiley & Sons, Inc.

[21] Nicholson, R. S., *Theory and application of cyclic voltammetry for measurement of electrode reaction kinetics*. Analytical Chemistry, 1965. **37**(11): p. 1351-1355.

[22] Cline, K. K., McDermott, M. T., and McCreery, R. L., *Anomalously slow electron transfer at ordered graphite electrodes: Influence of electronic factors and reactive sites*. Journal of Physical Chemistry, 1994. **98**(20): p. 5314-5319.

[23] McCreery, R. L., Cline, K. K., McDermott, C. A., and McDermott, M. T., *Control of reactivity at carbon electrode surfaces*. Colloids and Surfaces A, 1994. **93**(0): p. 211-219.

[24] Kinoshita, K., *Carbon: Electrochemical and physicochemical properties*. A Wiley-Interscience publication. 1988: Wiley.

[25] Kinoshita, K. and Bett, J. A. S., *Potentiodynamic analysis of surface oxides on carbon blacks*. Carbon, 1973. **11**(4): p. 403-411.

[26] Parratt, L. G., *Surface studies of solids by total reflection of X-Rays*. Physical Review, 1954. **95**(2): p. 359-369.

[27] Kiessig, H., *Untersuchungen zur Totalreflexion von Röntgenstrahlen*. Annalen der Physik, 1931. **402**(6): p. 715-768.

[28] Scherrer, P., *Bestimmung der größe und der inneren Struktur von Kolloidteilchen mittels Röntgenstrahlen*. Nachr. Ges. Wiss. Gottingen, Math. Phys., 1918. **2**(July): p. 98-100.

[29] Ma, J., Habrioux, A., Morais, C., Lewera, A., Vogel, W., Verde-Gómez, Y., Ramos-Sanchez, G., Balbuena, P. B., and Alonso-Vante, N., *Spectroelectrochemical probing of the strong interaction between platinum nanoparticles and graphitic domains of carbon*. ACS Catalysis, 2013. **3**(9): p. 1940-1950.

[30] Jackson, C., Smith, G. T., Inwood, D. W., Leach, A. S., Whalley, P. S., Callisti, M., Polcar, T., Russell, A. E., Levecque, P., and Kramer, D., *Electronic metal-support interaction enhanced oxygen reduction activity and stability of boron carbide supported platinum*. Nature Communications, 2017. **8**: p. 15802.

[31] Matsutsu, M., Petersen, M. A., and van Steen, E., *$Pt_{38}$ cluster on OH- and COOH-functionalised graphene as a model for Pt/C-catalysts*. Phys Chem Chem Phys, 2016. **18**(36): p. 25693-25704.

[32] Popok, V. N., Barke, I., Campbell, E. E. B., and Meiwes-Broer, K.-H., *Cluster–surface interaction: From soft landing to implantation*. Surface Science Reports, 2011. **66**(10): p. 347-377.

[33] Peitz, A., *Degradation mechanisms of electrocatalysts used in polymer electrolyte fuel cells*, in *Department of Chemistry and Applied Biosciences*. 2011, ETH Zurich: ETH Zurich.

[34] Ago, H., Kugler, T., Cacialli, F., Salaneck, W. R., Shaffer, M. S. P., Windle, A. H., and Friend, R. H., *Work functions and surface functional groups of multiwall carbon nanotubes*. J Phys Chem B, 1999. **103**(38): p. 8116-8121.

[35] Brieger, C., Melke, J., van der Bosch, N., Reinholz, U., Riesemeier, H., Guilherme Buzanich, A., Kayarkatte, M. K., Derr, I., Schökel, A., and Roth, C., *A combined in-situ XAS–DRIFTS study unraveling adsorbate induced changes on the Pt nanoparticle structure*. Journal of Catalysis, 2016. **339**: p. 57-67.

[36] Xing, L., Hossain, M. A., Tian, M., Beauchemin, D., Adjemian, K. T., and Jerkiewicz, G., *Platinum electro-dissolution in acidic media upon potential cycling*. Electrocatalysis, 2014. **5**(1): p. 96-112.

# Chapter 3
# Towards Practical Applications of EQCN Experiments to Study Pt Anchor Sites on Carbon Surfaces: Part 1 – Validation of Technique

**Modified from Fortuin et al. [1] for this report*

## 3.1 Introduction

Electrochemical quartz crystal nano-balance (EQCN) is a powerful tool to study interfacial electrochemistry phenomena [2,3]. This technique allows for conventional electrochemical techniques, such as cyclic voltammetry (CV), chronoamperometry (CA), and other potential sweep methods to be used in parallel with the detection of nanogram mass changes [4-6]. This leads to detailed studies of electrochemical surface reaction mechanisms, deposition rates, and roughness effects [6-9]. The technique has been shown to be particularly useful in sensor applications, as its sensitivity allows for small mass/concentration changes in a system to be easily detected [10-12].

Much of the research in the electrocatalysis field has not been able to make use of this powerful tool as real-world catalysts cannot easily be applied to a quartz crystal resonator essential for EQCN experiments. Fundamental research, such as the work conducted by Jerkiewicz *et al.* [13-15], has focused on using the EQCN technique to model a carbon supported platinum (Pt/C) electrocatalyst as a bulk $Pt_{poly}$ catalyst. While this gives critical insights into the surface reaction mechanisms on Pt, it excludes the metal-support interactions between Pt and carbon. However, little work has been published with regards to modifying a quartz crystal resonator for more applied investigations into the interfacial electrochemistry occurring on supported platinum nanoparticles and the electronic interaction between Pt and carbon in a Pt/C electrocatalyst.

Some attempts have been made at depositing a Pt/C ink onto a gold coated quartz crystal [16,17]. However, these systems are difficult to calibrate since precise loadings are required to

ensure that the quartz crystal oscillations are not drastically different from measurement to measurement.

Before directly studying Pt anchor sites on carbon by EQCN, it needs to be shown that the two different 2-D model Pt/C catalyst systems can be directly compared, such that the stability (and hence anchoring) of Pt on the support can be investigated by EQCN. The model system of the real-world catalyst (*e.g.* Pt supported on Vulcan) is represented by Pt sputtered onto basal plane oxygen terminated highly orientated pyrolytic graphite (HOPG). The system of comparison is a mirror finished graphite (MFG) quartz crystal resonator, onto which Pt has been sputtered. The MFG undergoes the exact same surface oxidation treatment as the HOPG, such that the two catalysts can be directly compared. The aim is to obtain similar electrochemical responses on the MFG as HOPG, using conventional electrochemical methods, such that we can study Pt/C using EQCN. This chapter reports the physical characteristics of the two systems, namely the crystallite size, crystallography, surface functional groups, as well as electrochemical responses via cyclic voltammetry in acidic media and the ferri/ferrocyanide couple [18,19].

## 3.2 Experimental Methods

All electrochemical measurements were conducted using a Bio-Logic SP-200 potentiostat. EQCN measurements were conducted using a Seiko EG&G QCM922A, in a home-built Faraday cage and vibration free table. The packaged EC-Lab v11.1x software was used to control both instruments.

### 3.2.1 Electrodes

A custom-built, two-compartment cell (developed by Prof Jerkiewicz) was used and cleaned by submerging in NOCHROMIX® (Godax Laboratories, Inc.) overnight. A Teflon™ quartz holder houses the planar quartz crystals cut in the AT orientation, in the vertical cell orientation as

described by Jerkiewicz *et al.* [20]. An AT-cut quartz crystal was coated with a 100 nm Ti layer, followed by sputtering of approximately 300 nm Pt layer to form a Pt coated quartz crystal (PQC). Alternatively, a 300 nm carbon layer was sputtered onto the 100 nm Ti layer on the quartz to fabricate a MFG quartz crystal with a roughness of 60 nm. The base resonant frequency was 9.00 MHz and 9.13 MHz for PQC and MFG respectively. All quartz crystals were supplied by Bio-Logic.

The working electrode for the conventional system consisted of 1 $cm^2$, 200 $\mu$m thick HOPG disks (Optigraph GmbH, Berlin). This was attached to a conventional glassy carbon (GC) electrode using a carbon-Nafion® (Ion Power) paste. The HOPG surface was modified by refluxing in Fenton's reagent for 24 hours at 80 °C [21] , the constant time and temperatures were chosen to ensure the concentration of potential anchor sites on the surface is maximised.. The hydroxyl modified HOPG is referred to as HOPG-H, with the pristine HOPG samples referred to as HOPG-P. Pt was then deposited onto the modified and unmodified surfaces at a loading of 20 $\mu g.cm^{-2}$ by DC magnetron sputtering (PVD Products, USA). This was accomplished by using a Pt sputtering target (1.5" diameter x ⅛" thick) obtained from ACI Alloys (USA) having a purity of 99.95%. Prior to sputtering, the vacuum chamber of the sputtering apparatus was pumped down to a base pressure of approximately $5 \times 10^{-7}$ Torr. Sputtering of Pt, under an Ar plasma, was conducted at a chamber pressure of 8 mTorr and an Ar flow of 15 sccm. The sputtering rate ($nm.min^{-1}$) of Pt was calibrated as described by Falch *et al.* [22] with minimal deviation in the sputtered layer from sample to sample. The substrates were positioned onto a stainless-steel tray that slots into a housing fitted with a computer controlled XY motor below a fixed aperture, allowing for dedicated sputtering of individual samples. Similarly, the aforementioned procedure was used to prepare surface modified MFG and deposit Pt. The hydroxyl modified MFG is referred to as MFG-H and the unmodified MFG is referred to as MFG-P. In this instance, a dedicated stainless-steel tray was manufactured in-house to deposit Pt on the MFG samples in an evenly spaced manner within the sputtering apparatus as seen in fig. 3.1.

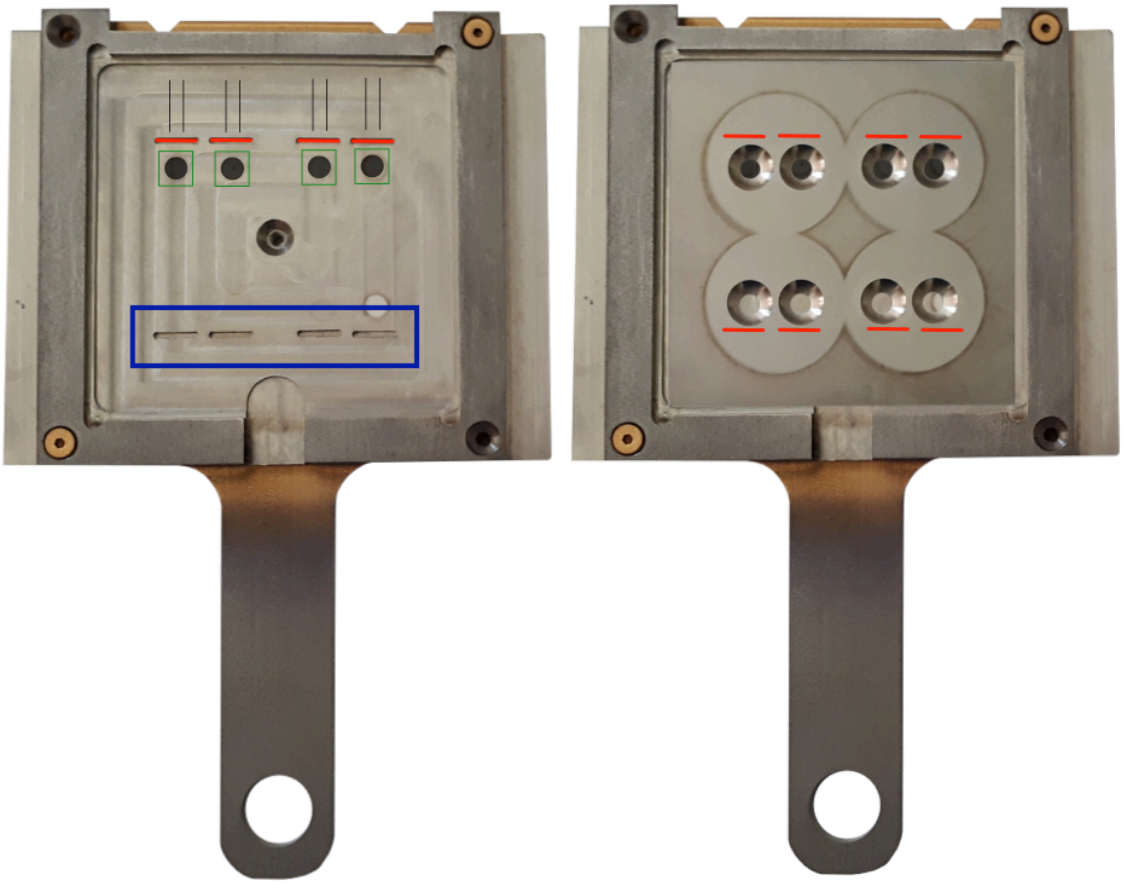

**Figure 3.1 In-house manufactured stainless-steel tray for sputtering on quartz crystal samples with the lead wire attached. The left tray is with the aperture mask removed, with schematic of the quartz crystal resonators positioned with the mantle in the grooves. The right tray is with the aperture mask placed on top of the quartz crystal resonators, the red lines indicate the mantle grooves.**

A reversible hydrogen electrode (RHE) using Pt foil (Alfa Aesar, 99.999%) was used as the reference electrode and a Pt mesh (Alfa Aesar, 99.99%) as the counter electrode.

### 3.2.2 Electrochemical Testing

Prior to conducting electrochemical measurements on HOPG and MFG, cyclic voltammograms ($i$ vs $E$) of $Pt_{poly}$ were measured in aqueous 0.5 M $H_2SO_4$ prepared from 99.999 wt.% $H_2SO_4$ (Sigma Aldrich) and 18.2 MΩ.cm nano-pure water. All measurements were carried out at room temperature and under an inert Ar atmosphere (99.999%, Air Products). The electric potential

was cycled between 0.05 and 1.50 V vs RHE to ensure cleanliness and reproducible functioning of the electrochemical setup.

To confirm the oxidation of HOPG by various treatment methods and changes in the electronic states of the carbon, CVs using the ferri/ferrocyanide redox couple were run. A solution of 1 mM $K_4Fe(CN)_6$ (Sigma Aldrich) in 1 M $KCl_{(aq)}$ (Merck) was prepared. The electric potential was cycled between 0.00 and 1.20 V vs RHE at scan rates of 100, 75, 50, 25, and 20 $mV.s^{-1}$, of which we only report on the scan rate at 50 $mV.s^{-1}$here. See fig. A.1 and A.2 for current responses for all scan rates and summaries of $\Delta E_p$ and peak current density ($j_p$) as a function of scan rates in Appendix A. Similarly, this was applied to the MFG system and the two systems were compared.

### 3.2.3 Physical Characterisation

X-ray diffraction (XRD) measurements were taken using a Bruker D2 Phaser in the Bragg-Brentano geometry with a Co anode ($\lambda$ = 1.79026 Å), primarily using a $2\theta$ range of 20 - 90° with 0.0274° steps. Samples were placed in a zero-background sample holder and was placed such that they were in line with a straight edge across the holder. The measurement was repeated at various angles ($\Phi$) about the vector normal to the sample surface.

X-ray photoelectron spectroscopy (XPS) measurements were carried out using a monochromated Al source (1487.1 eV) and a SPECS PHOIBOS 150 hemispherical electron energy analyser. The overall experimental resolution was approximately 0.6 eV for all spectra. Some of the spectra were acquired on a KRATOS-SUPRA spectrometer at UNISA (Florida Science Campus, South Africa), using a monchromated Al source (1486.6 eV) having a base pressure of $1.2 \times 10^{-8}$ Torr. The surface of all samples was cleaned with a short cycle of Ar ion sputtering. This ranged from 30 to 120 s, with measurements taken at various intervals.

## 3.3 Results and Discussion

### 3.3.1 Physical Characterisation

XRD measurements showed reproducible diffraction peaks across the lateral position of the various carbon substrates. The diffraction patterns were independent of the orientation about $\Phi$, by considering the reproducibility of the peak shape and intensities (*e.g.* HOPG-H (d) – (f) peaks in fig. 3.2), which shows that the scattering vector was normal to the surface (fig. 3.2).

Furthermore, the MFG graphitic peaks around 31° $2\theta$ are shifted to a larger angle compared to the HOPG samples, suggesting a slightly smaller d-spacing. This was accompanied by narrower peak widths relating to a larger crystallite size. Relative crystallite sizes were estimated using the Scherrer equation [23] below,

$$d = \frac{K\lambda}{\beta cos\theta} \qquad (4.1)$$

where, $d$ is the estimated crystallite size in nm, $K$ is a dimensionless shape factor set to 0.9, $\lambda$ is the X-ray source wavelength ($\lambda$ = 1.79026 Å), $\beta$ is the full width at half maximum in rad, and $\theta$ is the Bragg angle in deg, and are summarised in table 3.1.

Absent peaks in the MFG samples suggest a preferred orientation, while this does not appear the case for the HOPG samples with which they were compared.

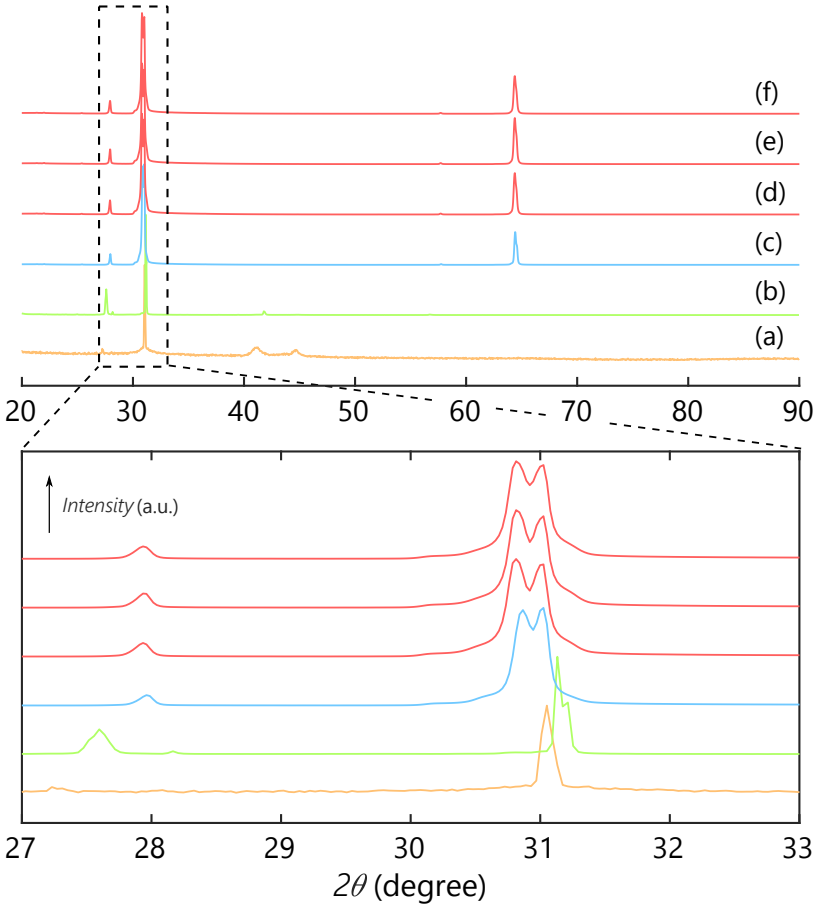


**Figure 3.2 Diffractograms comparing the various carbon substrates where (a) MFG-P, (b) MFG-H, (c) HOPG-P, and (d) – (f) HOPG-H at different angles of $\Phi$. The magnified portion focuses on the graphite (002) orientation, showing a shift to lower d-spacing for the MFG substrates**

**Table 3.1 Comparison of graphite crystallite size and Pt crystallite size as determined by the Scherrer equation [23] of HOPG and MFG substrates at loadings of 50 $\mu$g.cm$^{-2}$ Pt**

| Sample | C (002) Crystallite Size (nm) | Pt (111) Crystallite Size (nm) |
|---|---|---|
| HOPG-P | 26.1 | - |
| MFG-P | 63.0 | - |
| 50 $\mu$g.cm$^{-2}$ Pt/HOPG-P | 23.0 | 10.8 |
| 50 $\mu$g.cm$^{-2}$ Pt/HOPG-H | 26.7 | 10.1 |
| 50 $\mu$g.cm$^{-2}$ Pt/MFG-P | 71.3 | 14.9 |
| 50 $\mu$g.cm$^{-2}$ Pt/MFG-H | 85.9 | 12.1 |

XPS measurements confirm the results seen in XRD, with a sharp C 1*s* peak observed in the survey spectra (fig. 3.3). There was minimal nitrogen and oxygen present in the samples, with only an appreciable contaminant present in the MFG-P spectrum. This small Ar 2*p* peak at approximately 241.1 eV is due to Ar implantation in the graphite matrix during sputtering [24].

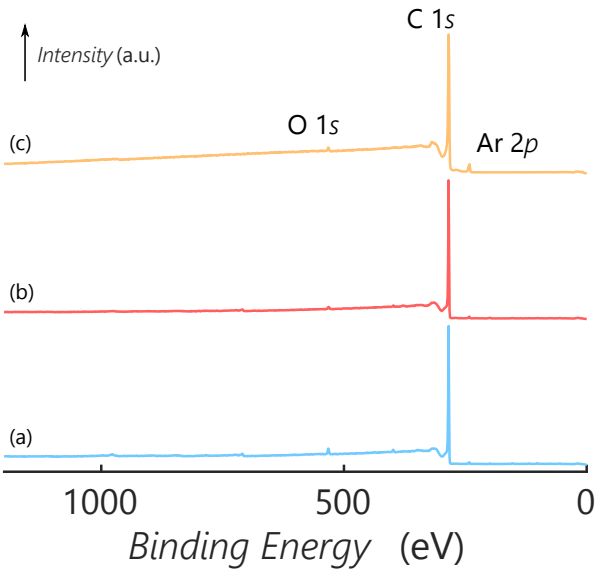


**Figure 3.3 XPS survey spectra of (a) HOPG-P, (b) HOPG-H, and (c) MFG-P. Bands at (iv) 532.4 eV, (iii) 398.5 eV, (ii) 284.4 eV, and (i) 241.1 eV are assigned to O 1*s*, C 1*s*, and Ar 2*p* respectively**

Based on the valence band data displayed in fig. 3.4, all samples have similar densities of state (DOS) near the Fermi level ($E_F$) as indicated by the overlay of the spectra in the inset. However, MFG-P does have a more pronounced O 2*s* band at 21.9 eV, suggesting that this graphite moiety is covered with larger amounts of surface carbonyl groups as stated in other studies [25-27]. This observation is further supported by the broadening of MFG-P's C 1*s* spectrum towards higher binding energies shown in fig. 3.5.

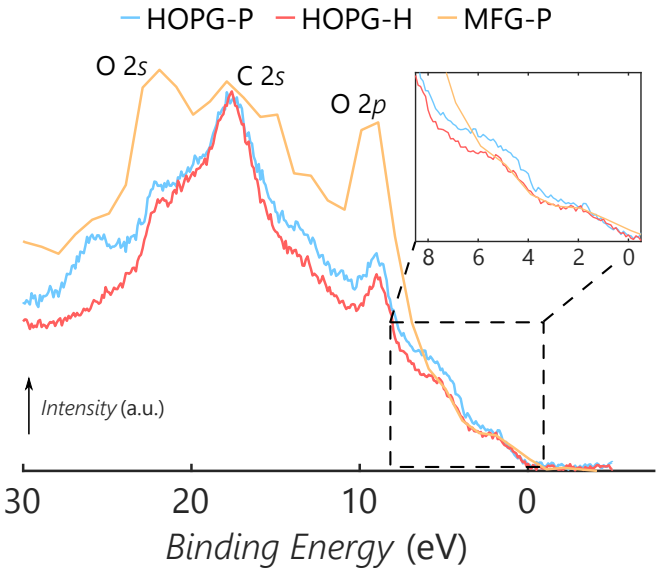


**Figure 3.4 Valence band spectra of HOPG-P, HOPG-H and MFG-P respectively. Bands at 22.2 – 21.9 eV, 17.9 – 17.6 eV, and 9.0 – 8.9 eV are assigned to O 2*s*, C 2*s*, and O 2*p* respectively. The inset shows a magnification of the densities of state closer to the Fermi level in UHV**

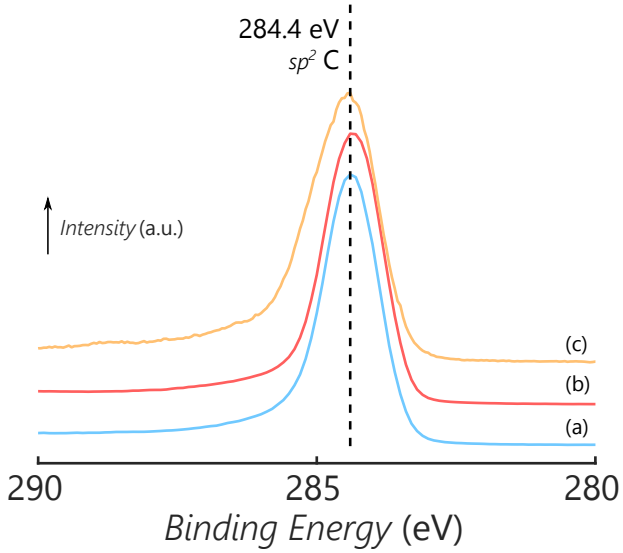


**Figure 3.5 C 1*s* spectra of (a) HOPG-P, (b) HOPG-H, and (c) MFG-P. All spectra are calibrated to 284.4 eV as the C $sp^2$ band**

### 3.3.2 Electrochemical Results

#### *3.3.2.1 $[Fe(CN)_6]^{4-/3-}$ Redox Couple for Carbon Substrates*

The CVs of the ferri/ferrocyanide redox couple were studied for different graphite substrates, shown in fig. 3.6. Control substrates of GC, HOPG-P, and MFG-P were studied to create a baseline to which surface modifications and Pt depositions can be compared. From the corresponding CVs, an estimated electrode capacitance (*C*) [28] was determined, as well as the rate constant, $k^0$, using Nicholson's method [29][1].

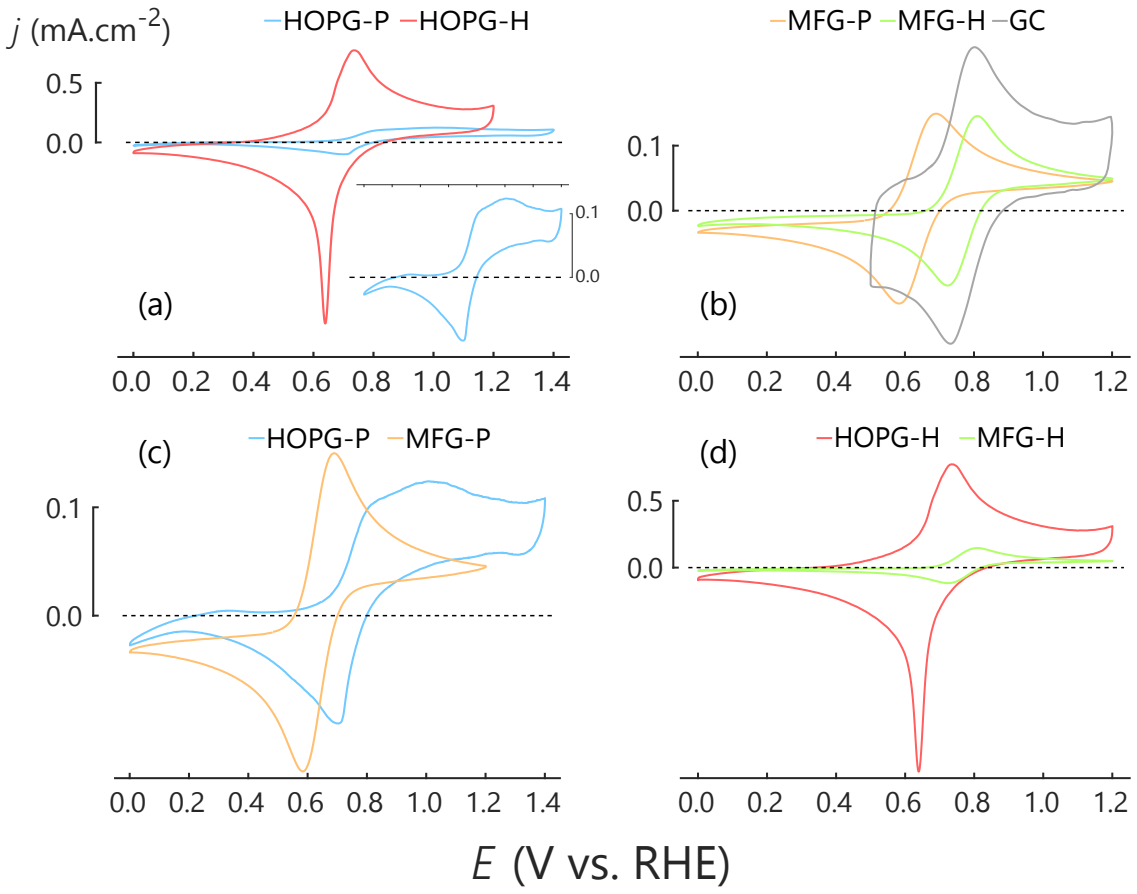


**Figure 3.6 Current responses of (a) HOPG-P and HOPG-H, (b) MFG-P, MFG-H, and GC, (c) HOPG-P and MFG-P, and (d) HOPG-H and MFG-H in 1 mM $[Fe(CN)_6]^{4-}$ / 1 M $KCl_{(aq)}$ solution under Ar saturation and room temperature, with a sweep rate of 50 mV.s$^{-1}$**

[1] See section 2.3.1, pages 34 and 35, for explanation of calculations

Unmodified, pristine HOPG surfaces show slow rates of electron transfer for the $[Fe(CN)_6]^{4-/3-}$ couple. This has been postulated by Cline *et al.* [18] to be due to a lack of surface reactive sites as the basal plane of HOPG, which is not a suitable electron transfer structure, hence the surface morphology has a significant influence on $k^0$. With the introduction of surface disorder, *i.e.* by surface treatment/oxidation, there is a significant increase in the rate constant as indicated in table 3.2 [18,19]. Furthermore, as seen in fig. 3.6 (a), the broadening of the HOPG-P peaks ($E_{p,a}$ and $E_{p,c}$) and deviation from the classic "duck bill" shape, suggests that there are few sites for adsorption for the ferrocyanide ion and subsequent electron transfer.

**Table 3.2 Redox potential, kinetic data, and capacitance values for various carbon substrates with loadings of 20 $\mu$g.cm$^{-2}$ Pt and without Pt**

| Substrate | $\Delta E_p$ (mV) | $k^0$ (cm.s$^{-1}$)[a] | C ($\mu$F.cm$^{-2}$) |
|---|---|---|---|
| HOPG-P | 306 | $5.0 \times 10^{-7}$ | 620 |
| HOPG-H | 95.2 | 0.0056 | 3,400 |
| 20 $\mu$g.cm$^{-2}$ Pt/HOPG-P | 65.0 | 0.035 | 1,300 |
| 20 $\mu$g.cm$^{-2}$ Pt/HOPG-H | 75.0 | 0.014 | 2,300 |
| MFG-P | 107 | 0.0033 | 490 |
| MFG-H | 85.9 | 0.0085 | 290 |
| 20 $\mu$g.cm$^{-2}$ Pt/MFG-P | 87.4 | 0.0080 | 1,400 |
| 20 $\mu$g.cm$^{-2}$ Pt/MFG-H | 185 | $1.1 \times 10^{-4}$ | 1,500 |
| GC | 68.7 | 0.020 | 520 |

[a] $\alpha = 0.5$, $D_O = D_R = 10^{-5}$ cm$^2$.s$^{-1}$

The HOPG-H substrate shows a five-fold increase in capacitance over HOPG-P (fig. 3.6a). This is a similar capacitance value observed as for GC. This increase is most likely due to decreased conductivity of HOPG-H. However, since the resolution of the Al X-ray source is too low to see such small changes in the near-$E_F$ electronic structure, it is speculated that the process of oxidizing HOPG, exfoliates a few layers of graphite from the surface whilst the hydroxyl radicals bond to the surface. The fact that HOPG-P and HOPG-H show very similar XPS spectra after Ar ion sputtering, is evidence that only the very top few atomic layers of HOPG participate in oxidation.

Contrary to HOPG, as shown in fig. 3.6 (b) and (d), the large increase in capacitance is not seen for the MFG-H samples as seen between HOPG-P and HOPG-H. Although not well understood, it is postulated that the surface orientation of the graphite is slightly different from HOPG, as seen in XRD, and thus less hydroxyl radicals react with the surface. What is clear, though, is that HOPG-H and MFG-H show increased electron transfer rates over their HOPG-P and MFG-P counterparts.

*3.3.2.2 Electrochemical Response of Pt Supported Carbon Substrates*

A loading of 20 $\mu$g.cm$^{-2}$ Pt was deposited onto the various carbon substrates as described in section 3.2.1. CVs in an acidic medium were recorded for characteristic Pt electrochemical response and CVs in ferri/ferrocyanide were recorded and compared as in section 3.3.2.1.

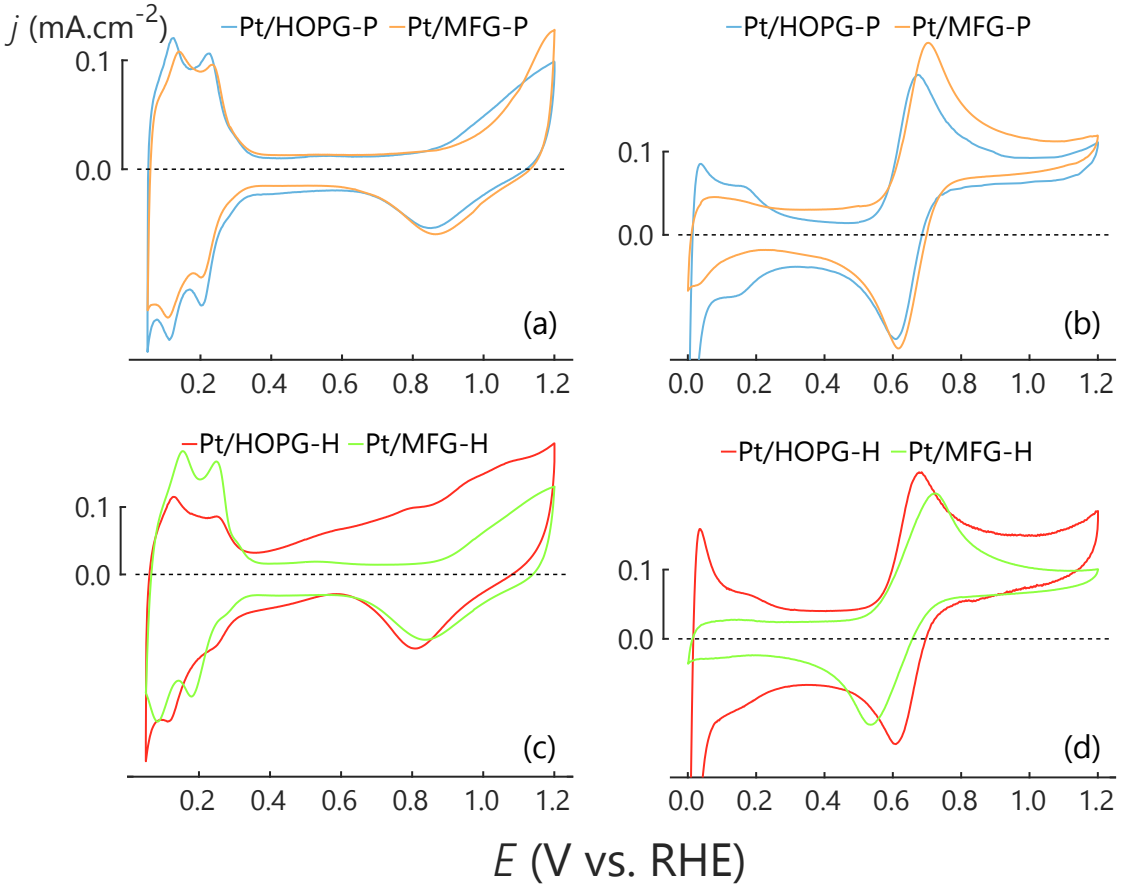


**Figure 3.7 Comparative current responses of 20 $\mu$g.cm$^{-2}$ Pt on HOPG-P, MFG-P, HOPG-H, and MFG-H in (a),(c) 0.5 M $H_2SO_4$ and (b),(d) 1 mM $[Fe(CN)_6]^{4-}$ / 1 M $KCl_{(aq)}$ solution under Ar saturation and room temperature, with a sweep rate of 50 mV.s$^{-1}$**

As expected with the deposition of Pt, the capacitance of the samples decreases. From fig. 3.7 (a) HOPG-P20 and MFG-P20 (20 $\mu$g.cm$^{-2}$ Pt deposited) the Pt CVs indicate similar responses, with the only appreciable difference in the oxide formation region. The onset of oxide formation is shifted to higher potentials in MFG-P20, indicating that this graphite moiety may have larger Pt nanoparticles deposited and is more oxophilic [30]. However, fig. 3.7 (b) suggests that the Pt layer may be shielded (*i.e.* implanted in the graphite matrix), as there is larger current contribution from graphite in the $[Fe(CN)_6]^{4-/3-}$ redox couple. The greater surface roughness of MFG as compared to HOPG, supports the above hypothesis, as well as supporting the reasoning that inner sphere electron transfer is taking place, as opposed to outer sphere electron transfer. The ill-defined Pt-$H_{upd}$ (0.0 – 0.4 V vs. RHE) region and larger $\Delta E_p$ table 3.2 is a clear indicator that Pt plays less of a role in electron transfer than what is suggested by the current response in acid. Similarly, for the peroxide treated equivalent samples (fig. 3.7c & d) the above trend is observed. Furthermore, the tilting of HOPG-H20's current response in acid (fig. 3.7c) is indicative of decreased conductivity within the support.

*3.3.2.3 Frequency Response of Pt Supported on Carbon Substrates*

While the above has shown that Pt/MFG has a typical current response for Pt in acid media, its frequency response needs to be compared to a baseline of $Pt_{poly}$ coated quartz crystal. The frequency response curve of $Pt_{poly}$ has been well documented by Jerkiewicz *et al.* [5,9,13-15,20,31-33] over the years, and an accurate reproduction of the standard Pt frequency response serves as the basis of validating the EQCN setup.

From fig. 3.8, a frequency response for $Pt_{poly}$ over a range of 0.0 – 1.5 V vs RHE shows a frequency change of approximately 25 Hz, which is in good accordance to that reported by Jerkiewicz [14] and Kim *et al.* [9,32-34].

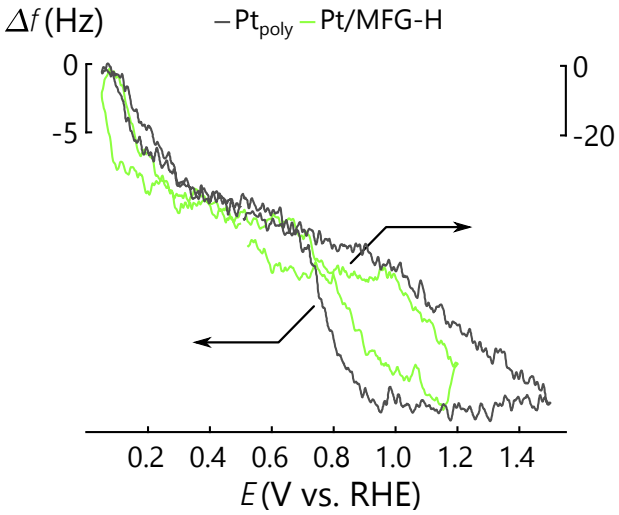


**Figure 3.8 Comparative frequency response of Ptpoly quartz crystal and 20 $\mu$g.cm$^{-2}$ Pt/MFG-H quartz crystal in 0.5 M $H_2SO_4$ under Ar saturation and room temperature, with a sweep rate of 50 mV.s$^{-1}$**

Measuring the frequency response of MFG-H20 against $Pt_{poly}$, a clear similarity between the two catalysts can be seen, but a larger $\Delta f$ response versus potential in the graphite substrate is observed. This is to be expected, as the surface of MFG-H20 has a significantly larger capacitance than Pt, hence a larger effect of ion attraction and repulsion from the surface influencing the response as discussed by Jerkiewicz [14]. This is further substantiated by the wider hysteresis in the Pt-$H_{upd}$ region of the Pt/MFG-H, showing a reliable depiction of the electrochemical surface phenomena on Pt. Thus, we have shown that we can reliably study Pt/MFG-H by EQCN.

## 3.4 Conclusions

From these preliminary results, it is shown that the behavior of the carbon substrates is in good agreement with each other based on XRD diffraction patterns and XPS valence band structure data. The electrochemical surface response is different and was attributed to the orientation of the graphite crystal facets, as the ferri/ferrocyanide redox couple is very surface sensitive.

However, the electrochemical response of the ferri/ferrocyanide couple was in good agreement with the larger graphite crystallite size recorded by XRD. Furthermore, the $k^0$ and capacitance of the MFG, catalysed and uncatalysed, increases after surface modification. This is in accordance with the trend seen between modified and unmodified HOPG, and thus serves as a basis of comparison. Based on these findings, HOPG and MFG samples are structurally comparable, and their electrochemical behaviour, while not identical, follow similar trends after modification.

In the case of Pt/MFG, the electrochemical surface response is less comparable to Pt/HOPG when probing with the ferri/ferrocyanide redox couple but is similar in acidic media. It is postulated that the marginal physical surface differences in the MFG from HOPG are amplified by the deposition of Pt due to a more pronounced implantation of Pt into MFG than into HOPG. Work is ongoing to better understand why this difference occurs and to determine the influence of the Pt deposition and surface oxidation. More interestingly, Pt/MFG-H shows the expected frequency response curve shape, although further investigations are needed to better understand the repulsion and attractive forces that result in a higher physical frequency response.

Overall, the early results obtained for HOPG and MFG samples with Pt deposited are qualitatively comparable. With the EQCN analysis we show that we have not changed the resonance of the quartz crystal and we can prepare samples using the MFG substrate as we do for HOPG. The EQCN technique may now be used to better study Pt nanoparticles supported on a carbon substrate and tentative inferences made to practical 3-D applications.

## 3.5 References

[1] Fortuin, A. C., Jackson, C., Carleschi, E., Doyle, B. P., Shnier, A., Kriek, R. J., Ray, S. C., Billing, D. G., Wamwangi, D., Scherer, G. G., and Levecque, P. B. J., *Towards practical applications of EQCN experiments to study Pt anchor sites on carbon surfaces*. Electrocatalysis, 2018. **9**(2): p. 271-278.

[2] Buttry, D. A. and Ward, M. D., *Measurement of interfacial processes at electrode surfaces with the electrochemical quartz crystal microbalance*. Chemical Reviews, 1992. **92**: p. 1355-1379.

[3] Schmickler, W., Interfacial Electrochemistry. 1996: Oxford University Press.

[4] Ratieuville, Y., Viers, P., Alexandre, J., and Durand, G., *A new electrochemical cell adapted to quartz crystal microbalance measurements*. Electrochemistry Communications, 2000. **2**(12): p. 839-844.

[5] Vatankhah, G., Lessard, J., Jerkiewicz, G., Zolfaghari, A., and Conway, B. E., *Dependence of the reliability of electrochemical quartz-crystal nanobalance mass responses on the calibration constant, $C_f$: Analysis of three procedures for its determination*. Electrochimica acta, 2003. **48**(11): p. 1613-1622.

[6] Jeffrey, C. A., Storr, W. M., and Harrington, D. A., *Electrochemical quartz-crystal microbalance study of silver and copper electrodeposition on bare and iodine-covered platinum electrodes*. Journal of Electroanalytical Chemistry, 2004. **569**(1): p. 61-70.

[7] Keita, B., Nadjo, L., Belanger, D., Wilde, C. P., and Hilaire, M., *Electrochemical quartz crystal microbalance: evidence for the adsorption of heteropoly and isopoly anions on gold electrodes*. Journal of Electroanalytical Chemistry, 1995. **384**(1): p. 155-169.

[8] Gu, N., Niu, L., and Dong, S., *Simultaneous determination of both the calibration constant in an electrochemical quartz crystal microbalance and the active surface area of a polycrystalline gold electrode*. Electrochemistry Communications, 2000. **2**(1): p. 48-50.

[9] Kim, J. and Jerkiewicz, G., *Influence of the surface roughness of platinum electrodes on the calibration of the electrochemical quartz-crystal nanobalance*. Analytical Chemistry, 2017. **89**(14): p. 7462-7469.

[10] Wink, T., Van Zuilen, S. J., Bult, A., and Van Bennekom, W. P., *Self-assembled monolayers for biosensors*. Analyst, 1997. **122**(4): p. 43R-50R.

[11] Janata, J., Josowicz, M., Vanýsek, P., and DeVaney, D. M., *Chemical sensors*. Analytical Chemistry, 1998. **70**(12): p. 179-208.

[12] Bizet, K., Gabrielli, C., and Perrot, H., *Immunodetection by quartz crystal microbalance*. Applied Biochemistry and Biotechnology, 2000. **89**(2): p. 139.

[13] Jerkiewicz, G., Vatankhah, G., Lessard, J., Soriaga, M. P., and Park, Y.-S., *Surface-oxide growth at platinum electrodes in aqueous $H_2SO_4$: Reexamination of its mechanism through combined cyclic-voltammetry, electrochemical quartz-crystal nanobalance, and Auger electron spectroscopy measurements*. Electrochimica Acta, 2004. **49**(9–10): p. 1451-1459.

[14] Jerkiewicz, G., *Electrochemical hydrogen adsorption and absorption part 1: Under-potential deposition of hydrogen*. Electrocatalysis, 2010. **1**(4): p. 179-199.

[15] Jerkiewicz, G., Vatankhah, G., Tanaka, S.-i., and Lessard, J., *Discovery of the potential of minimum mass for platinum electrodes*. Langmuir, 2011. **27**(7): p. 4220-4226.

[16] Watanabe, M. and Uchida, H., *Electrocatalysis at platinum and bimetallic alloys*, in *Fuel cell catalysis: a surface science approach*, M.T.M. Koper, Editor. 2009, John Wiley & Sons. p. 317-344.

[17] Ofstad, A. B., Thomassen, M. S., Gomez de la Fuente, J. L., Seland, F., Møller-Holst, S., and Sunde, S., *Assessment of platinum dissolution from a Pt/C fuel cell catalyst: An electrochemical quartz crystal microbalance study*. Journal of The Electrochemical Society, 2010. **157**(5): p. B621-B627.

[18] Cline, K. K., McDermott, M. T., and McCreery, R. L., *Anomalously slow electron transfer at ordered graphite electrodes: Influence of electronic factors and reactive sites*. Journal of Physical Chemistry, 1994. **98**(20): p. 5314-5319.

[19] McCreery, R. L., Cline, K. K., McDermott, C. A., and McDermott, M. T., *Control of reactivity at carbon electrode surfaces*. Colloids and Surfaces A, 1994. **93**(0): p. 211-219.

[20] Jerkiewicz, G., Vatankhah, G., Zolfaghari, A., and Lessard, J., *Analysis of the mass response of the electrochemical quartz-crystal nanobalance in horizontal and vertical geometry*. Electrochemistry Communications, 1999. **1**(9): p. 419-424.

[21] Kim, U. J., Furtado, C. A., Liu, X., Chen, G., and Eklund, P. C., R*aman and IR spectroscopy of chemically processed single-walled carbon nanotubes*. Journal of the American Chemical Society, 2005. **127**(44): p. 15437-15445.

[22] Falch, A., Lates, V., and Kriek, R. J., *Combinatorial plasma sputtering of $Pt_xPd_y$ thin film electrocatalysts for aqueous $SO_2$ electro-oxidation*. Electrocatalysis, 2015. **6**(3): p. 322-330.

[23] Scherrer, P., *Bestimmung der größe und der inneren Struktur von Kolloidteilchen mittels Röntgenstrahlen*. Nachr. Ges. Wiss. Gottingen, Math. Phys., 1918. **2**(July): p. 98-100.

[24] Evans, S. and Thomas, J. M., *The chemical nature of ion-bombarded carbon: A photoelectron spectroscopic study of "cleaned" surfaces of diamond and graphite*. Proceedings of the Royal Society of London. A. Mathematical and Physical Sciences, 1977. **353**(1672): p. 103-120.

[25] Xie, Y. and Sherwood, P. M. A., *X-ray photoelectron-spectroscopic studies of carbon fiber surfaces. 11. Differences in the surface chemistry and bulk structure of different carbon fibers based on poly (acrylonitrile) and pitch and comparison with various graphite samples*. Chemistry of Materials, 1990. **2**(3): p. 293-299.

[26] Gardner, S. D., Singamsetty, C. S. K., Booth, G. L., He, G.-R., and Pittman, C. U., *Surface characterization of carbon fibers using angle-resolved XPS and ISS*. Carbon, 1995. **33**(5): p. 587-595.

[27] Yue, Z. R., Jiang, W., Wang, L., Gardner, S. D., and Pittman Jr, C. U., *Surface characterization of electrochemically oxidized carbon fibers*. Carbon, 1999. **37**(11): p. 1785-1796.

[28] Bard, A. J. and Faulkner, L. R., *Electrochemical methods: Fundamentals and applications*. 2nd ed. 2001: John Wiley & Sons, Inc.

[29] Nicholson, R. S., *Theory and application of cyclic voltammetry for measurement of electrode reaction kinetics*. Analytical Chemistry, 1965. **37**(11): p. 1351-1355.

[30] Mayrhofer, K. J. J., Blizanac, B. B., Arenz, M., Stamenkovic, V. R., Ross, P. N., and Markovic, N. M., *The impact of geometric and surface electronic properties of Pt-catalysts on the particle size effect in electrocatalysis*. The Journal of Physical Chemistry B, 2005. **109**(30): p. 14433-14440.

[31] Jerkiewicz, G., DeBlois, M., Radovic-Hrapovic, Z., Tessier, J.-P., Perreault, F., and Lessard, J., *Underpotential deposition of hydrogen on benzene-modified Pt(111) in aqueous $H_2SO_4$*. Langmuir, 2005. 21(8): p. 3511-3520.

[32] Kim, J., Munro, A., Beauchemin, D., and Jerkiewicz, G., *Limits of detection and quantification of electrochemical quartz-crystal nanobalance in platinum electrochemistry and electrocatalysis research*. Analytical Chemistry, 2016. **88**(21): p. 10599-10604.

[33] Kim, J., Urchaga, P., Baranton, S., Coutanceau, C., and Jerkiewicz, G., *Interfacial structure of atomically flat polycrystalline Pt electrodes and modified Sauerbrey equation*. Physical Chemistry Chemical Physics, 2017. **19**(33): p. 21955-21963.

[34] Kim, J., *Comprehensive study of the influence of surface roughness of platinum electrodes on their interfacial mass changes as examined using the electrochemical quartz-crystal nanobalance*, in *Dept. of Chemistry*. 2017, Queen's University.

# Chapter 4
# Towards Practical Applications of EQCN Experiments to Study Pt Anchor Sites on Carbon Surfaces: Part 2 – Studying Potential Cycling of Pt Electrocatalysts

## 4.1 Introduction

The use of the electrochemical quartz crystal nano-balance (EQCN) is a technique that has seen little use in studying electrocatalyst durability. Much of the EQCN work has been used to study reactions and adsorption occurring at metal surfaces [1-20], in particular Pt and Au surfaces. However, limited work has been done to apply this technique in studying Pt/C electrocatalysts for polymer electrolyte fuel cell (PEFC) applications.

Works by Ofstad *et al.* [21] and Wickman *et al.* [22] are two of the few studies which studied Pt dissolution of real-world electrocatalysts by EQCN. While, both have studied degradation mechanisms of Pt/C successfully, there were some shortfalls when compared to conventional Pt/C degradation testing methods.

Wickman *et al.* [22] followed a similar approach as we have in this work, however, they deposited much lower loadings of Pt and did not explain the changes in their frequency response before, during, and after degradation studies. However, their degradation study only expanded a total of 30 cycles at 50 $mV.s^{-1}$, thus giving insufficient data to understand the degradation mechanisms of Pt dissolution and use the EQCN to its full potential. On the other hand, Ofstad *et al.* [21] studied a system whereby a Pt/C ink was deposited on a Au electrode and studied the effects of Pt dissolution in the presence of $Cl^-$. Thus, their work incorporates many extra variables that are difficult to account for using the EQCN technique.

This study differs from Wickman *et al.*'s [22] and Ofstad *et al.*'s [21] works by following DoE approved degradation protocols for Pt dissolution by load cycling. This is coupled with modifications to the graphite substrate, as discussed previously, and investigates the influence of these oxygen groups on the mobility of Pt.

## 4.2 Experimental Methods

All electrochemical measurements were conducted using a Bio-Logic SP-200 potentiostat. EQCN measurements were conducted using a Seiko EG&G QCM922A, in a home-built Faraday cage and vibration free table (fig. 4.1). The packaged EC-Lab v11.1x software was used to control both instruments.

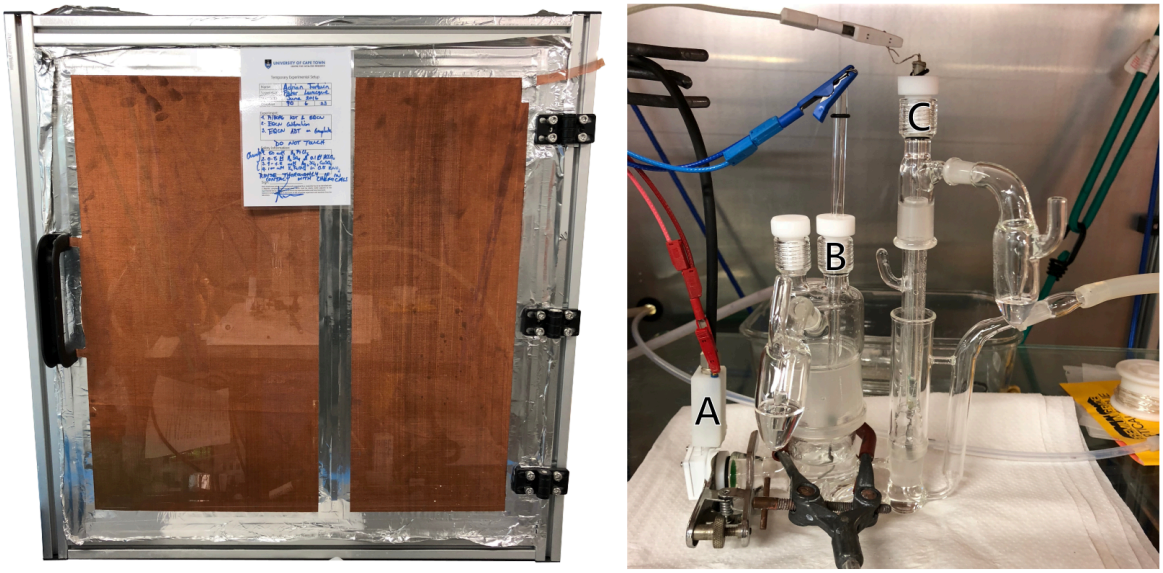


**Figure 4.1 Experimental setup, left is the Faraday cage and right is the cell within the Faraday cage, as developed by Prof Jerkiewicz. The working electrode (A), the counter electrode (B), and the reference electrode (C) are described in text**

### 4.2.1 Electrodes

A custom-built, two-compartment cell (developed by Prof Jerkiewicz) was used and cleaned by submerging in NOCHROMIX® (Godax Laboratories, Inc.) overnight. A Teflon™ quartz holder houses the planar quartz crystals cut in the AT orientation, in the vertical cell orientation as described by Jerkiewicz *et al.* [4]. The AT-cut quartz crystal was coated with a 100 nm Ti layer, followed by sputtering of approximately 300 nm carbon layer to fabricate a mirror finish graphite (MFG) quartz crystal with a roughness of 60 nm. The base resonant frequency was 9.13 MHz and all quartz crystals were supplied by Bio-Logic.

Because the MFG quartz crystals are layered, as illustrated in fig. 4.2, following the same procedures to modify the carbon surface as discussed in sections 2.2.1, 3.2.1, and Fortuin *et al.* [23] could not be followed. Initial modifications resulted in the delamination of the titanium layer and subsequently the carbon layer. This suggests that the sputtering of the carbon film does not lap the Ti layer, hence leaving it available for attack under the aggressive chemical environment. In order to overcome this challenge, a homogeneous layer of nitrocellulose was applied to the quartz crystal, leaving only the 5 mm diameter opening of the graphite as illustrated in fig. 4.2 (b).

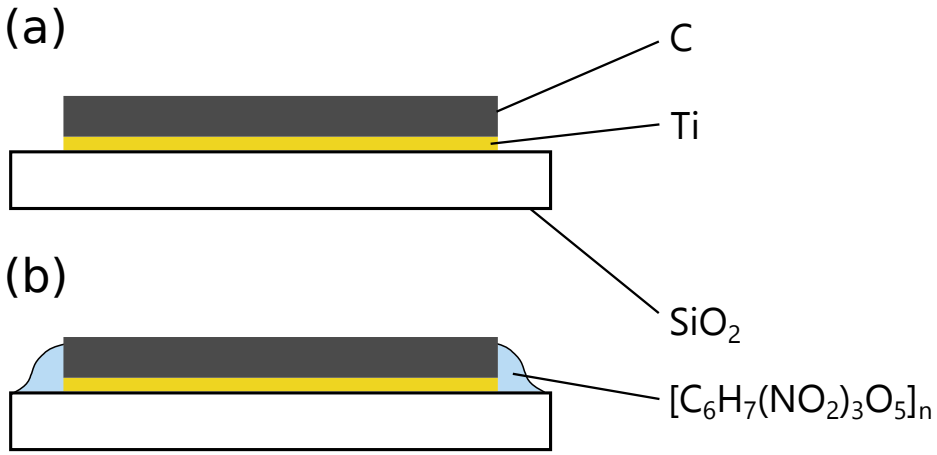


**Figure 4.2 Schematic cross section of quartz crystal (a) as received, and (b) with nitrocellulose lacquer applied**

The MFG quartz crystal was then refluxed in Fenton's reagent for 24 hours at 80 °C [24] to synthesise a hydroxyl modified MFG sample referred to as MFG-H. Alternatively, samples were refluxed in a 1:1 ratio of 5 N $HNO_3$ and $H_2SO_4$ for 24 hours at 120 °C [25] and are referred to as MFG-A. As for the samples prepared in chapters 2 and 3, constant time and temperatures were chosen to ensure the concentration of potential anchor sites on the surface is maximised. Prior to depositing Pt, all samples were washed and dried with aliquots of acetone, ethanol, isopropanol, and deionised water to remove the nitrocellulose. Pt was then deposited onto the modified and unmodified surfaces at loadings of 20 $\mu$g.cm$^{-2}$ and 50 $\mu$g.cm$^{-2}$ by DC magnetron sputtering (PVD Products, USA). This was accomplished by using a Pt sputtering target (1.5" diameter x ⅛" thick) obtained from ACI Alloys (USA) having a purity of 99.95%. Prior to sputtering, the vacuum chamber of the sputtering apparatus was pumped down to a base pressure of approximately $5 \times 10^{-7}$ Torr. Sputtering of Pt, under an Ar plasma, was conducted at a chamber pressure of 8 mTorr and an Ar flow of 15 sccm. The sputtering rate (nm.min$^{-1}$) of Pt was calibrated as described by Falch *et al.* [26] with minimal deviation in the sputtered layer from sample to sample. The substrates were positioned onto an in-house manufactured stainless-steel tray (illustrated in fig. 3.1 in section 3.2.1) that slots into a housing fitted with a computer controlled XY motor below a fixed aperture, allowing for dedicated sputtering of individual samples.

A reversible hydrogen electrode (RHE) using Pt foil (Alfa Aesar, 99.999%) was used as the reference electrode and a Au coil as the counter electrode.

### 4.2.2 Electrochemical Testing

Prior to conducting all electrochemical measurements on the MFG samples, cyclic voltammograms ($i$ vs $E$) of $Pt_{poly}$ were measured in aqueous 0.5 M $H_2SO_4$ prepared from 99.999 wt.% $H_2SO_4$ (Sigma Aldrich) and 18.2 MΩ.cm nano-pure water. All measurements were carried out at room temperature and under an inert Ar atmosphere (99.999%, Air Products). The

electric potential was cycled between 0.05 and 1.50 V vs RHE to ensure cleanliness and reproducible functioning of the electrochemical setup.

Following the above, conditioning of the MFG quartz crystals was achieved by cycling the potential between 0.00 and 1.50 V vs RHE for 30 cycles at a scan rate of 250 $mV.s^{-1}$ to remove any surface contaminants due to modification and sputtering. This ensures that all organics are oxidised from the surface. A further 200 cycles at 250 $mV.s^{-1}$ and between 0.00 and 1.30 V vs RHE were performed in order to destress the quartz crystal as described in Jerkiewicz *et al.* [4] and Kim [27]. While, Jerkiewicz *et al.* [4] and Kim [27] state that 1,000 cycles are required to destress near surface edges of the quartz crystal, this has to be limited for this study in order to preserve the integrity of the electrocatalyst for accelerated durability testing. However, the quartz crystal is destressed such that a reproducible characteristic $Pt_{poly}$ current and frequency response with minimal frequency drift is obtained. This indicates cleanliness of the electrode and electrolyte, and stability of the quartz crystal. Lastly, 15 cycles at 50 $mV.s^{-1}$ between 0.05 and 1.30 V vs RHE were performed in order to obtain an initial mass voltammogram.

For the accelerated durability test, the protocol outlined in Ohma *et al.* [28] and the US DoE report [29] were employed. An initial cyclic voltammogram was recorded at 50 $mV.s^{-1}$ between 0.05 and 1.30 V vs RHE for 10 cycles. The choice of using 10 cycles is to assist in averaging data in order to obtain accurate mass voltammograms as described in Jerkiewicz *et al.* [4]. Following this, the potential was held at 0.60 V vs RHE for 30 s, then stepped up to 1.00 V vs RHE for 3 s, and then stepped down to 0.60 V vs RHE and held for 3 s. This potential step was repeated 10,000 times, with 10 cyclic voltammograms recorded, as above, at intervals. Cyclic voltammograms were recorded after every 10 potential step cycles for the first 100 cycles, every 100 cycles between 100 and 1,000 cycles, and every 1,000 cycles thereafter. It must be noted, that the frequency response, which can be represented as a mass voltammogram, is recorded in parallel with the cyclic voltammogram. It is further noted that due to the fragility of the quartz crystals, and added stresses incurred to chemically modify the graphite layer, only one of each MFG sample was measured for its frequency response, however cyclic voltammograms

were measured for repeat samples to represent reproducibility. A $Pt_{poly}$ CV of multiple samples is illustrated in Appendix B.

### 4.2.3 Physical Characterisation

X-ray diffraction (XRD) measurements were taken using a Bruker D8 Advance in the Bragg-Brentano geometry with a Co anode ($\lambda$ = 1.79026 Å), primarily using a $2\theta$ range of 20 - 120° with 0.043° steps. Samples were placed in a zero-background sample holder and the sample was placed such that they were in line with a straight edge across the holder. Measurements were repeated using a $2\theta$ range of 42 – 50° with 0.037° steps and a dwell time of 13.5 s to increase resolution of the Pt (111) spectrum.

## 4.3 Results and Discussion

### 4.3.1 Calibration of the EQCN

In order to confirm that the EQCN system is working optimally, the determination of the calibration factor was determined by applying the Sauerbrey equation (equation 4.1) to classic underpotential deposition of metal salts on a $Pt_{poly}$ electrode.

$$\Delta m = -\frac{n\sqrt{\rho_q \mu_q}}{2f_0^2}\Delta f = -\frac{N\rho_q}{f_0^2}\Delta f = -C_f \Delta f \qquad (4.1)$$

whereby:

$\Delta f$ is the measured frequency change (Hz)

$f_0$ is the baseline frequency of the quartz crystal in air (~9.00 MHz)

$n$ is the harmonic mode ($n$ = 1)

$\rho_q$ is the density of quartz (2.648 $g.cm^{-3}$)

$\mu_q$ is the shear modulus of quartz (2.947 x $10^{11}$ $g.cm^{-1}.s^{-2}$)

$\Delta m$ is the associated mass change (g)

$N$ is a frequency parameter which is dependent on the of cut of quartz (1661 kHz.mm) [30]

$C_f$ is the calibration factor determined experimentally (ng.Hz$^{-1}$.cm$^{-2}$)

Before introducing a metal salt, the as received $Pt_{poly}$ and MFG quartz crystal were destressed for 1,000 cycles between 0.0 and 1.5 V vs RHE at 250 mV.s$^{-1}$. Cyclic voltammograms were recorded at 50 mV.s$^{-1}$ to ensure that the current response represented the standard polycrystalline Pt and graphite current responses in 0.5 M $H_2SO_4$ as is seen in fig. 4.3 below.

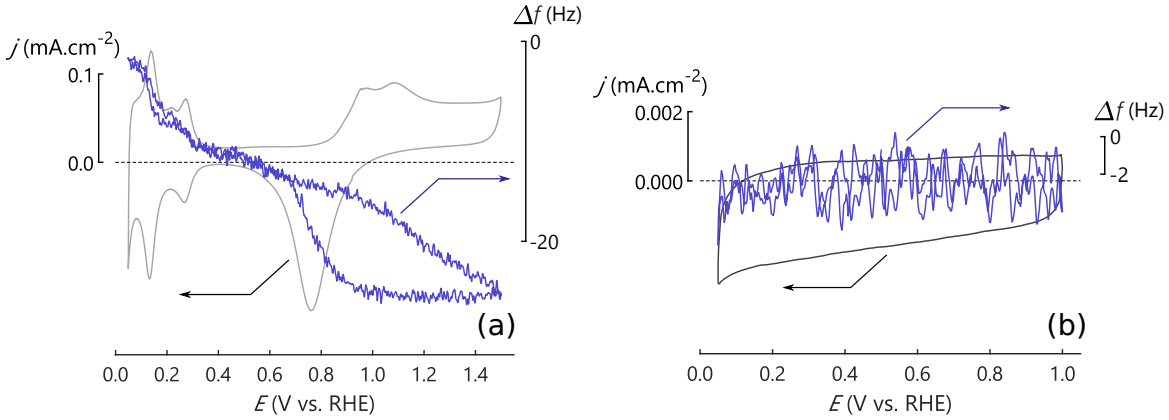


**Figure 4.3 Current and frequency responses of (a) $Pt_{poly}$ and (b) graphite in room temperature Ar saturated 0.5 M $H_2SO_4$ at 50 mV.s$^{-1}$**

The current responses are as expected, with the $Pt_{poly}$ frequency response following the standard $Pt_{poly}$ frequency response meticulously developed by Jerkiewicz [1-4,8] over the years. The frequency response for graphite, however, shows no mass change. This is to be expected, as the smooth graphite surface has no surface reactions or ion adsorption within the potential range measured [23,31-33].

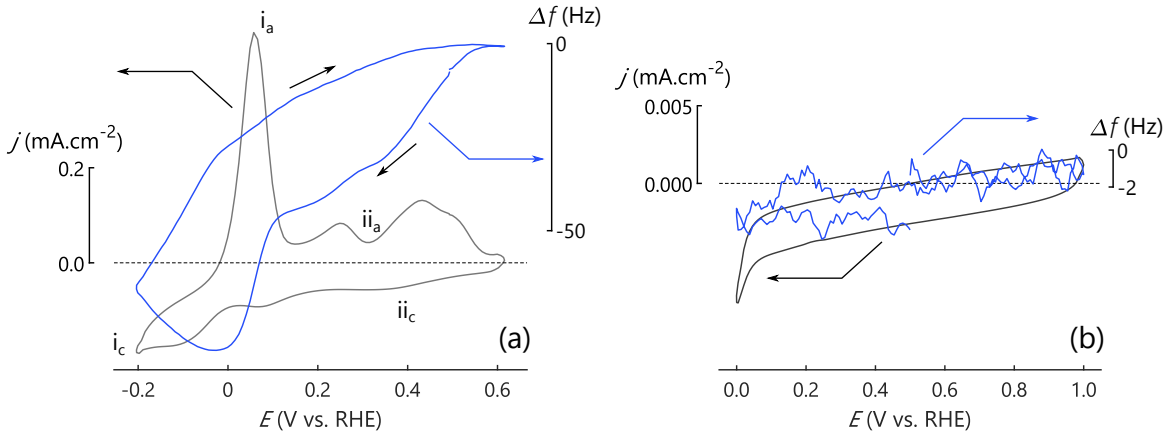


**Figure 4.4 Current and frequency responses of Cu deposition on (a) $Pt_{poly}$ and (b) graphite in room temperature Ar saturated 1 mM $Cu^{2+}_{(aq)}$ + 0.5 M $H_2SO_4$ at 50 $mV.s^{-1}$. Current responses at $i_a/i_c$ represent bulk Cu deposition and stripping, while $ii_a/ii_c$ represents underpotential deposition and stripping**

A 1 mM $CuSO_{4\,(aq)}$ in 0.5 M $H_2SO_4$ was introduced into the system and the current response was recorded over a potential range of -0.2 – 1.0 V vs RHE as illustrated in fig. 4.4. For $Pt_{poly}$, an upper vertex potential (0.65 V vs RHE) below the onset of $PtO_x$ was chosen to exclude any influence from $PtO_x$ formation on Cu deposition (fig. 4.4a).

In the case of Cu deposition on $Pt_{poly}$, we measured a typical current response as reported in literature [10,34-39]. Below 0.1 V vs RHE, we see the onset of bulk (or over potential deposition, OPD) Cu deposition on $Pt_{poly}$. This is evident, as a large mass addition is observed in the frequency response by the steep gradient change of the frequency response between 0.0 and 0.1 V vs RHE. For Cu deposition on graphite (fig. 4.4b) we see little interaction, as there are no surfaces for nucleation of $Cu^0$. However, the changes in the current response are in line with Cu UPD as reported by Jaya *et al.* [40], which suggests deposition and stripping occur simultaneously, hence no appreciable frequency response. However, if we consider electron transfer at modified and disordered graphite surfaces [32,41], we may see adsorption, nucleation and deposition of Cu on graphite, although this is outside of the scope of this work.

With the successful reproduction of Cu UPD on $Pt_{poly}$, we can determine the $C_f$ value by determining the gradient of $\Delta q / \Delta f$ from Faraday's first law of electrolysis in equation 4.2:

$$C_f = \left(\frac{M}{zF}\right)\left(\frac{\Delta q}{\Delta f}\right) = \left(\frac{M}{zF}\right)\left(\frac{j\Delta t}{\Delta f}\right) \qquad (4.2)$$

whereby:

$\Delta q$ is the change in charge as a result of current flow ($C.cm^{-2}$)

$F$ is Faraday's constant (96,485 $C.mol^{-1}$)

$M$ is the molar mass of the metal being electrodeposited (63.546 $g.mol^{-1}$ for Cu)

$z$ is the charge of the metal solution being reduced (+2 for Cu)

$j$ is the current density ($A.cm^{-2}$)

$\Delta t$ is the time over which the current density, $j$, is applied (s)

For this system, we obtain a $C_f$ value of 5.47 $ng.Hz^{-1}.cm^{-2}$, which is in good agreement with the value determined by Jerkiewicz *et al.* [4] (5.61 $ng.Hz^{-1}.cm^{-2}$) and by theory (5.45 $ng.Hz^{-1}.cm^{-2}$). However, this is for Cu UPD on $Pt_{poly}$, and there is no guarantee that this $C_f$ value would apply to all graphite systems due to the effects of electron transfer at carbon mono-vacancies and oxygen terminating groups [32,41]. We can conclude, however, that the system is operating optimally and as expected.

### 4.3.2 Accelerated Durability Tests – Electrochemistry

In order to create suitable reference of comparison between MFG samples, load cycling was carried out on a $Pt_{poly}$ quartz crystal to which all MFG samples could be compared. Initial results showed a shift of the cyclic voltammogram downwards into a more reducing environment as indicated in fig. 4.5 below.

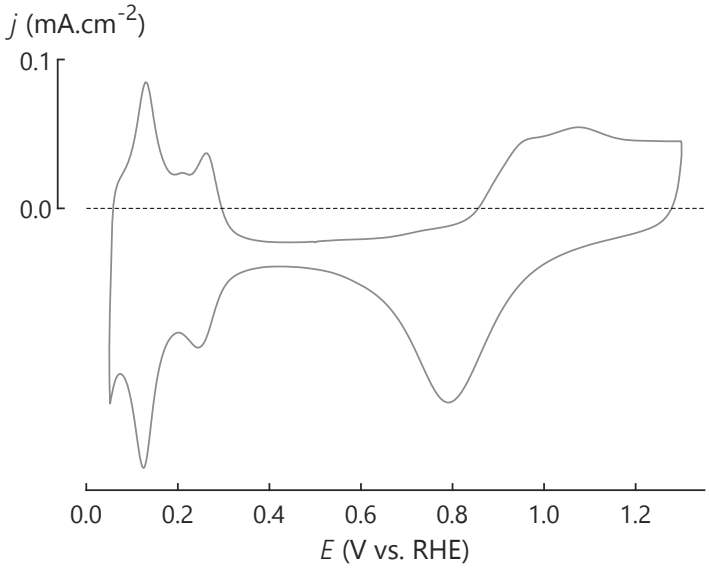


**Figure 4.5 $Pt_{poly}$ current response in room temperature Ar saturated 0.5 M $H_2SO_4$ at 50 mV.$s^{-1}$**

While the shape of the current response is typical of $Pt_{poly}$, the shift down suggests that there is either (i) a small amount of hydrogen crossover from the RHE electrode, creating a more reducing environment, or (ii) residual current response from the oxygen reduction reaction. This downward shift has been corrected for all cyclic voltammograms, however the reducing environment has no noticeable effects on the results, in particular the $H_{upd}$ region.

With the residual reducing effect taken into account, the results for load cycling of $Pt_{poly}$ are presented below in fig. 4.6.

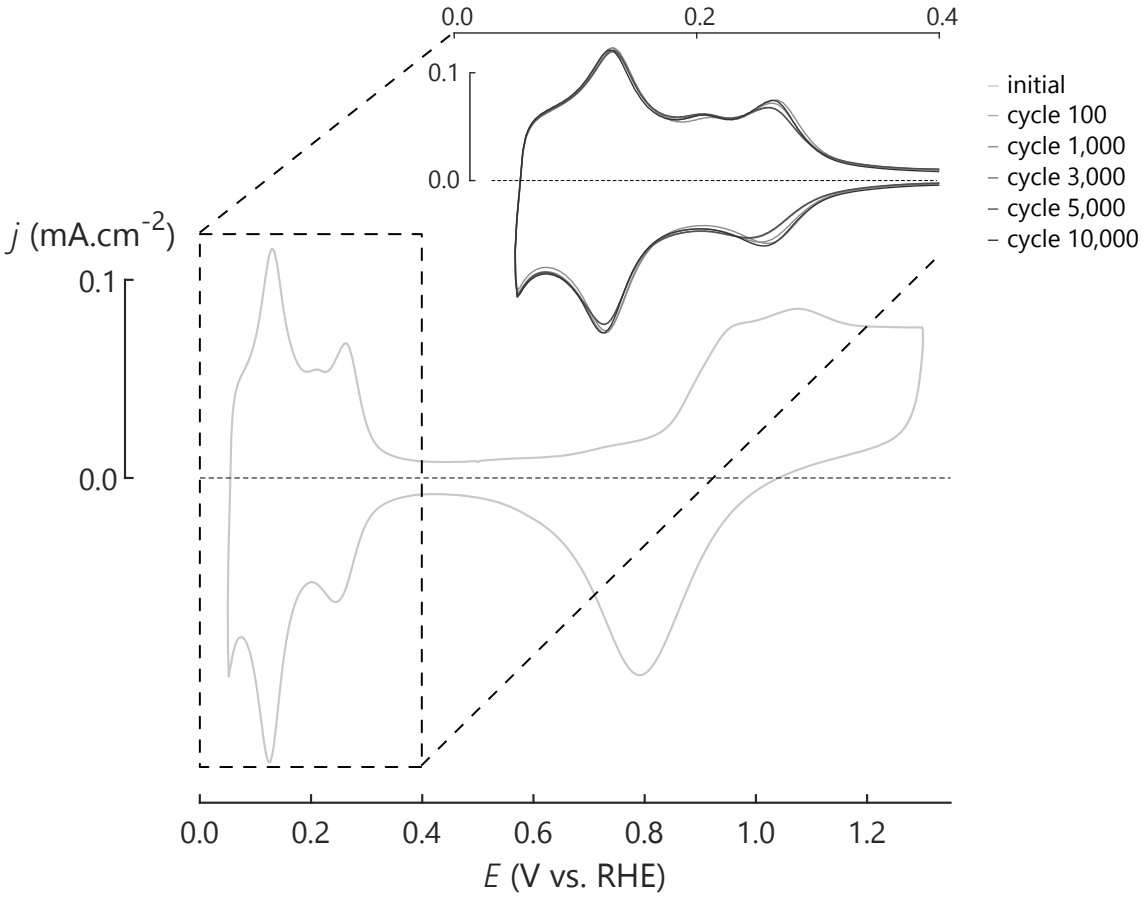


**Figure 4.6 Current response of $Pt_{poly}$ in room temperature Ar saturated 0.5 M $H_2SO_4$ at 50 mV.$s^{-1}$, inset is the hydrogen region used to determine the ECSA over 10,000 cycles**

From fig. 4.6 we can see little change in the $H_{upd}$ region over the course of 10,000 degradation cycles. This was initially unexpected, but on further analysis, there was a thin layer of Pt deposited on the O-ring of the quartz holder as illustrated in fig. 4.7 below.

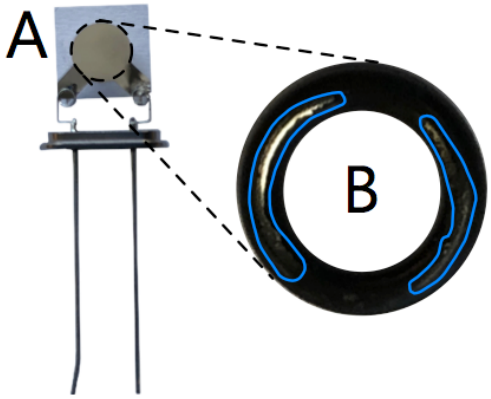


**Figure 4.7 (A) $Pt_{poly}$ quartz crystal with (B) the O-ring on the electrolyte side with Pt deposits outlined in blue.**

With the noticeable deposition of Pt on the O-ring, it is peculiar that a significant change in $H_{upd}$ is not observed. Considering that the $Pt_{poly}$ quartz crystal consists of a thick 300 nm layer of bulk Pt, it is easy to assume that this bulk Pt layer was reduced in thickness, but not eliminated. Furthermore, the electrochemical active surface area (ECSA) is a measure of available Pt for reaction, not a measure for quantity of Pt, thus measuring of ECSA is not suitable in this instance [42].

Despite the unsuitability of ECSA for bulk $Pt_{poly}$ electrodes, it is possible to use as a baseline for the measured current response changes with time, this provides a reference point in which to compare Pt dissolution in the MFG samples.

Potential cycling for all Pt/MFG samples were measured as for $Pt_{poly}$, and can be found in Appendix B. A plot of the percentage change in ECSA versus cycle number for loadings of 20 $\mu g.cm^{-2}$ (fig. 4.8) and 50 $\mu g.cm^{-2}$ (fig. 4.9) on Pt/MFG are presented below.

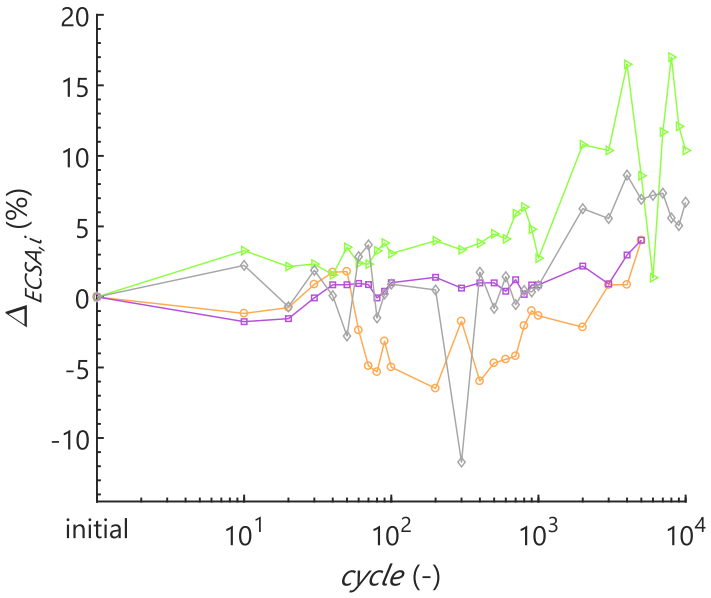


**Figure 4.8 Percentage change in ECSA with increasing degradation cycles a loading of 20 $\mu g.cm^{-2}$ Pt with ○ representing MFG-P, ▷ representing MFG-H, □ representing MFG-A, and ◇ representing $Pt_{poly}$**

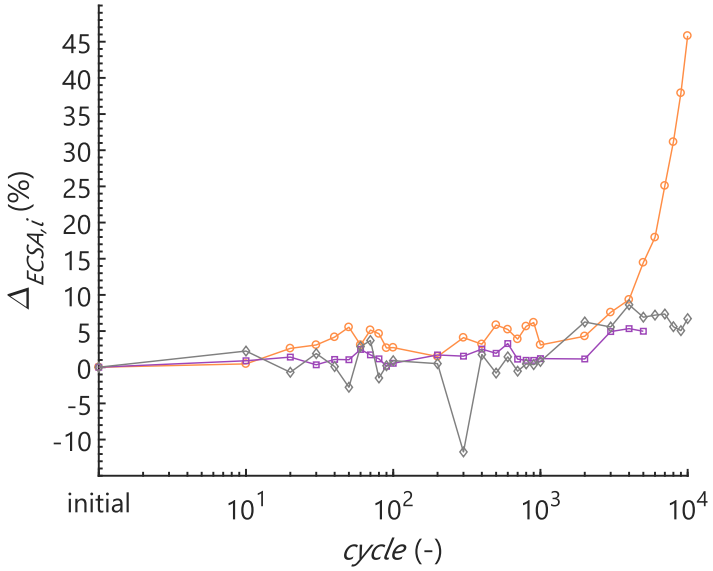


**Figure 4.9 Percentage change in ECSA with increasing degradation cycles a loading of 50 $\mu$g.cm$^{-2}$ Pt with ○ representing MFG-P, □ representing MFG-A, and ◇ representing Pt$_{poly}$**

As for Pt$_{poly}$, not much change is seen in the H$_{upd}$ region or significant changes in ECSA over 5,000 – 10,000 cycles for all samples, except for 50 $\mu$g.cm$^{-2}$ Pt/MFG-P. The result of 50 $\mu$g.cm$^{-2}$ Pt/MFG-P was unexpected and would indicate that a mechanism of partial exfoliation occurred. This is clear in H$_{upd}$ region after 10,000 cycles in fig. 4.10, where such a rapid decrease in ECSA can only be attributed to partial exfoliation of the Pt layer. For all other samples, after approximately 4,000 cycles (fig. 4.8 and fig. 4.9), Pt dissolution effects begin to become more apparent, regardless of loading.

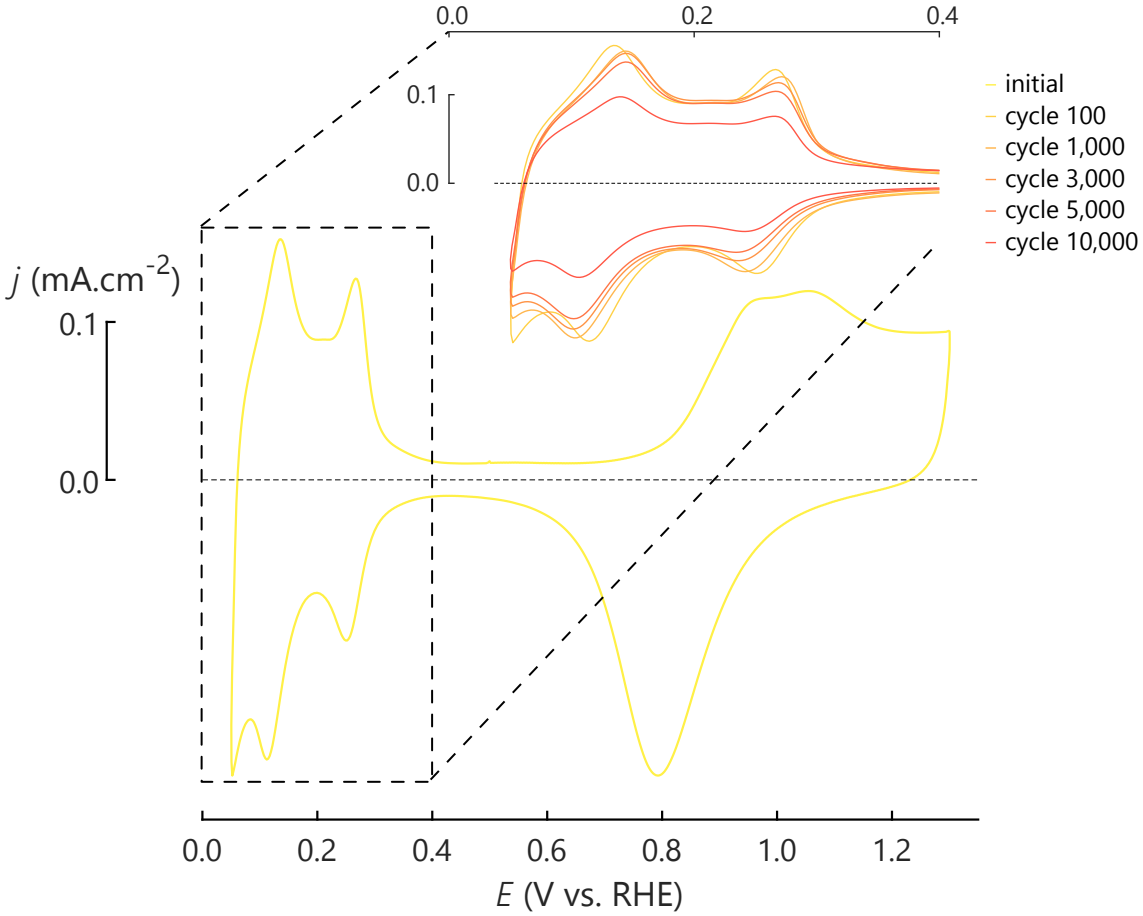


**Figure 4.10 Current response of 50 $\mu$g.cm$^{-2}$ Pt/MFG-P in room temperature Ar saturated 0.5 M $H_2SO_4$ at 50 mV.s$^{-1}$, inset is the hydrogen region used to determine the ECSA over 10,000 cycles**

The relative changes in ECSA for each sample doesn't share much information on the support and Pt dissolution over a few cycles. In order to garner some idea of the surface chemistry, the absolute ECSA for each sample at each loading needs to be considered. This is summarised in table 4.1 below.

The absolute ECSA between the MFG samples and the HOPG samples from section 2.3.3 show an increase in available surface area for the MFG samples. This is expected, as the MFG samples have a 60 nm surface roughness, hence having a larger actual surface area per geometric area.

With this increased roughness, the stability of Pt will be greater and will interact with the surface more strongly [32,41].

**Table 4.1 Initial and final ECSA for each sample compared to the final ECSA of the corresponding HOPG samples as well as the percentage change in ECSA from initial to final for both MFG and HOPG samples.**

| Sample | Electrochemical Active Surface Area ($m^2.g_{Pt}^{-1}$) | | | | |
|---|---|---|---|---|---|
| | $MFG_i$ | $MFG_f$ | $HOPG_f$ | $\% \Delta ECSA_{MFG}$ | $\% \Delta ECSA_{HOPG}$ |
| $Pt_{poly}$* | R = 1.25 | R = 1.17 | - | -6.72 | - |
| 20 $\mu$g.cm$^{-2}$ Pt/MFG-P | 9.17 | 8.80 | 6.12 | -4.01 | -13.3 |
| 20 $\mu$g.cm$^{-2}$ Pt/MFG-H | 14.9 | 13.4 | 3.40 | -10.4 | -13.3 |
| 20 $\mu$g.cm$^{-2}$ Pt/MFG-A | 16.3 | 15.7 | 4.03 | -4.02 | -15.3 |
| 50 $\mu$g.cm$^{-2}$ Pt/MFG-P | 4.09 | 2.22 | - | -45.8 | - |
| 50 $\mu$g.cm$^{-2}$ Pt/MFG-A | 7.53 | 7.15 | - | -4.97 | - |

* roughness factor for $Pt_{poly}$ is presented here

The trend of increasing ECSA from MFG-A > MFG-H > MFG-P remains as with the HOPG samples, which could suggest that the acid treated MFG interacts with Pt more strongly, creating discrete islands of weak electron withdrawing oxygen sites. This further supports the conclusions drawn in chapter 2. However, further insight is needed into the mechanism of dissolution.

### 4.3.3 Accelerated Durability Tests – Frequency Response

The usefulness of the EQCN technique, is the recording of frequency response in parallel with electrochemical measurements. Further to this, the EQCN technique allows us to better understand the interfacial chemical environment of the electrode. This is due to the sensitivity of the instrument towards small mass variations, so that measurements of the effects of capacitance and complex double layer charging phenomenon can be studied [1,43]. Thus, significant differences between the different MFG samples based on the chemical modification is expected.

However, one short fall of the EQCN is its ability to measure bulk mass loss over extended periods of time. This is because the system, in general, suffers from drift due to multiple factors, especially when running an experiment over a period of 13 hours. Hence, using the EQCN to measure absolute mass loss would be inaccurate, and thus it can only be used as a qualitative tool. Rough estimates of mass loss using the $C_f$ for $Pt_{poly}$ are summarised in table 4.2 further on in this chapter. It should be emphasised that the $C_f$ value does not take into roughness effects or the influences of the chemical modifications of the MFG samples, hence these are rough estimates. Further to this, the influence of carbon corrosion is difficult to separate from Pt dissolution using the EQCN and would require a modification of the Sauerbrey equation to deconvolute parallel mechanisms, however it is assumed carbon corrosion is negligible in this study.

This section focusses exclusively on the Pt-C interactions and less on the absolute mass loss during potential cycling. Again, as a baseline, the frequency response of $Pt_{poly}$ at intervals as with the cyclic voltammograms was investigated (fig. 4.11).

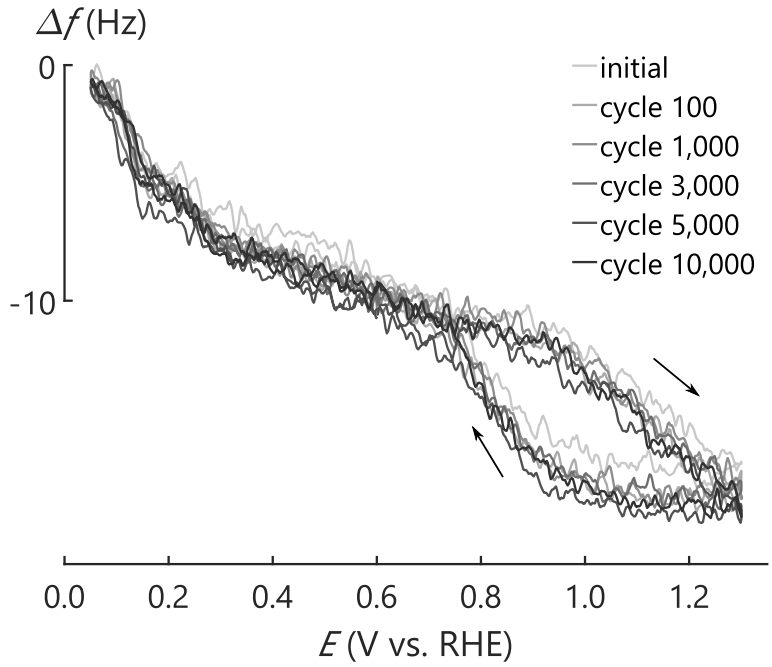


**Figure 4.11 Frequency response of $Pt_{poly}$ in room temperature Ar saturated 0.5 M $H_2SO_4$ at 50 mV.$s^{-1}$**

Together with the CV of $Pt_{poly}$, the electrochemical processes can be explained for the frequency response curve in fig. 4.11. With an increase in potential in the range $0.5 < E < 1.3$ V vs RHE (*cf.* fig. 4.6), $Pt_{poly}$ undergoes surface oxidation which results in the formation of a $PtO_x$ layer, this is represented by a decrease in frequency. Decreasing potential in the range $1.2 > E > 0.5$ V vs RHE, the surface $PtO_x$ is reduced to $Pt_{poly}$, hence a positive increase in the frequency response. For the range $E < 0.5$ V vs RHE, more complex phenomena occur such as electrostatic effects due to non-faradaic charge transfer and solvation effects of protons. More importantly, the overall change in frequency of roughly 20 Hz (109 ng.cm$^{-2}$) across the entire potential range (in fig. 4.11) is in good agreement with the values published by Jerkiewicz *et al.* [2,6]. It is interesting to note the consistency of the frequency response as the catalyst is stressed. This data suggests that there is very little surface roughening occurring [7], even with a total mass loss of approximately 215 ng.cm$^{-2}$ for the last 8,000 cycles (table 4.2), where the mass loss is in good agreement with the trends discussed in Xing *et al.* [42]. As with the electrochemistry results above (section 4.3.2), the lack of change in the frequency response points unequivocally that the roughness factor remains fairly constant and Pt dissolution is occurring uniformly across the electrode.

**Table 4.2 Estimated mass loss over the last cycles of each cycle using $C_f$ = 5.47 ng.Hz$^{-1}$.cm$^{-2}$**

| Sample | Cycles | $\Delta$f (Hz) | $\Delta$m (ng.cm$^{-2}$) | Ref. |
|---|---|---|---|---|
| $Pt_{poly}$ | last 8,000 | 40 | 215 | - |
| $Pt_{poly}$ | 5,000 | - | 280 ± 14 | [42] |
| 20 $\mu$g.cm$^{-2}$ Pt/MFG-P | last 3,000 | 70 | 383 | - |
| 20 $\mu$g.cm$^{-2}$ Pt/MFG-H | last 4,000 | 225 | 1,230 | - |
| 20 $\mu$g.cm$^{-2}$ Pt/MFG-A | last 3,000 | 50 | 274 | - |
| 50 $\mu$g.cm$^{-2}$ Pt/MFG-A | last 3,000 | 15 | 82 | - |

The Pt/MFG samples display different frequency response behaviour to $Pt_{poly}$. From fig. 4.12 – 4.14 we see a lack of consistency in the Pt/MFG frequency responses, where each almost levels out after 1,000 cycles. The 50 $\mu$g.cm$^{-2}$ Pt/MFG-A is the exception to this, as well as its frequency response in the $H_{upd}$ region.

For the Pt/MFG-P samples, a similar trend between 20 $\mu$g.cm$^{-2}$ (fig. 4.12a) and 50 $\mu$g.cm$^{-2}$ (fig. 4.12b) loadings is observed, albeit the latter has a larger frequency response. Initially, we record a frequency response at 142 ng.cm$^{-2}$ and 268 ng.cm$^{-2}$ for 20 and 50 $\mu$g.cm$^{-2}$ loadings were recorded, respectively. If it is assumed that these deviations from $Pt_{poly}$ are due to surface roughness, then based on the work by Kim [27], it can also be assumed that these samples have a surface roughness of $1.61 < R < 5.44$, which implies discrete Pt NPs or islands.

However, this is not entirely true, and doesn't take into account the effects of the underlying carbon surface or the differences in the frequency response curves. Furthermore, one would expect a similar response to $Pt_{poly}$ for the higher loading samples. Again, this does not hold true at the later cycles, due to the severe degree of Pt dissolution.

The phenomena occurring can be broken down into each region, a well-defined $H_{upd}$ region ($H_{upd}$-R) for a loading of 20 $\mu$g.cm$^{-2}$ (fig. 4.12a) is observed, albeit with a wider hysteresis than expected. This, consistently wider hysteresis, could be attributed to the increased hydrophobicity of the sample due to the graphitic carbon, which would alter the surface charge and, hence, the frequency response. This would also explain the slightly wider double layer region's (DLR) frequency response. As for the oxide formation region, there are drastic changes. Initially, a well-defined oxide formation and reduction region (OFRR) is seen, but after 1,000 cycles there is a suppression of this region, with a pinch in the frequency response between 1.0 and 1.1 V vs RHE. Again, it is postulated that this phenomenon is due to interfering surface charge between Pt NPs and carbon hydrophobicity.

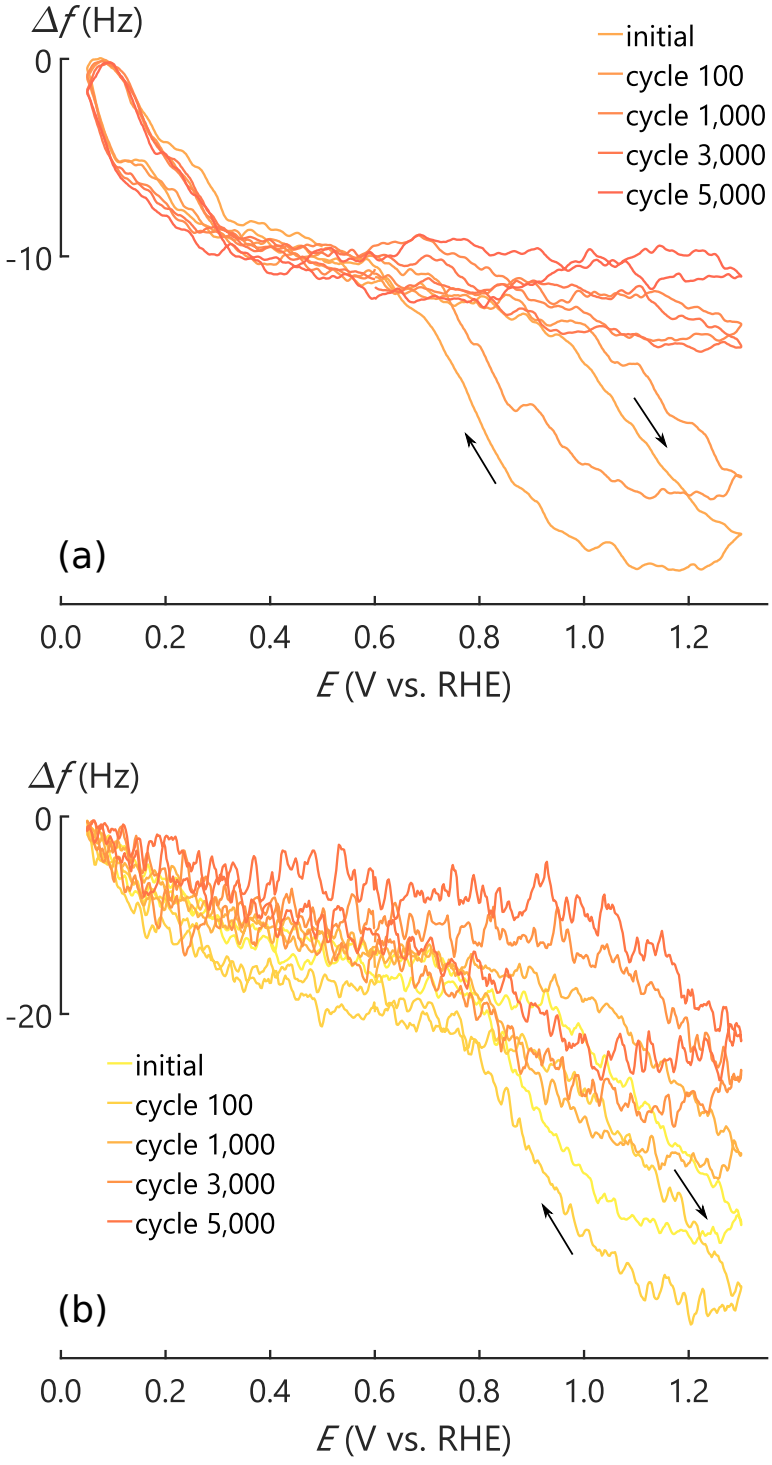


**Figure 4.12 Frequency responses of (a) 20 $\mu$g.cm$^{-2}$ Pt/MFG-P and (b) 50 $\mu$g.cm$^{-2}$ Pt/MFG-P in room temperature Ar saturated 0.5 M $H_2SO_4$ at 50 mV.s$^{-1}$**

With the 50 $\mu$g.cm$^{-2}$ loading (fig. 4.12b), the frequency response is more erratic. The $H_{upd}$-R is very poorly defined and appears to be an extension of the DLR. Whether this is due to a malfunction in the instrument or is a result of the sample is presently unknown. Both the DLR and OFRR both start to broaden and lose their characteristic shapes after 1,000 cycles. Both Pt/MFG-P samples show similar initial roughness factors ($R_{20}$ = 1.83 and $R_{50}$ = 2.03), hence roughness effects have to be excluded. However, the integrity of the deposited Pt film has not been discussed, and with load cycling, we could see a partial delamination of the Pt film leading to entrapment of electrolyte, thus skewing the results [27]. While this is very much speculative, it would require further investigation.

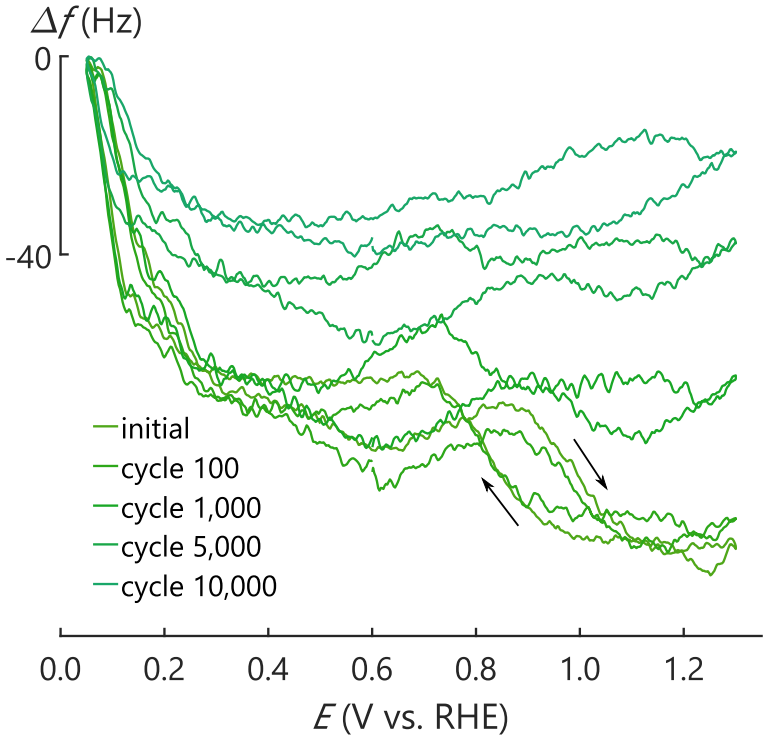


**Figure 4.13 Frequency responses of 20 $\mu$g.cm$^{-2}$ Pt/MFG-H in room temperature Ar saturated 0.5 M $H_2SO_4$ at 50 mV.s$^{-1}$**

In fig. 4.13 the frequency response of 20 $\mu$g.cm$^{-2}$ Pt/MFG-H over 10,000 degradation cycles is presented. Initially, a frequency response, that translates into approximately 563 ng.cm$^{-2}$ over the entire potential range is seen. As with 20 g.cm$^{-2}$ Pt/MFG-P there is a wider than normal $H_{upd}$-R hysteresis, that spans approximately 377 ng.cm$^{-2}$ (69 Hz). It is expected that peroxide modification should alter the hydrophobicity of the carbon, and hence make it more wettable. However, the Pt/HOPG-H shown in chapter 2, presented some exfoliation of the upper most graphene layers. Keeping this in mind, it can be postulated that this large $H_{upd}$-R is due to two processes, (i) interactions with oxygen terminal groups which alters the surface charge by making it slightly more negative, and (ii) electrolyte entrapment between the graphene layers. The second point can be seen in the large DLR, where a separation of charge creating positive regions in the anodic sweep and negative regions during the cathodic sweep are clearly seen, hence accounting for the bulge at $0.40 < E < 0.85$ V vs RHE [22].

The most peculiar phenomenon is the shape of the OFRR. For the first 100 cycles, there is oxide formation during the anodic sweep, but the frequency response suggests that reduction occurs (increase in frequency) after 1.2 V vs RHE. While the general electrochemical processes remain unchanged, the frequency response gives an indication of the interfacial charge, suggesting that there are multiple points of zero total charge (PZTC) throughout these samples. This ties into the results seen in fig. 4.12 (a), indicating changes in surface charge.

Lastly, for Pt/MFG-A, a more stable frequency response over the entire degradation process is seen. A mass variation of 591 ng.cm$^{-2}$ is initially noted for 20 $\mu$g.cm$^{-2}$ Pt/MFG-A (fig. 4.14a), with a mass variation of 563 ng.cm$^{-2}$ noted after 5,000 cycles. In terms of overall mass variation, the Pt/MFG-A performs far better than all the previous MFG samples. This small deviation in overall frequency would suggest that Pt/MFG-A has similarly consistent overall frequency response as for $Pt_{poly}$ (fig. 4.11), thus suggesting that the Pt film/NPs remain in a relative state of harmony, with not much migration across the surface to expose different facets for oxidation.

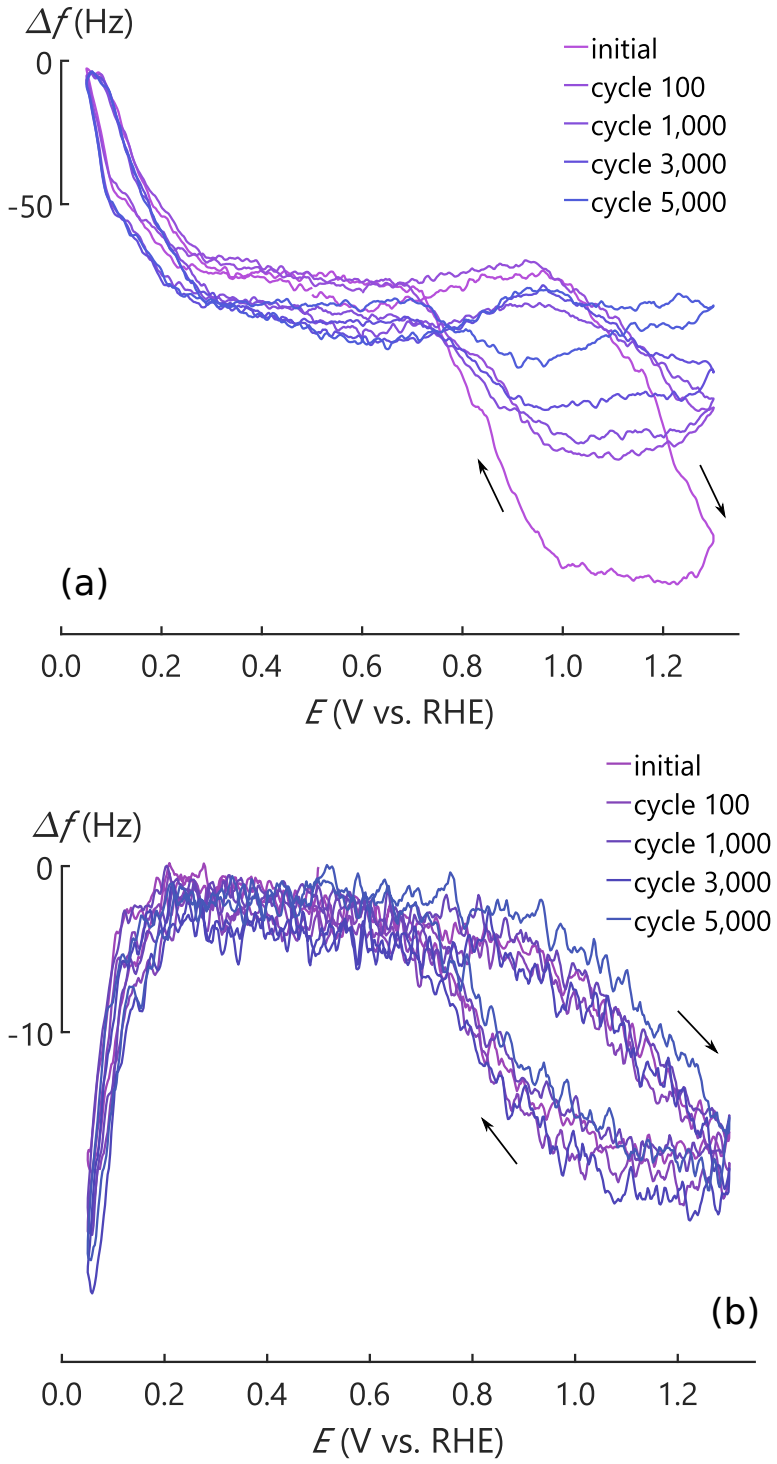


**Figure 4.14 Frequency responses of (a) 20 $\mu$g.cm$^{-2}$ Pt/MFG-A and (b) 50 $\mu$g.cm$^{-2}$ Pt/MFG-A in room temperature Ar saturated 0.5 M $H_2SO_4$ at 50 mV.s$^{-1}$**

In terms of the $H_{upd}$-R and DLR, a similar trend and explanation is observed as for Pt/MFG-H (fig. 4.13). This further strengthens the notion of the surface oxygen groups polarising the surface of the electrode, leading to higher frequency responses. Again, the concept of electrolyte entrapment due to graphene exfoliation is present, albeit to a lesser extent as seen in the case of Pt/MFG-H.

The last frequency response presented here is an interesting situation. For 50 $\mu$g.cm$^{-2}$ Pt/MFG-A (fig. 4.14b) we record a mass variation of 93 ng.cm$^{-2}$ over the entire potential range. This is in close comparison to $Pt_{poly}$, which suggests more bulk Pt behaviour. Furthermore, the consistency in the frequency response over 5,000 cycles supports the notion that Pt is less mobile across the surface.

The most intriguing phenomenon is the flip observed in the $H_{upd}$-R. This stark difference is unusual and reasoning for it can only be speculated at this time. However, if the differences between this sample and the rest of the MFG samples are considered, a possible explanation for this phenomenon may be inferred. Firstly, based on the consistency of overlap of the frequency response, this sample behaves most like $Pt_{poly}$, which would suggest that the surface oxide groups are maintaining stable Pt film across the surface. Secondly, because changes in the OFRR are not seen, it can be assumed that Pt is not mobile at all with minimal dissolution (table 4.2). Secondly, because there is no expansion of the DLR, it can be assumed that there is no drastic change in surface charge, leaving a uniformly charged DLR. With this insight, it can only be assumed that the PZTC is at a low enough potential (due to electronic changes from the oxygen groups) that we have a positively charged Pt surface during $H_{upd}$.

It is interesting to note that this phenomenon is not replicated in the 20 $\mu$g.cm$^{-2}$ loading (fig. 4.14a). There is one possibility for this, the loading is too low and does not cover the entire surface homogenously, allowing for electrolyte to penetrate to the surface of the carbon. This would lead to complex relationship between the electrolyte and the electrode, where ultimately the negative carbon surface dominates all other forces.

## 4.4 Conclusions

In this work, it has been successfully shown for the first time, that there is a large influence of surface functional groups on the frequency response while using the EQCN technique.

The EQCN technique clearly indicates that there is a change of surface charge during Pt dissolution, which is most evident in the OFRR. While most of this is qualitatively determined in combination with the works published by Jerkiewicz *et al.* [1-3] and Kim [27], it is a strong first step in truly understanding the Pt dissolution phenomenon on a real-world like electrocatalyst.

It is interesting to note the influence of surface oxygen terminated groups on carbon, and how the interaction of electron withdrawing vs electron donating groups influence the interfacial area and the Pt mobility across the surface. A trend of Pt stability on Pt/MFG-A > Pt/MFG-P > Pt/MFG-H is seen, which is believed to be more accurate than using conventional electrochemical techniques. This is also a first step in correlating experiment with theory for Pt/C electrocatalysts and how Pt NPs are stabilised on the surface.

Although this work draws these strong conclusions, it confirms initial calculations of the modelling works by Matsutsu *et al.* [44] and Eikerling *et al.* [43] on understanding the mobility of Pt across the surface and influence of interfacial surface charges.

## 4.5 References

[1] Jerkiewicz, G., *Electrochemical hydrogen adsorption and absorption part 1: Under-potential deposition of hydrogen*. Electrocatalysis, 2010. **1**(4): p. 179-199.

[2] Jerkiewicz, G., Vatankhah, G., Lessard, J., Soriaga, M. P., and Park, Y.-S., *Surface-oxide growth at platinum electrodes in aqueous $H_2SO_4$: Reexamination of its mechanism through combined*

*cyclic-voltammetry, electrochemical quartz-crystal nanobalance, and Auger electron spectroscopy measurements*. Electrochimica Acta, 2004. **49**(9–10): p. 1451-1459.

[3] Jerkiewicz, G., Vatankhah, G., Tanaka, S.-i., and Lessard, J., *Discovery of the potential of minimum mass for platinum electrodes*. Langmuir, 2011. **27**(7): p. 4220-4226.

[4] Jerkiewicz, G., Vatankhah, G., Zolfaghari, A., and Lessard, J., *Analysis of the mass response of the electrochemical quartz-crystal nanobalance in horizontal and vertical geometry*. Electrochemistry Communications, 1999. **1**(9): p. 419-424.

[5] Kim, J. and Jerkiewicz, G., *Influence of the surface roughness of platinum electrodes on the calibration of the electrochemical quartz-crystal nanobalance*. Analytical Chemistry, 2017. **89**(14): p. 7462-7469.

[6] Kim, J., Munro, A., Beauchemin, D., and Jerkiewicz, G., *Limits of detection and quantification of electrochemical quartz-crystal nanobalance in platinum electrochemistry and electrocatalysis research*. Analytical Chemistry, 2016. **88**(21): p. 10599-10604.

[7] Kim, J., Urchaga, P., Baranton, S., Coutanceau, C., and Jerkiewicz, G., *Interfacial structure of atomically flat polycrystalline Pt electrodes and modified Sauerbrey equation*. Physical Chemistry Chemical Physics, 2017. **19**(33): p. 21955-21963.

[8] Vatankhah, G., Lessard, J., Jerkiewicz, G., Zolfaghari, A., and Conway, B. E., *Dependence of the reliability of electrochemical quartz-crystal nanobalance mass responses on the calibration constant, $C_f$: analysis of three procedures for its determination*. Electrochimica acta, 2003. 48(11): p. 1613-1622.

[9] Gu, N., Niu, L., and Dong, S., *Simultaneous determination of both the calibration constant in an electrochemical quartz crystal microbalance and the active surface area of a polycrystalline gold electrode*. Electrochemistry Communications, 2000. **2**(1): p. 48-50.

[10] Jeffrey, C. A., Storr, W. M., and Harrington, D. A., *Electrochemical quartz-crystal microbalance study of silver and copper electrodeposition on bare and iodine-covered platinum electrodes*. Journal of Electroanalytical Chemistry, 2004. **569**(1): p. 61-70.

[11] Ratieuville, Y., Viers, P., Alexandre, J., and Durand, G., *A new electrochemical cell adapted to quartz crystal microbalance measurements*. Electrochemistry Communications, 2000. **2**(12): p. 839-844.

[12] Chatenet, M., *Electrochemical quartz crystal microbalance determination of nickel formal partial charge number as a function of the electrode potential upon nickel underpotential deposition on platinum in sulfuric medium*. Electrocatalysis, 2015. **6**(4): p. 382-389.

[13] Bizet, K., Gabrielli, C., and Perrot, H., *Immunodetection by quartz crystal microbalance*. Applied Biochemistry and Biotechnology, 2000. **89**(2): p. 139.

[14] Buttry, D. A. and Ward, M. D., *Measurement of interfacial processes at electrode surfaces with the electrochemical quartz crystal microbalance*. Chemical Reviews, 1992. **92**: p. 1355-1379.

[15] Hepel, M., *Electrode-solution interface studied with electrochemical quartz crystal nanobalance*, in *Interfacial electrochemistry: Theory, experiment, and applications*, A. Wieckowski, Editor. 1999, Marcel Dekker, Inc.: New York.

[16] Hepel, M., Kanige, K., and Bruckenstein, S., I*n situ underpotential deposition study of lead on silver using the electrochemical quartz crystal microbalance*. Journal of Electroanalytical Chemistry and Interfacial Electrochemistry, 1989. **266**(2): p. 409-421.

[17] Keita, B., Nadjo, L., Belanger, D., Wilde, C. P., and Hilaire, M., *Electrochemical quartz crystal microbalance: Evidence for the adsorption of heteropoly and isopoly anions on gold electrodes*. Journal of Electroanalytical Chemistry, 1995. **384**(1): p. 155-169.

[18] Koh, W., Kutner, W., Jones, M. T., and Kadish, K. M., *An improved holder for the electrochemical quartz crystal microbalance and its cyclic voltammetry characteristics*. Electroanalysis, 1993. **5**(3): p. 209-214.

[19] Wilde, C. P. and Zhang, M., A*dsorption and underpotential deposition of lead at electrodeposited platinum electrodes*. Journal of Electroanalytical Chemistry, 1992. **327**(1): p. 307-320.

[20] O'Sullivan, C. K. and Guilbault, G. G., *Commercial quartz crystal microbalances – theory and applications*. Biosensors and Bioelectronics, 1999. **14**(8): p. 663-670.

[21] Ofstad, A. B., Thomassen, M. S., Gomez de la Fuente, J. L., Seland, F., Møller-Holst, S., and Sunde, S., *Assessment of platinum dissolution from a Pt/C fuel cell catalyst: An electrochemical quartz crystal microbalance study*. Journal of The Electrochemical Society, 2010. **157**(5): p. B621-B627.

[22] Wickman, B., Grönbeck, H., Hanarp, P., and Kasemo, B., *Corrosion induced degradation of Pt/C model electrodes measured with electrochemical quartz crystal microbalance*. Journal of The Electrochemical Society, 2010. **157**(4): p. B592-B598.

[23] Fortuin, A. C., Jackson, C., Carleschi, E., Doyle, B. P., Shnier, A., Kriek, R. J., Ray, S. C., Billing, D. G., Wamwangi, D., Scherer, G. G., and Levecque, P. B. J., *Towards practical applications of EQCN experiments to study Pt anchor sites on carbon surfaces*. Electrocatalysis, 2018. **9**(2): p. 271-278.

[24] Kim, U. J., Furtado, C. A., Liu, X., Chen, G., and Eklund, P. C., *Raman and IR spectroscopy of chemically processed single-Walled carbon nanotubes*. Journal of the American Chemical Society, 2005. **127**(44): p. 15437-15445.

[25] Schönfelder, R., Avilés, F., Knupfer, M., Azamar-Barrios, J. A., González-Chi, P. I., and Rümmeli, M. H., *Influence of architecture on the Raman spectra of acid-treated carbon nanostructures*. Journal of Experimental Nanoscience, 2014. **9**(9): p. 931-941.

[26] Falch, A., Lates, V., and Kriek, R. J., *Combinatorial plasma sputtering of $Pt_xPd_y$ thin film electrocatalysts for aqueous $SO_2$ electro-oxidation*. Electrocatalysis, 2015. **6**(3): p. 322-330.

[27] Kim, J., *Comprehensive study of the influence of surface roughness of platinum electrodes on their interfacial mass changes as examined using the electrochemical quartz-crystal nanobalance*, in *Dept. of Chemistry*. 2017, Queen's University.

[28] Ohma, A., Shinohara, K., Iiyama, A., Yoshida, T., and Daimaru, A., *Membrane and catalyst performance targets for automotive fuel cells by FCCJ membrane, catalyst, MEA WG*. ECS Trans., 2011. **41**(1): p. 775-784.

[29] *Multi-year research, development and demonstration Plan*. 2012, U.S. Department of Energy: Office of Energy Efficiency and Renewable Energy.

[30] Lichter, J. A. *Crystals and Oscillators*, JL9113 Rev. C. [cited 2018, 11 Jan]; Available from: http://www.nelfc.com/pdf/pdfapp/9113.pdf.

[31] Kinoshita, K., *Carbon: Electrochemical and physicochemical properties*. A Wiley-Interscience publication. 1988: Wiley.

[32] Cline, K. K., McDermott, M. T., and McCreery, R. L., *Anomalously slow electron transfer at ordered graphite electrodes: Influence of electronic factors and reactive sites*. Journal of Physical Chemistry, 1994. **98**(20): p. 5314-5319.

[33] McCreery, R. L., *Carbon electrodes: Structural effects on electron transfer kinetics*. Electroanalytical chemistry, 1991. **17**: p. 221-374.

[34] Batina, N., Will, T., and Kolb, D. M., *Study of the initial stages of copper deposition by in situ scanning tunnelling microscopy*. Faraday Discussions, 1992. **94**: p. 93-106.

[35] Green, C. L. and Kucernak, A., *Determination of the platinum and ruthenium surface areas in platinum−ruthenium alloy electrocatalysts by underpotential deposition of copper. I. Unsupported catalysts*. The Journal of Physical Chemistry B, 2002. **106**(5): p. 1036-1047.

[36] Marković, N. M., Gasteiger, H. A., Lucas, C. A., Tidswell, I. M., and Ross, P. N., *The effect of chloride on the underpotential deposition of copper on Pt(111): AES, LEED, RRDE, and X-ray scattering studies*. Surface Science, 1995. **335**: p. 91-100.

[37] Markovic, N. M., Gasteiger, H. A., and Ross, P. N., Jr., *Copper electrodeposition on Pt(111) in the presence of chloride and (bi)sulfate: Rotating ring-Pt(111) disk electrode studies*. Langmuir, 1995. **11**(10): p. 4098-4108.

[38] Danilov, A. I., Molodkina, E. B., Polukarov, Y. M., Climent, V., and Feliu, J. M., *Active centers for Cu UPD–OPD in acid sulfate solution on Pt (111) electrodes*. Electrochimica acta, 2001. **46**(20): p. 3137-3145.

[39] Gomez, R., Yee, H. S., Bommarito, G. M., Feliu, J. M., and Abrun, H. D., *Anion effects and the mechanism of Cu UPD on Pt (111): X-ray and electrochemical studies*. Surface science, 1995. **335**: p. 101-109.

[40] Jaya, S., Rao, T. P., and Rao, G. P., *Underpotential deposition studies of copper on glassy carbon*. Journal of Chemical Sciences, 1986. **97**(5): p. 581-586.

[41] McCreery, R. L., Cline, K. K., McDermott, C. A., and McDermott, M. T., *Control of reactivity at carbon electrode surfaces*. Colloids and Surfaces A, 1994. **93**(0): p. 211-219.

[42] Xing, L., Hossain, M. A., Tian, M., Beauchemin, D., Adjemian, K. T., and Jerkiewicz, G., *Platinum electro-dissolution in acidic media upon potential cycling*. Electrocatalysis, 2014. **5**(1): p. 96-112.

[43] Huang, J., Malek, A., Zhang, J., and Eikerling, M. H., *Non-monotonic surface charging behavior of platinum: a paradigm change*. The Journal of Physical Chemistry C, 2016. **120**(25): p. 13587-13595.

[44] Matsutsu, M., Petersen, M. A., and van Steen, E., *$Pt_{38}$ cluster on OH- and COOH-functionalised graphene as a model for Pt/C-catalysts*. Phys Chem Chem Phys, 2016. **18**(36): p. 25693-25704.

# Chapter 5
# Conclusions and Outlook

## 5.1 Conclusions

In this study work has been conducted and presented to better understand Pt interactions with its carbon support.

We considered the use of a model electrochemical system, in which we employed a highly orientated pyrolytic graphite (HOPG) as a two-dimensional carbon system. The surface of HOPG was modified by aggressive chemical oxidation with Fenton's reagent and acid oxidation. This resulted in the exfoliation of the top few graphene layers from the HOPG substrate. Although, the exfoliation was not homogeneous across the entire surface, it is suspected that mono-vacancies were formed.

The results indicate that the oxidation of the basal plane of HOPG was successful. Deposition of Pt to the correct loadings was also achieved and confirmed by X-ray reflectometry. Further sample analysis, *viz*. X-ray photoelectron spectroscopy and X-ray diffractometry, seem to suggest that Pt forms clusters around oxygen terminated groups, creating islands of Pt. The fact that islands formed, suggests that oxygen terminated groups are not spread homogenously across the surface of the HOPG substrate, but rather form at edge sites and mono-vacancies.

Based on the electrochemical results, there is not much difference in current response between the different HOPG samples after potential cycling for Pt dissolution. It is believed that Pt implantation plays a large role in this, hence skewing the results. However, from the differential capacitance results we clearly see a change in surface charge based on the shift of the potential of zero total charge (PZTC) above and below that of pristine HOPG.

In order to gain more in depth understanding of Pt mobility across the surface of HOPG, and how it interacts with the oxygen terminated groups, the use of the electrochemical quartz crystal nano-balance (EQCN) technique was employed.

The use of as received mirror finished graphite (MFG) quartz crystals was chosen, for simplicity. Because of this, HOPG carbon and MFG carbon had to be compared in order to ascertain whether or not the EQCN results can be directly compared to the HOPG results recorded by a conventional electrochemical system.

While the bare carbons could not be compared directly, samples with Pt deposited are qualitatively comparable. Further to this, the MFG substrate was oxidised in a similar manner as HOPG. These modifications and deposition of Pt did not adversely affect the integrity of the quartz crystal, nor did it alter the base frequency of the crystals significantly.

With the calibration of the system, it was shown that our system is optimised and accurately reproduces results described in literature. We could now confidently study Pt interaction on carbon with the EQCN technique.

On first inspection, the current response results of the MFG samples mimicked that of the HOPG samples. This further confirmed that the systems are comparable, and that potential cycling had the same effect qualitatively.

The frequency response offered the most interesting results, with a clear indication of changes in the surface charge of Pt with increased potential cycling. This work does give an indication that the surface of Pt is not monotonic and is a first step in confirming the theoretical work by Eikerling *et al.* [1]. This suggests that there are metal support interactions, and extent of these interactions are dependent on the oxygen terminated group. It is believed that a frequency response that mimics bulk $Pt_{poly}$, is an indication of stronger metal support interactions, with limited Pt mobility. As a result, the results indicate a Pt stability as follows:

-COOH functionalised graphite > pristine graphite > -OH functionalised graphite. These results are counterintuitive, but it is suspected that there is a large degree of exfoliation for the -OH functionalised groups, hence the observed trend. However, the effects of electron donating, might be another cause for concern, hence aiding in Pt mobility.

Thus, we have been able to illustrate that there are sites which anchor Pt to carbon and these do aid in reducing Pt mobility and, hence, Pt dissolution. More importantly, it is clear that the EQCN technique can be used to study these phenomena. While the EQCN technique gives us valuable electrochemical information, it is an instrument that gives us an indication of the secrets of metal support interactions at the a more fundamental level.

With careful experimental setup, design and optimisation, the EQCN technique can and should be employed in studying electrocatalyst phenomenon to better understand the more fundamental aspects of the electrocatalyst. It is truly a link between experiment and theory.

In conclusion, this study has been able to meet its outlined objectives.

## 5.2 Outlook

This work has been successful in meeting the outlined objectives, however there are still some gaps in the understanding on this particular topic of metal support interactions in electrocatalysts.

It is advised that more intensive characterisation is measured to prove or disprove the postulations determined from the results presented here. Firstly, it would be critical to quantify the oxygen terminated surface groups by Fourier transform infrared spectroscopy (FT-IR) and determined the d-band to g-band ratios of these samples by Raman spectroscopy. A better

understanding of the starting material will lead to a better understanding of the electrochemical response.

In order to best quantify the phenomenon presented in this work, studying the system by *in-situ* FT-IR will give an indication of whether Pt does in fact cluster around the oxygen terminated groups over time. This will result in a reduced signal for oxygen groups between 3,200 and 1,000 $cm^{-1}$. Secondly, the use of *in-situ* Raman spectroscopy will give a clear indication of $PtO_x$ formation and together with CO displacement will illustrate how the surface charge changes with time.

The above experiments will lead to invaluable insight into the system, with a strong experimental backbone on which to develop an accurate model for Pt dissolution mechanisms and the influence oxygen terminated groups as anchoring points for Pt.

Lastly, while it might not be able to quantify, *in-situ* electrochemical atomic force microscopy, will be able to qualitatively give us an indication of Pt mobility across the surface of carbon. This will reveal if in fact Pt NPs form and if they are mobile across the surface by changes in surface charge or by constant dissolution and deposition. The use of the Kelvin probe technique would be most beneficial.

## 5.3 References

[1] Huang, J., Malek, A., Zhang, J., and Eikerling, M. H., *Non-monotonic surface charging behavior of platinum: a paradigm change*. The Journal of Physical Chemistry C, 2016. **120**(25): p. 13587-13595.

Appendix A – Chapter 3

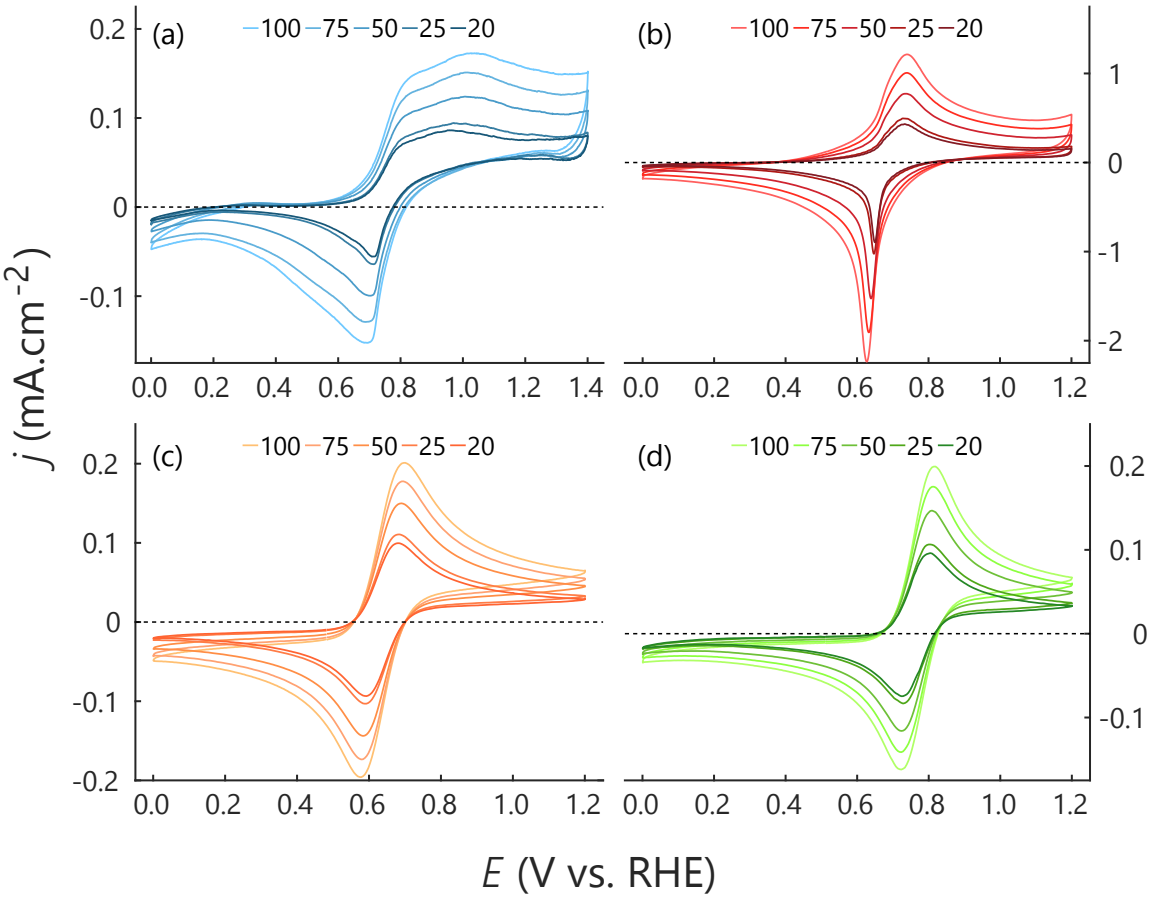


**Figure A.1 Current responses of (a) HOPG-P, (b) HOPG-H, (c) MFG-P, and (d) MFG-H in 1 mM $[Fe(CN)_6]^{4-}$ / 1 M $KCl_{(aq)}$ solution under Ar saturation and room temperature, with a sweep rate of 20, 25, 50, 75, and 100 $mV.s^{-1}$**

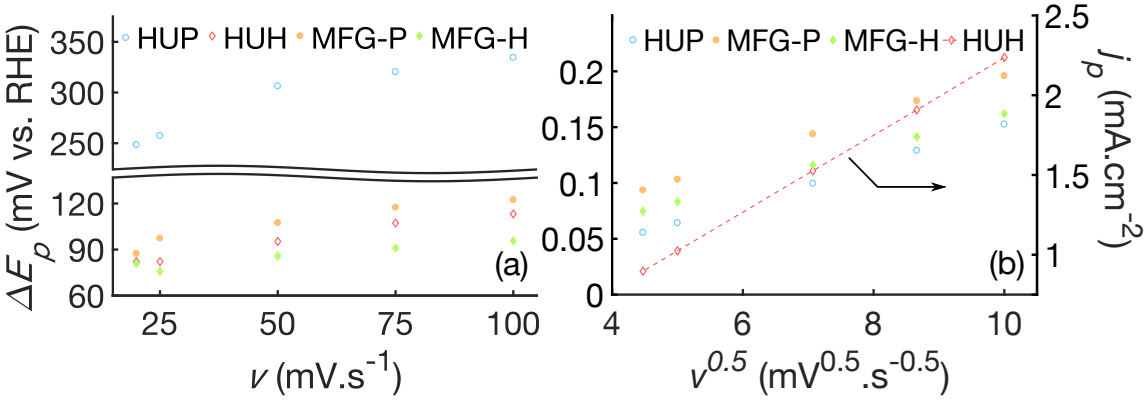


**Figure A.2 Summary of (a) $\Delta E_p$ and (b) $j_p$ for HOPG-P, HOPG-H, MFG-P, and MFG-H as a function of scan rate ($\nu$) and square root of scan rate ($\nu^{0.5}$) respectively**

Appendix B – Chapter 4

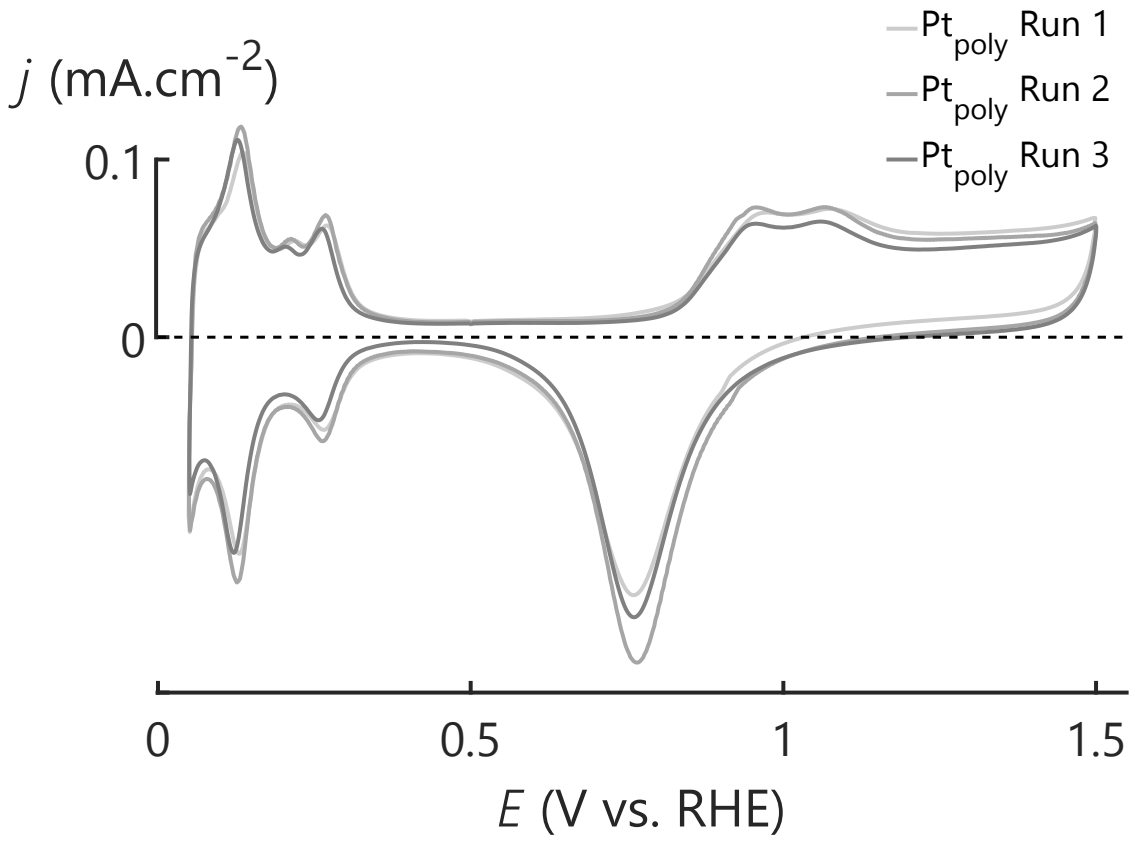


**Figure B.1: Three separate $Pt_{poly}$ cyclic voltammograms runs in room temperature Ar saturated 0.5 M $H_2SO_4$ at 50 $mV.s^{-1}$ to illustrate reproducibility of the EQCN system**

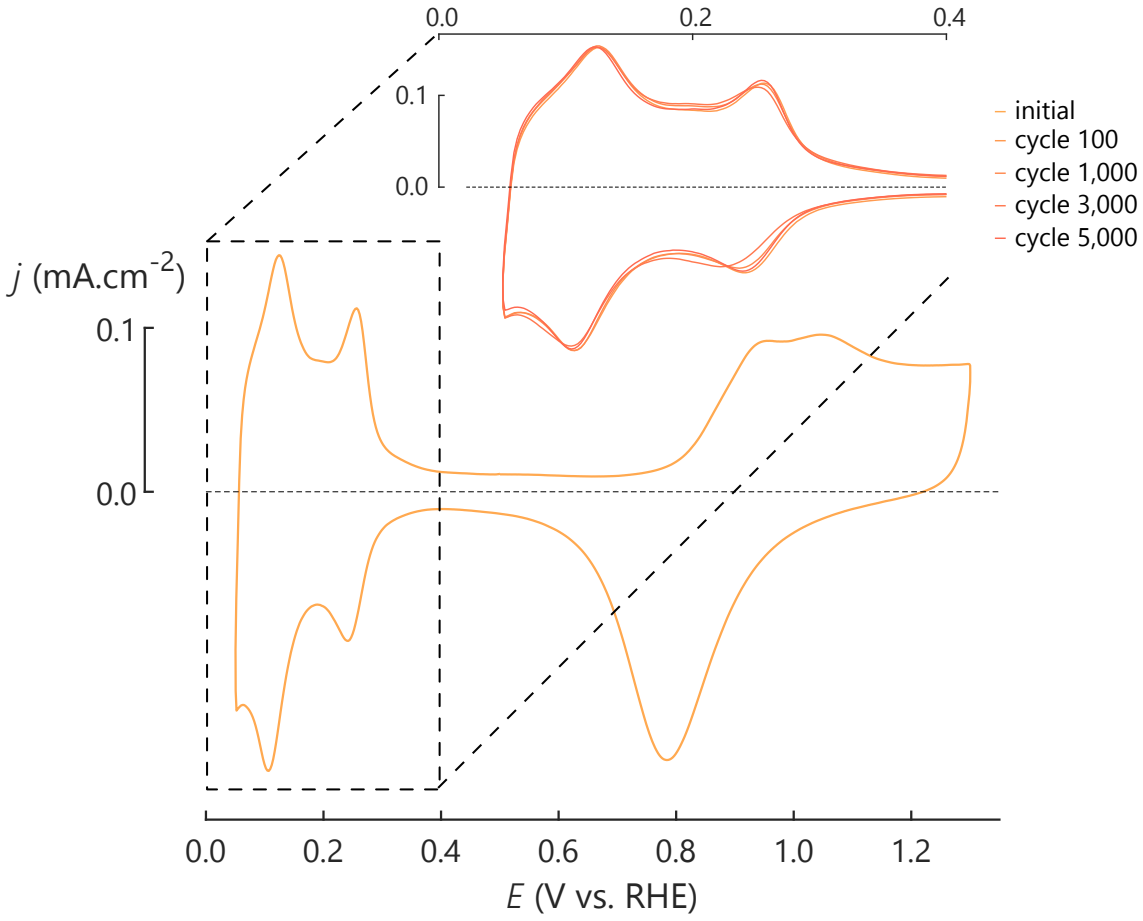


**Figure B.2 Current response of 20 $\mu$g.cm$^{-2}$ Pt/MFG-P in room temperature Ar saturated 0.5 M $H_2SO_4$ at 50 mV.s$^{-1}$, inset is the hydrogen region used to determine the ECSA over 5,000 cycles**

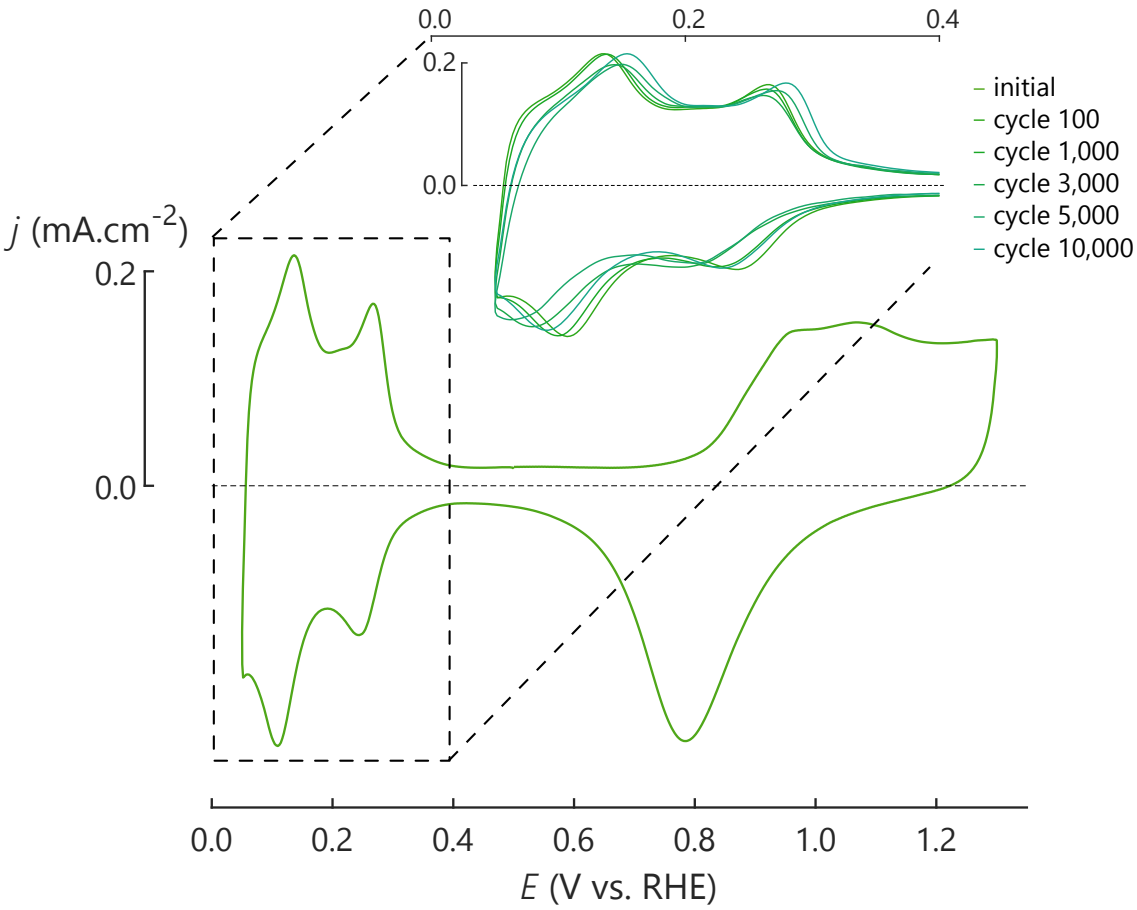


**Figure B.3 Current response of 20 $\mu$g.cm$^{-2}$ Pt/MFG-H in room temperature Ar saturated 0.5 M $H_2SO_4$ at 50 mV.s$^{-1}$, inset is the hydrogen region used to determine the ECSA over 10,000 cycles**

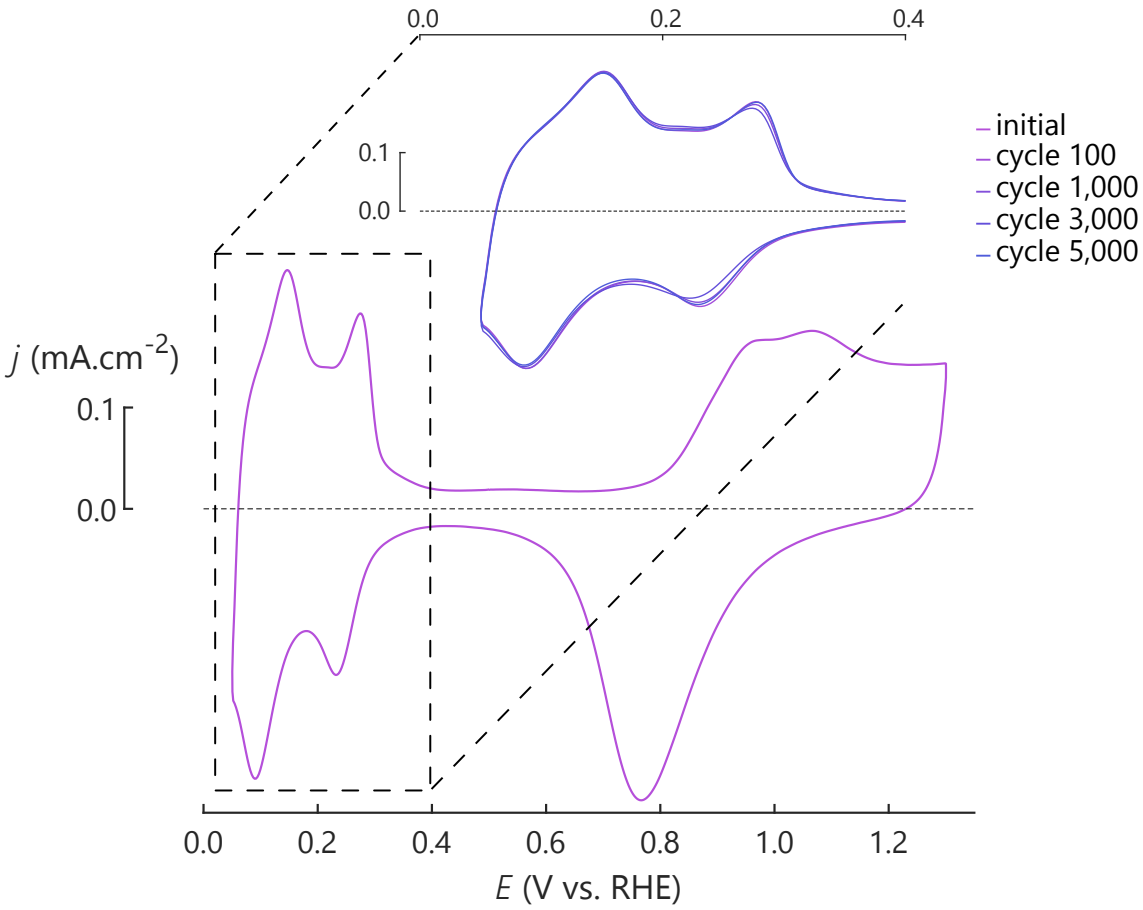


**Figure B.4 Current response of 20 $\mu$g.cm$^{-2}$ Pt/MFG-A in room temperature Ar saturated 0.5 M $H_2SO_4$ at 50 mV.s$^{-1}$, inset is the hydrogen region used to determine the ECSA over 5,000 cycles**

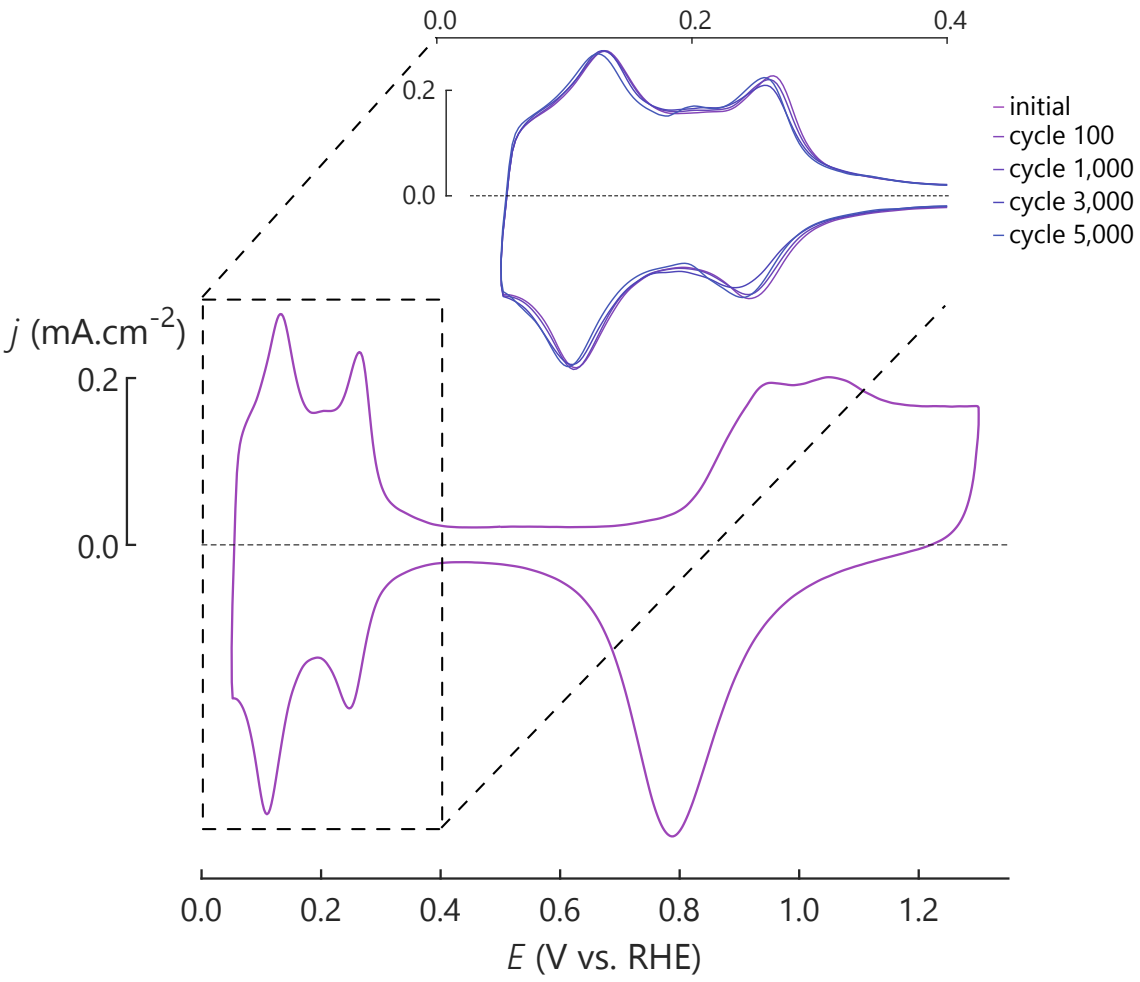


**Figure B.5 Current response of 50 $\mu$g.cm$^{-2}$ Pt/MFG-A in room temperature Ar saturated 0.5 M $H_2SO_4$ at 50 mV.s$^{-1}$, inset is the hydrogen region used to determine the ECSA over 5,000 cycles**

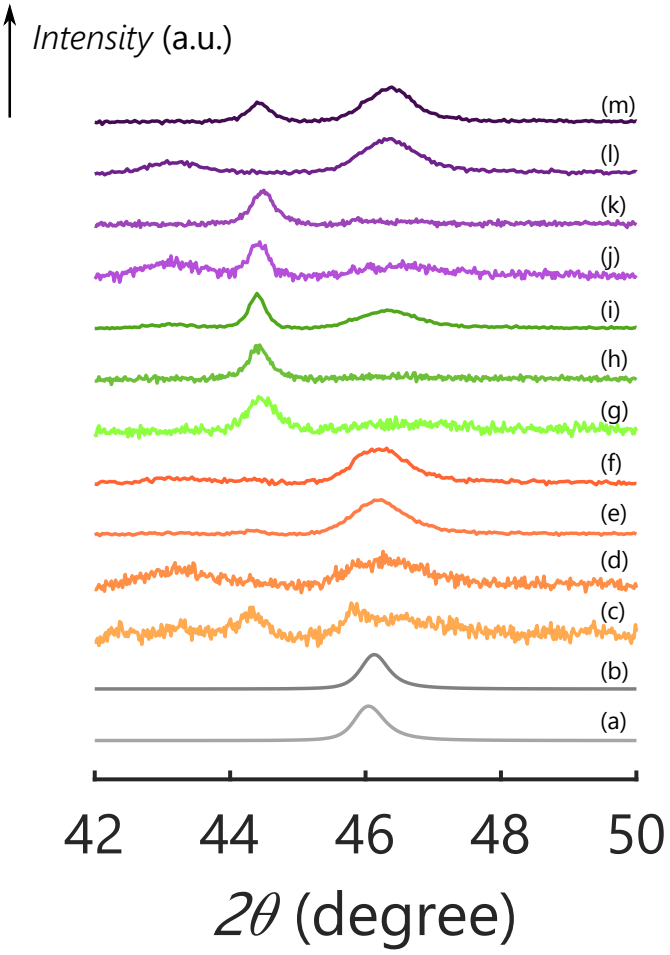


**Figure B.6 Normalised diffractograms of (a) $Pt_{poly}$ initial, (b) $Pt_{poly}$ after degradation (c) 20 $\mu g.cm^{-2}$ Pt/MFG-P initial, (d) 20 $\mu g.cm^{-2}$ Pt/MFG-P after degradation (e) 50 $\mu g.cm^{-2}$ Pt/MFG-P initial, (f) 50 $\mu g.cm^{-2}$ Pt/MFG-P after degradation (g) 20 $\mu g.cm^{-2}$ Pt/MFG-H initial, (h) 20 $\mu g.cm^{-2}$ Pt/MFG-H after degradation, (i) 50 $\mu g.cm^{-2}$ Pt/MFG-H, (j) 20 $\mu g.cm^{-2}$ Pt/MFG-A initial, (k) 20 $\mu g.cm^{-2}$ Pt/MFG-A after degradation, (l) 50 $\mu g.cm^{-2}$ Pt/MFG-A initial, and (m) 50 $\mu g.cm^{-2}$ Pt/MFG-A after degradation**